RESEARCH & DEVELOPMENT

# CFRP Strands in Prestressed Cored Slab Units


**Griffith Shapack, EIT**
**Rudolf Seracino, PhD**
**Gregory Lucier, PhD**
**Sami Rizkalla, PhD**

**Department of Civil, Construction, and Environmental Engineering**
**North Carolina State University**



**FHWA/NC/2014-09**

**February 2016**

**FHWA/NC/2014-09**

# CFRP Strands in Prestressed Cored Slab Units


| | |
|---|---|
| Principal Investigator | Dr. Rudolf Seracino |
| Key Researcher | Dr. Gregory Lucier |
| Key Researcher | Dr. Sami Rizkalla |
| Research Assistant | Mr. Griffith Shapack |

**Department of Civil, Construction, and Environmental Engineering**
**North Carolina State University**
Raleigh, NC


Prepared for:
**North Carolina Department of Transportation**
Research and Development Unit

February 2016

Technical Report Documentation Page

| 1. Report No. | 2. Governmental Accession No. | 3. Recipient's Catalog No. |
|---|---|---|
| FHWA/NC/2014-09 | | |

| 4. Title and Subtitle | 5. Report Date |
|---|---|
| CFRP Strands in Prestressed Cored Slab Units | February 2016 |
| | 6. Performing Organization Code |
| 7. Author(s)<br>Rudolf Seracino, Gregory Lucier, Sami Rizkalla, Griffith Shapack | 8. Performing Organization Report No. |
| 9. Performing Organization Name and Address<br>Department of Civil, Construction, and Environmental Engineering<br>North Carolina State University<br>Raleigh, NC 27695-7908 | 10. Work Unit No. (TRAIS)<br>11. Contract or Grant No. |
| 12. Sponsoring Agency Name and Address<br>North Carolina Department of Transportation<br>Research and Development Unit<br>104 Fayetteville Street<br>Raleigh, NC 27601 | 13. Type of Report and Period Covered<br>August 2013 - May 2015<br>14. Sponsoring Agency Code<br>NCDOT Project No.: 2014-09 |

15. Supplementary Notes

16. Abstract

Steel prestressed cored slab superstructures are a structural system commonly used for bridges in coastal North Carolina. However, due to the aggressive marine environment several of such bridges are in need of major repairs or replacement after being in service for little more than 40 years. In order to prevent the premature deterioration of future bridges, an investigation was conducted into replacing steel prestressed cored slabs with FRP prestressed cored slabs.

A research program was undertaken to design, manufacture, and test to failure full-scale cored slabs prestressed with carbon FRP (CFRP) and reinforced with glass FRP (GFRP) stirrups. Direct tension tests were conducted on the CFRP strands and GFRP bars to validate the manufacturers' design values. Beam-end specimens were tested to comparatively evaluate the bond characteristics of the CFRP strand. Two 45-ft long CFRP prestressed cored slabs were tested in flexure, while two were 15-ft long and tested in shear. The concrete section and CFRP strand layout were designed to be similar to those of current steel prestressed cored slabs so that they may be cast using existing stressing beds at precast facilities familiar with the production of cored slabs. Test results of the experimental program were compared to the predicted performance and strength of the CFRP prestressed cored slabs relative to current design recommendations given in the current ACI 440 design guides. Direct comparison to control steel prestressed cored slabs ensured that the CFRP cored slabs would be a suitable replacement alternative.

| 17. Key Words | 18. Distribution Statement |
|---|---|
| Carbon fiber strands; Prestressed cored slabs; Bridge deck; Carbon FRP; Glass FRP. | |

| 19. Security Classif. (of this report) | 20. Security Classif. (of this page) | 21. No. of Pages | 22. Price |
|---|---|---|---|
| Unclassified | Unclassified | 133 | |

**Form DOT F 1700.7** (8-72) **Reproduction of completed page authorized**

## DISCLAIMER

The opinions, findings, and conclusions found in this report reflect the views of the authors and not necessarily the views of North Carolina State University. The authors are responsible for the accuracy of the data presented within this report. This report was also prepared in cooperation with the North Carolina Department of Transportation, although the views in this report are not necessarily the views of the Department, nor the Federal Highway Administration. This report does not constitute a standard, specification, or regulation.

## ACKNOWLEDGMENTS

The research team would like to thank the North Carolina Department of Transportation Technical Advisory Committee who oversaw this project. The Technical Advisory Committee included the following members:

Brian Hanks (Chair)
Todd Garrison
Tom Koch
Gichuru Muchane
Daniel Muller
Christopher Peoples
Greg Perfetti
J. Neil Mastin
F. Rasay Abadilla, Jr. (Project Manager)

Thanks are also extended to Constructed Facilities Laboratory (CFL) technicians Jerry Atkinson and Johnathan McEntire.

## EXECUTIVE SUMMARY


Steel prestressed cored slab superstructures are a structural system commonly used for bridges in coastal North Carolina (NC). This type of bridge is subjected to an aggressive marine environment, so corrosion of the internal reinforcement is of significant concern. Several of these bridges in NC are in need of repair or replacement after having been in service for little more than 40 years.

To prevent corrosion in future cored slab superstructures, the North Carolina Department of Transportation (NCDOT) chose to evaluate the performance of cored slabs reinforced with non-corroding Fiber Reinforced Polymer (FRP) instead of traditional steel. The objective of the study was to investigate the performance of cored slabs prestressed with carbon FRP (CFRP) strands and reinforced with glass FRP (GFRP) stirrups. The structural performance of these experimental cored slabs was compared to that of steel control specimens to evaluate their suitability with respect to the current standard design. The general objective was accomplished through the following specific tasks:

- Previous research in the field of FRP reinforcement was reviewed, with an emphasis on FRP prestressing.
- FRP material tests were performed to confirm manufacturers' design values.
- The bond properties of the CFRP prestressing strands were comparatively measured using tests on beam-end specimens
- The current standard NCDOT cored slab design was reviewed and an all-FRP substitute reinforcing scheme for cored slabs was designed.
- Three full-scale, 45 ft. long cored slabs were cast and tested to failure in flexure. Two of the specimens were reinforced with FRP and a third served as a steel-reinforced control specimen.

- Three full-scale, 15 ft. long cored slabs were cast and tested to failure in shear. Two of the specimens were reinforced with FRP and the third served as a steel-reinforced control specimen.
- The tests of the steel and FRP reinforced specimens were compared to each other and to their calculated design strengths.

This report presents the findings from the literature review, testing, and analysis of the test data. Specific findings include the following:

- A large body of research exists on the topic of FRP prestressing. Test results have shown that the capacity of FRP prestressed concrete members can equal or exceed that of equivalent steel prestressed members.
- A growing number of FRP prestressed bridge decks and piles are being implemented by Departments of Transportation across the country and abroad.
- The manufacturers' reported values for the mechanical properties of the CFRP strand and GFRP rebar used in this project are accurate.
- The voids in a hollow cored slab can float during casting, which has been observed by others, and dramatically weakens the cored slab section. Care must be taken to prevent this phenomenon during construction when using either steel or FRP reinforcement.
- The experimental flexural capacity of the properly manufactured FRP reinforced cored slab was 9% greater than the capacity of the steel reinforced control cored slab, however, this capacity was 10% lower than the unfactored ACI 440.4R (2004) capacity.
- The presence of closely spaced, large diameter GFRP stirrups in the compression zone of the FRP reinforced cored slabs appears to have triggered premature compression zone failure in one of the specimens.
- Even with the postulated effect from the GFRP stirrups, ACI 440.4R (2004) predicts a safe flexural design strength that is 8% lower than the experimental flexural capacity.

- The GFRP stirrups remained intact after all full-scale tests.
- ACI 440.4R (2004) provided conservative predictions for shear strength.
- Due to the nature of the prestressed cored slab section studied, shear failure is unlikely to be a design concern, as the flexural failure mode dominates the behavior for this section.

Based on these findings, the all-FRP reinforcement scheme for cored slabs should be a suitable structural replacement for the current design using steel reinforcement. However, the GFRP stirrups may have had a deleterious effect on the strength of the cored slabs. This effect should be explored further so that it may be quantified, and perhaps mitigated. An alternative arrangement of corrosion resistant shear reinforcement would likely address this situation.

**TABLE OF CONTENTS**

# LIST OF TABLES

## LIST OF FIGURES

## CHAPTER 1: Introduction

### 1.1 Background

The North Carolina Department of Transportation (NCDOT) has used prestressed concrete cored slabs in bridge superstructures for over 40 years. The typical cross section of the steel prestressed cored slab is illustrated in Figure 1.1. The section consists of two tubular cores in a rectangular concrete section 3 ft. wide with shear keys on both sides. These sections have depths ranging from 18 to 24 in. and are usually economical for spans ranging from 40 to 60 ft. In the bridge superstructure, the cored slabs are post-tensioned transversely at the third points of spans then the shear keys are grouted, as shown in Figure 1.2. An asphalt wearing surface is placed directly on the slabs with no need for a cast-in-place concrete deck.

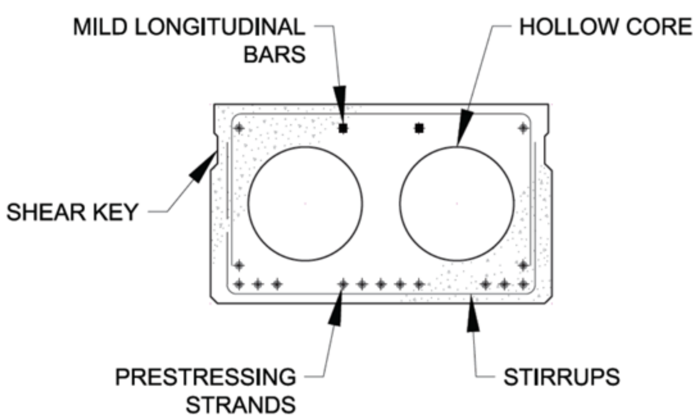


**Figure 1.1: Typical cored slab section**

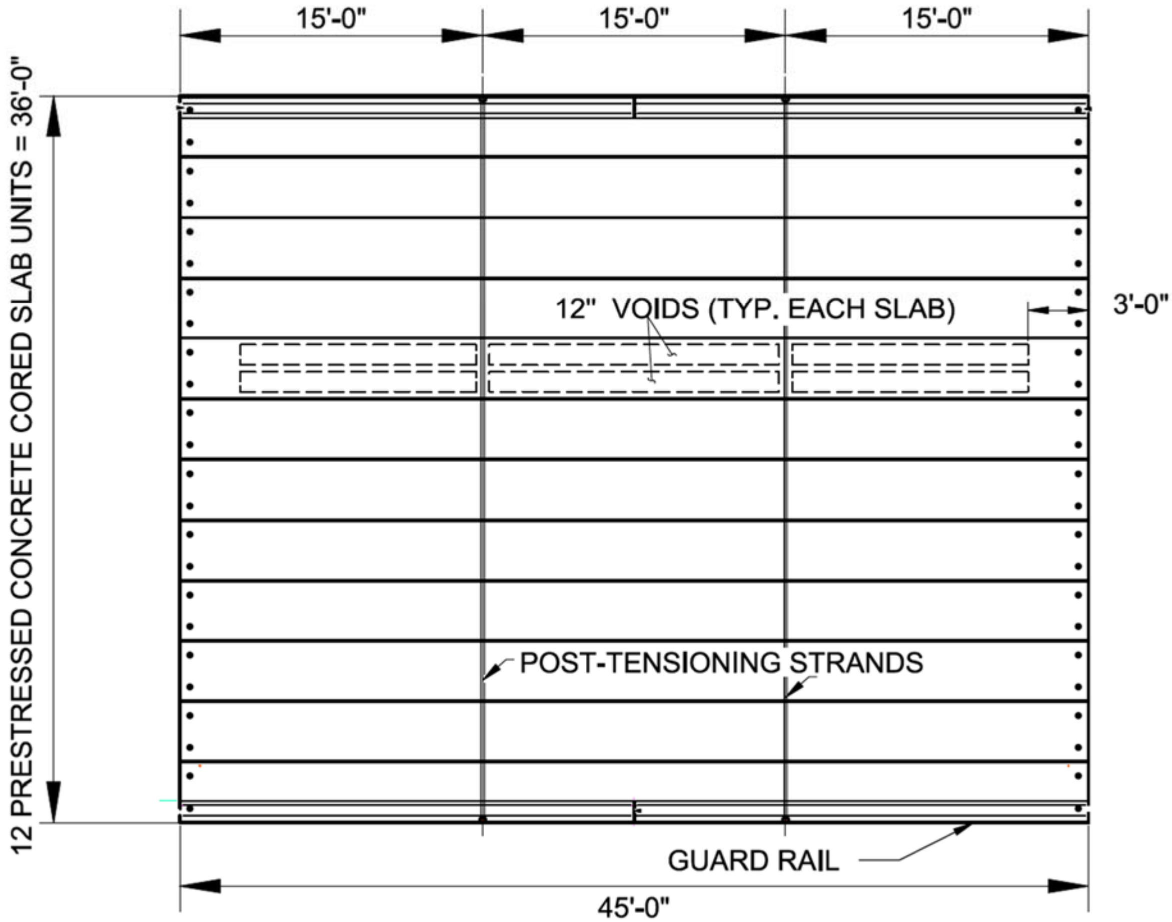


**Figure 1.2: Typical span of cored slab units**

Several cored slab bridges built in the 1970s along the North Carolina coast, similar to that depicted in Figure 1.3, are showing signs of significant deterioration. The soffit of the cored slabs, particularly at the end spans, can be continuously exposed to salt-water splash leading to spalls in the cover concrete caused by corrosion of the bottom stirrup legs and the bottom layer of prestressing. Several cored slab bridge superstructures have been replaced by the NCDOT due to corrosion, and others are scheduled for replacement.

**Figure 1.3: Typical cored slab bridge in coastal North Carolina**

Fiber Reinforced Polymer (FRP) is a non-corroding composite material with high tensile strength. Since the late 1980's, FRP has been used as tensile reinforcement in concrete structures around the world. It has been tested and implemented in exceedingly corrosive environments where it has been proven to be a safe, durable alternative to steel reinforcement (Soudki 1998). FRP manufacturers have developed a wide variety of products, including products that can replace both prestressing strands and mild steel reinforcement.

### 1.2 Objectives

The purpose of this research project was to design, test, and evaluate an all-FRP reinforcing scheme for prestressed concrete cored slabs. It was critical that the structural performance met or exceeded the current performance from equivalent steel reinforced beams. Because the cored slabs are a standard design and precast plants have dedicated equipment for casting them, the existing design parameters were changed as little as possible.

Carbon FRP (CFRP) prestressing strands and Glass FRP (GFRP) rebar were the reinforcement materials chosen. An investigation into their mechanical properties was critical to proper design of the cored slabs. Traditional steel reinforced and experimental FRP reinforced cored slabs were cast and tested to evaluate the performance of the FRP reinforcing scheme relative to the existing design.

### 1.3 Scope

The experimental program started with direct tension tests of six CFRP strand specimens and six GFRP rebar specimens to establish their material properties. Ten beam-end specimens were then fabricated and tested to examine the bond strength of the CFRP strand compared to steel strand. The bonded length of the CFRP and steel strands was varied in each beam-end specimen. Finally, full-scale cored slabs were cast and loaded to failure in flexural and shear. For each set of tests, one steel reinforced cored slab was cast as a control specimen and two identical FRP reinforced cored slabs were cast as experimental specimens. Both ends of each shear specimen were tested.

# CHAPTER 2: Literature Review

## 2.1 Introduction

Prestressed concrete bridge girders face deterioration from harmful environmental factors such as freeze-thaw cycles and exposure to de-icing salts and saltwater. Over time, the steel reinforcement in concrete bridges corrodes, which often leads to the costly repair or replacement of bridges after a relatively short time in-service. Previous research and field applications indicate that Fiber Reinforced Polymers (FRP) offer high tensile strength and corrosion resistance as a replacement for steel prestressing strands and reinforcing bars in bridge girders. FRP reinforcement does not corrode, and therefore lasts longer than steel reinforcement. This chapter summarizes milestones in FRP prestressed construction and significant research conducted on the use FRP prestressing systems in bridge girders.

## 2.2 Historical Research and Implementation

The first research project investigating the use of FRP for concrete reinforcement was carried out by the Army Corps of Engineers in 1966. Glass FRP (GFRP) bars were tested in tension to establish their rupture stress and elastic modulus. The bond between the GFRP bars and concrete was tested using different surface preparations. The most efficient surface preparation, coating the bars with epoxy and sand, was used in the casting of concrete beams reinforced with the GFRP bars. The specimens were subjected to short and long term loading. The poor bond between the GFRP and the concrete, coupled with the relatively low modulus of GFRP in comparison to steel, caused failure of the GFRP specimens below their predicted capacity. This investigation showed that FRP had good potential for concrete reinforcement, but that more development of FRP products was necessary (Wines and Hoff 1966).

During the following two decades, extensive research and development of fiber reinforced composites was accomplished in Germany and Japan. The first bridge in the world post-tensioned with FRP was built in Dusseldorf, Germany in 1980. The Lunensche Gasse Bridge, shown in Figure 2.1, was 23 ft. long and had a capacity of 30 tons. The pedestrian bridge was partially stressed with 12 Polystal GFRP tendons manufactured by Bayer. After 5 years it was dismantled for investigation and replaced by a bridge with an updated version of the tendons. Following this success, the Ulenbergstrasse Bridge was constructed in Dusseldorf in 1986 using GFRP post-tensioned tendons. This bridge carried a roadway with spans of 70 and 84 ft. Several other bridges post-tensioned with GFRP tendons were built in Germany and Austria through the early 1990's (Clarke 1993).

**Figure 2.1: Lunensche Gasse Bridge - Dusseldorf, Germany (Clarke 1993)**

The first Carbon FRP (CFRP) prestressed bridge was the Shinmiya Bridge, built in 1988 in Ishikawa Prefecture, Japan. The bridge was 20 ft. long with a 20 ton capacity. Each of the sixteen precast girders was prestressed with eight 0.5 in. diameter Carbon Fiber Composite Cable (CFCC) tendons manufactured by Tokyo Rope (Santoh et al. 1993). The Shinmiya Bridge was built to replace a steel reinforced bridge that had been in service for 20 years and had experienced aggressive corrosion. In 2011, 23 years after its construction, the bridge was inspected and showed no signs of deterioration. Figure 2.2 shows the steel reinforced bridge after being in service for 20 years alongside the CFCC reinforced bridge after being in service for 23 years (Enomoto et al. 2012).

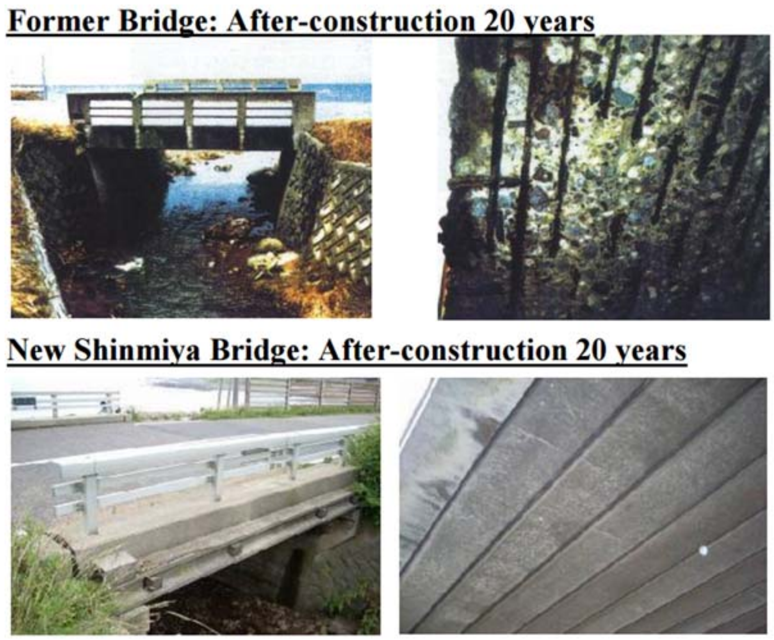


**Figure 2.2: Shinmiya Bridge (Enomoto et al. 2012)**

The first FRP post-tensioned bridge in the United States was built in Rapid City, South Dakota in 1992. The 30 ft. long, 17 ft. wide span was supported by steel girders. The bridge deck was post-tensioned in the transverse direction using steel, GFRP, and CFRP tendons (Iyer 1992).

### 2.3 Prestressing with GFRP

In early applications of FRP prestressing, tendons were partially prestressed. That is, they were stressed to less than 50% of their ultimate strength because their long-term behavior under constant stress was unknown. Feng et al. (1983) tested hundreds of GFRP specimens by stressing them at different increments and observing their behavior over 10 years. The results showed that GFRP bars will fail under sustained load (creep rupture). 100% of the specimens stressed to 75% or more of their rupture stress failed during testing. At 65% capacity, 91% of the samples ruptured, and at 50% capacity, 15% of the specimens failed. This showed that prestressing forces for GFRP must be kept low to prevent creep rupture.

Because FRP is often chosen due to its corrosion resistance, it is important that structures reinforced with FRP have excellent durability. Sen et al. (1993) cast concrete beams prestressed to 40% of their ultimate strength with GFRP strands. Half of the specimens were loaded up their cracking load, and then unloaded. Some beams were left in dry conditions as control specimens and the test specimens were subjected to saltwater spray for 20 months. Beams were removed at 4 month intervals and tested to failure. Cracked and uncracked specimens experienced a complete loss of effectiveness within 9 and 18 months, respectively. Results from the control specimens showed that creep effects were only responsible for a small fraction of this loss of strength. This showed that while Glass FRP does not corrode, GFRP under high sustained stress can degrade severely when exposed to saltwater.

Dolan et al. (2001) conducted tests for creep rupture and durability on GFRP, CFRP and Aramid FRP (AFRP) prestressing strands. Specimens were loaded and exposed to saltwater for 16 months. The report, prepared for the Federal Highway Administration, recommends not using Glass FRP strands for prestressing because of their alkali reactivity and tendency for creep rupture. Testing of a concrete slab prestressed with GFRP tendons by Sovjak et al. (2009) showed that the GFRP also undergoes significant relaxation losses over time. As a result most recent research on prestressed FRP has been focused on CFRP tendons.

### 2.4 Anchors for FRP Strands

The main challenge faced when constructing an FRP prestressed concrete member is the jacking of the FRP strand. The ratio of longitudinal tensile strength to transverse compressive strength for FRP is approximately 20 to 1 (Erki and Rizkalla 1993). Therefore, a standard steel prestressing chuck, which relies on transverse stiffness of the strand, cannot be used to stress FRP strands. Each FRP tendon manufacturer has its own proprietary system for strand anchorage. Nanni et al. (1996) evaluated these anchor systems for ten different aramid, carbon, and glass FRP strand manufacturers. Anchor types included wedge, resin potted, and spike type anchors. An assortment of anchors is shown in Figure 2.3. Only four of the ten anchor systems allowed the strands to reach their rupture stress. The other six anchor types caused the tendons to fail prematurely at the anchorage.

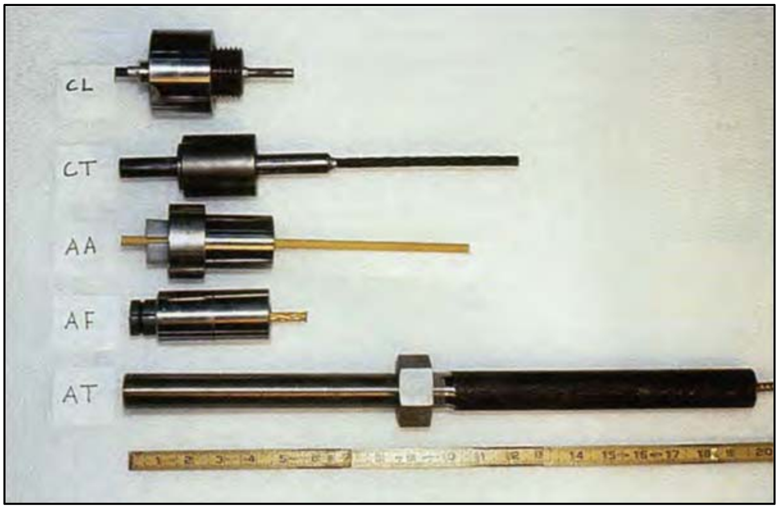


**Figure 2.3: Sample of FRP strand anchorage systems (Ehsani et al. 1997)**

### 2.5 Bond of FRP Strands

The transfer and development lengths of prestressing strands are important design criteria. Much research effort has been put into investigating the bond strength of FRP prestressing strands. Ehsani et al. (1997) cast sixteen concrete specimens with five types of FRP strands and steel strand for a control specimen. Three of the strands were Aramid FRP (AFRP) by several manufactures: Arapree, manufactured by Sireg, FiBRA, manufactured by Fibex, and Technora Rope, manufactured by Pelican Rope. The other two strands were CFRP: Leadline by Mitsubishi Kasei, and CFCC by Tokyo Rope. Transfer length specimens were cast as 10 ft. blocks with strain gages on the strands. Their strain was monitored up to 90 days after casting. Results showed that the transfer length for all of the FRP strands was shorter than for the traditional steel strand. Development length specimens were 20 ft. long and were tested in flexure. The distance from the end of the beam to the point load was varied to test the bond of the strands at the ultimate moment. A tested specimen is shown in Figure 2.4. All of the CFCC strands ruptured during testing without any slip occurring. While the lack of slip indicated good bond, the development length for CFCC was inconclusive because the sections did not reach their maximum moments.

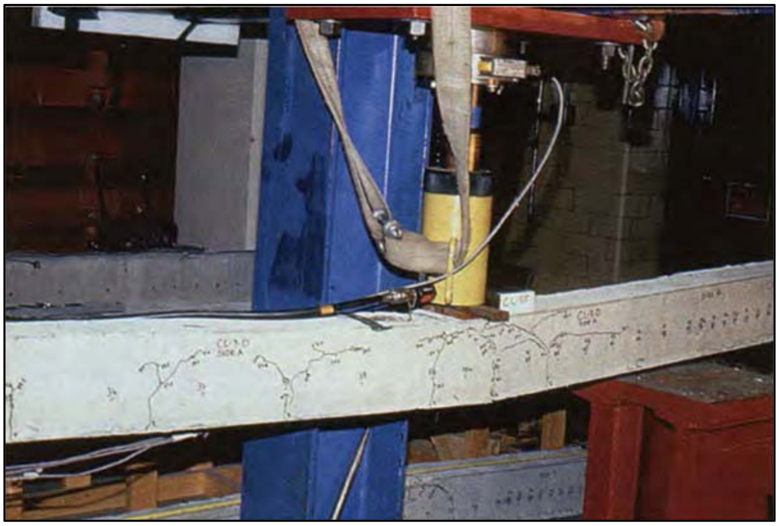

**Figure 2.4: Failed beam after development length test (Ehsani et al. 1997)**

Mahmoud et al. (1999) cast 52 concrete prisms and splice beams to test transfer and development length, respectively. Leadline, CFCC, and steel strands were investigated. Results showed that the presence of shear stirrups decreased the transfer lengths of Leadline and CFCC. Stirrups also decreased the development length of the CFCC. The transfer length of the Leadline increased by 22% after one year, but there was no effect on the CFCC or steel. The bond strength of all materials was greatly affected by concrete strength.

Lu et al. (2000) cast 42 prisms and beams to find the bond strength of Technora, Leadline, a proprietary GFRP bar, and steel strand. The results showed that the FRP strands had a slightly shorter transfer length than steel, and that the transfer length was not affected by the level of prestressing. The ACI 440.4R (2004) equations for predicting transfer and development length were found to be conservative. The authors also commented that the rupture stress of the FRP strands should be used in the transfer and development length equations, as opposed to the stress in the strands at the nominal strength of the section.

Grace (2000) cast eight double tee girders to evaluate transfer and development length: four stressed with Leadline and four stressed with CFCC. The results indicated that the transfer length of Leadline and CFCC is from 47 to 59 strand diameters and from 27 to 38 strand diameters, respectively. It was also found that the amount of prestress in the strand did not affect the transfer length. After one year, all specimens experienced a transfer length increase of approximately 7%.

## 2.6 Flexural Behavior

A traditional steel prestressed beam is designed to fail by crushing of the concrete in the compression zone after the steel has begun to yield. This allows for significant deformation of the beam, and thus warning before failure occurs. Because FRP is fully linear elastic and does not yield, FRP prestressed beams can be designed to fail by one of two failure modes: crushing of the concrete or rupture of the strands. T-beams designed by Abdelrahman et al. (1996) were purposefully designed to fail due to progressive rupture of the CFRP strands. The strands were cast in two layers, as shown in Figure 2.5. As the beam is loaded, the strain increases in the bottom strands until they rupture. This causes a sudden and obvious energy release, which is a warning of impending failure. The load carrying capacity of the section decreases by 50%, and it is loaded until the top layer of strands rupture. Another indication of the impending failure of FRP prestressed beams is a wide distribution of large cracks.

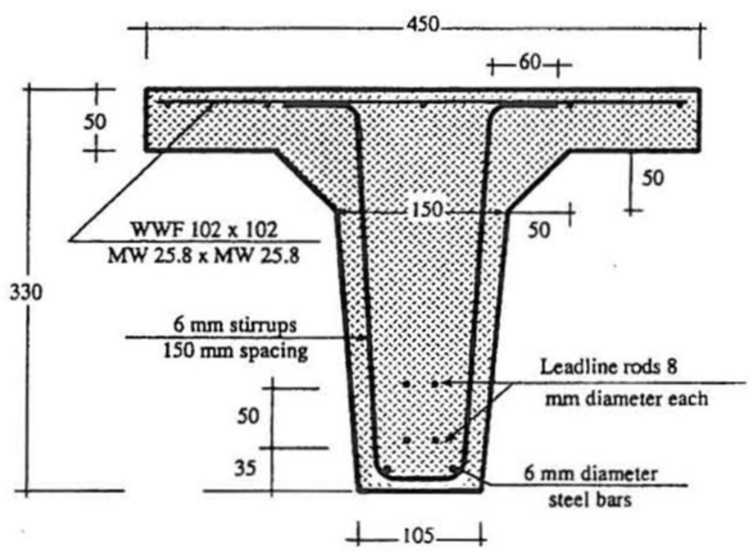


**Figure 2.5: Cross section of T-beams (Abdelrahman et al. 1996)**

Grace et al. (2013a) cast AASHTO-type girders with seven layers of CFRP tendons. These specimens were also designed to fail from progressive rupture of the layers of prestressing. Figure 2.6 shows the load-deflection response of one of the girders. After the layers of tendons ruptured sequentially 5 times, the section still carried almost 50% of its capacity. The girders, which were 41 ft. long and 22 in. deep, deflected 19.7 in. at midspan at failure.

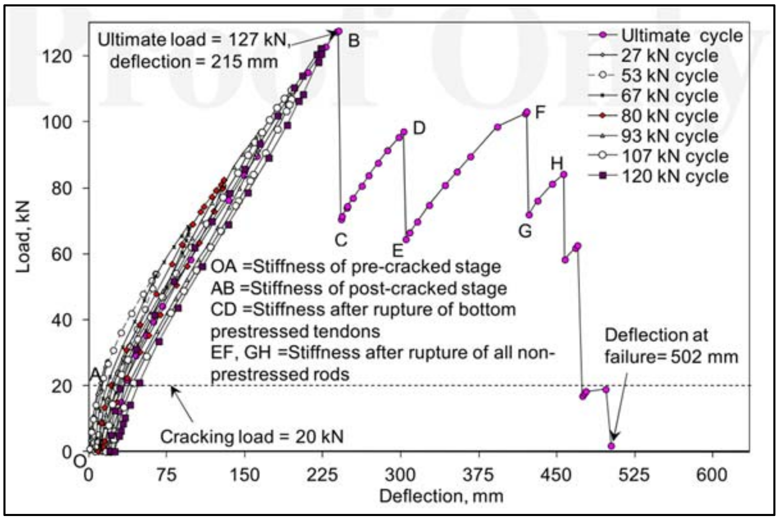


**Figure 2.6: Load-deflection curve for AASHTO girders (Grace et al. 2013a)**

CFRP prestressed beams can also be safely designed to fail from crushing of the concrete in the compression zone. Although CFRP tendons do not yield, they can achieve significant strain before rupture, allowing for large deformation in a section. Grace et al. (2013b) also cast AASHTO-type girders that failed from concrete crushing. The 40 ft. long, 21 in. deep girders reached 11.5 in. of midspan deflection at failure. The prestressing strands were only at 67% of their capacity at failure. A study of CFRP prestressed beam deflection was conducted by Abdelrahman and Rizkalla (1998). Results showed that if steel and FRP reinforced beams are both designed to fail from strand rupture, the steel reinforced beam will deflect considerably more. This is because steel strands rupture at approximately 6% strain, whereas CFRP strands rupture at approximately 2% strain. However, if both steel and FRP reinforced beams are designed to fail by crushing of the concrete, their deflections are quite similar, as shown in Figure 2.7.

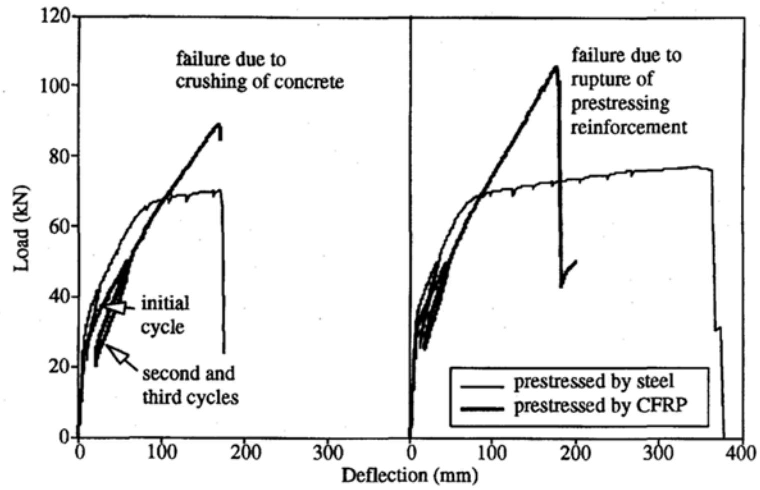


**Figure 2.7: Compression and tension controlled failure modes (Abdelrahman and Rizkalla 1998)**

## 2.7 Fatigue and Durability Response

Although FRP prestressing is more costly than steel, it is chosen because of its durability. Therefore, it is critical that FRP tendons hold up under harsh environmental conditions and cyclic loading. Abdelrahman et al. (1996) found that after two million cycles of loading up to 70%-100% of the cracking load, CFRP prestressed T-beams that were loaded monotonically to failure performed almost the same as a specimen that was not fatigue tested at all. Braimah (2000) subjected steel and CFRP prestressed T-beams to two years of sustained loading. The load induced a moment higher than the cracking moment, and stressed the CFRP strands to 40% of their ultimate capacity. Results showed that the post-cracking stiffness of the CFRP prestressed section is higher than the steel prestressed section. Also, the steel prestressed beam exhibited a higher midspan deflection at the sustained load level.

Rectangular concrete beams prestressed with steel and CFRP tendons were tested under extreme environmental and loading conditions by Mertol et al. (2007). The specimens were subjected to sustained load and heated saltwater spray for 18 months, as shown in Figure 2.8. After the sustained loading period, the specimens were tested with two million cycles of fatigue loading up to 65%-75% of the rupture stress of the strands before being tested monotonically to failure. The steel prestressed beams that were subjected to the sustained loading and saltwater spray failed after 12 months, whereas the CFRP prestressed beams were still intact after 18 months. None of the specimens experienced a major effect from the cyclic loading. The CFRP prestressed specimens did not experience any change in durability or strength from the testing. A higher sustained load decreased the strength of the CFRP specimens slightly, and made the steel specimens more susceptible to environmental effects.

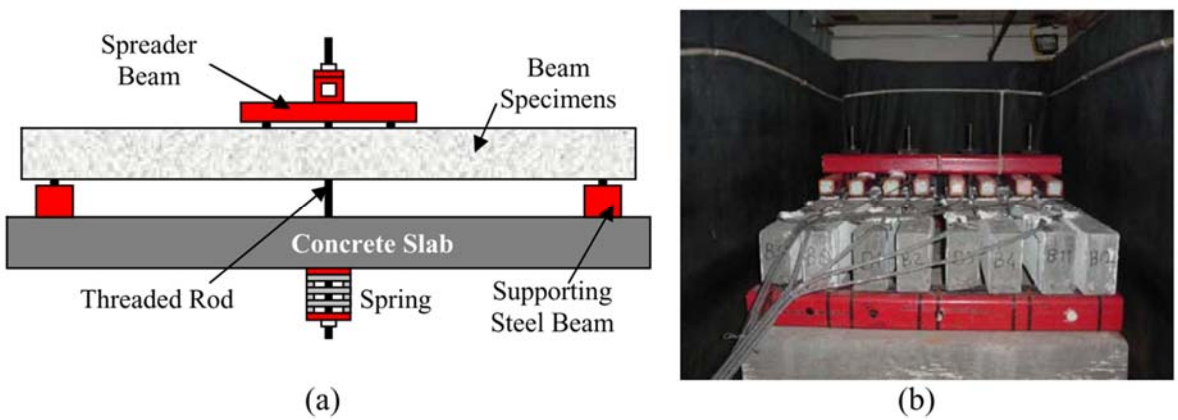


**Figure 2.8: Environmental testing (a) elevation view and (b) in environmental chamber (Mertol et al. 2007)**

T-beams prestressed with steel strands and CFRP rods were cast by Saiedi et al. (2012) to test the effects of cyclic loading at low temperatures. Specimens were subjected to three million cycles of loading at -18°F. The specimens were loaded from just below their decompression stress to their serviceability limit for floor construction. This range was chosen so that cracks would open and close completely during each cycle. The steel beam subjected to low temperatures failed after only 185,000 loading cycles. The CFRP prestressed specimens showed superior fatigue performance to their steel counterparts.

## 2.8 Shear Behavior

### 2.8.1 Beams Prestressed with CFRP

Shear failure is seldom a concern for shallow prestressed beams due to their high span to depth ratio, the axial effect of prestressing, and the minimum stirrup requirements. However, it is important to be able to characterize the shear capacity of a section for design purposes. Research on the shear strength of beams prestressed with FRP is scarce, but growing. Testing was conducted by Tottori and Wakui (1993) on the shear capacity of prestressed beams. Rectangular beams were cast with steel strand and steel stirrups as control specimens. The experimental beams had CFRP tendons and stirrups. Shear tests revealed that shear capacity is a function of the degree of prestress in the section and that the decompression moment could be used to calculate the capacity.

Fam et al. (1997) tested AASHTO-type girders reinforced with CFRP strands and stirrups in shear. The tests were conducted before the implementation of ACI 440.4R (2004), which does not allow for an increase in the shear strength of a beam due to axial prestressing forces. Instead, predictions were made using ACI 318, which did account for the prestressing effect on shear strength. Therefore, the concrete shear strength was overestimated, causing the effective strain in the stirrups to be underestimated. When steel stirrups are used, the concrete contribution to shear strength is greater because of the higher stiffness of steel. The shear cracks formed across steel stirrups are not as wide as they are with CFRP stirrups, and the concrete is able to retain more of its strength. Sixteen years later, more shear tests were conducted on AASHTO-type girders with CFRP tendons and stirrups by Grace et al. (2013b) The experimental values showed that the stirrup design method in ACI 440.4R (2004) gave conservative values for stirrup strain, validating that it is an adequate design process.

Grace et al. (2015) tested bulb T-beams reinforced with CFRP tendons and stirrups in shear. The results showed that the ratio of the actual capacity of the sections to the capacity calculated with ACI 440.4R (2004) ranged from 1.2 to 2.4 with an average of 1.8 and a standard deviation of 0.313. Due to the high level on conservatism in these calculations, a modified AASHTO LRFD method was proposed.

### 2.8.2 Non-Prestressed Beams Reinforced with GFRP Stirrups

Due to the comparatively low stress demand of stirrups in comparison to longitudinal reinforcement in reinforced concrete beams, relatively inexpensive GFRP stirrups are an economical choice in FRP reinforced sections (Shehata et al. 2000). According to ACI 440.1R (2006), FRP stirrups are designed in a method similar to steel stirrups, except that the yield stress of the steel bar is replaced with the tensile design strength of the FRP bar. The design strength is the lower of the stress corresponding to a strain of 0.4%, or the strength of the bent bar. The strain limit is imposed both to retain stability in the section, and to prevent the shear cracks from opening too much, thereby compromising the effectiveness of the concrete contribution to shear strength. When an FRP bar is bent, the cross section is flattened, as shown in Figure 2.9. This significantly reduces the rupture stress of the FRP stirrup (Bank 2007).

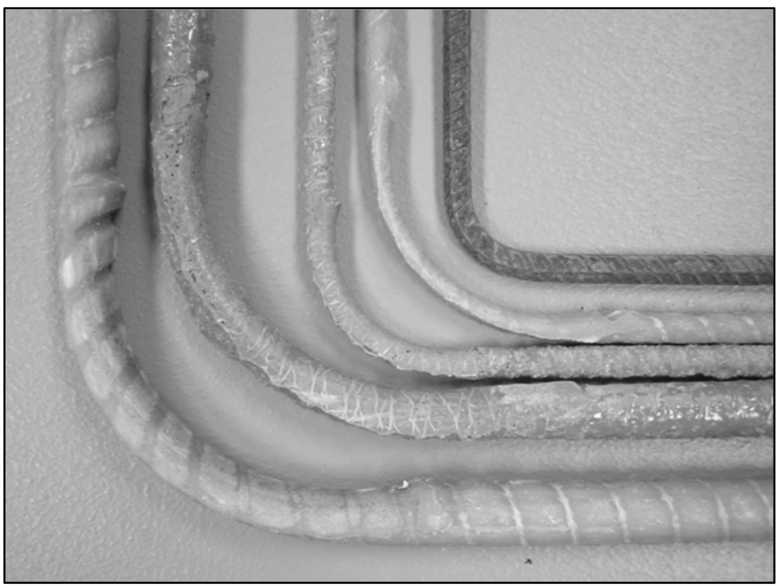

**Figure 2.9: Bent FRP bars with bent steel bar (Bank 2007)**

Nagasaka et al. (1993) cast thirty-five half scale beams reinforced longitudinally with braided AFRP, and transversely with AFRP, CFRP, GFRP, hybrid glass-carbon FRP, and steel stirrups. The beams were tested with monotonically increasing shear force to failure. The concrete strength and shear reinforcement ratio were the principle variables. Tension tests were also conducted on bent FRP bars embedded in concrete specimens. Results showed that the strength of the bars was reduced to 30-80% of the strength of the straight bars. The two failure modes that were observed in the shear tests were rupture of the stirrup at the curved section or crushing of the concrete strut. While the rupture mode was brittle, the crushing mode was relatively ductile. The ultimate shear capacity increased linearly with the shear reinforcement ratio. It was observed that there was not a significant difference in the performance of the different FRP stirrups.

Shehata et al. (2000) tested six beams reinforced transversely with CFRP, GFRP, steel, and no stirrups. Forty additional specially designed specimens were tested to evaluate the bent bar capacity. Results of these tests indicated that the stress capacity of the bent portion of the GFRP bars is approximately 49% of the strength parallel to the fibers. The results of the beam tests showed that due to the relatively lower tensile stiffness of FRP compared to steel, a higher ratio of shear reinforcement is necessary for FRP stirrups to maintain the same crack width as sections reinforced with steel stirrups.

### 2.9 Field Applications

In 1993, the Beddington Trail Bridge, prestressed with CFRP, was built in Calgary, Alberta, Canada. The bridge consisted of two spans of 75 ft. and 63 ft. and was prestressed with CFCC and Leadline strands. The bridge was also outfitted with fiber optic sensors to monitor the behavior of the bridge in service (Rizkalla and Tadros 1994). In 1997, the Taylor Bridge, also prestressed with CFCC and Leadline strands and monitored by fiber optic sensors, was built in Headingley, Manitoba, Canada (Rizkalla et al. 1998). In 1995, at the U.S. Navy's Advanced Waterfront Technology Test Site in Port Hueneme, California, 18 in. deep CFRP prestressed concrete slabs were built as part of a scale model of a pier (Malvar 2000). The Bridge Street Bridge, the first CFRP prestressed bridge in the United States, was built in Southfield, Michigan in 2001. The double tee bridge girders were prestressed with CFCC and Leadline tendons. They were also internally post-tensioned in the transverse direction and externally post-tensioned in the longitudinal direction with CFCC, as shown in Figure 2.10 (Brooks and Cooper 2003).

**Figure 2.10: External CFCC post-tensioning on the Bridge Street Bridge (Brooks and Cooper 2003)**

In 2011, the Pembroke Avenue Bridge, prestressed and post-tensioned with CFCC, was built in Detroit, Michigan. Two more CFCC prestressed and post-tensioned bridges were the M-50/US-127 bridge built in Jackson, Michigan in 2012 and the M-102 bridge over Plum Creek built in Southfield, Michigan in 2013. In 2014, two bridges using the same FRP reinforcement were built in Port Huron, Michigan, and Kittery, Maine (Grace 2014).

In 2012, two piles prestressed with CFCC were cast and driven by the Virginia Transportation Research Council. The behavior of the piles was monitored during and after the driving process to assess their performance. It was determined that the pile design was successful. In 2013, sixteen more piles of the same design were cast, driven, and put into service (Gomez 2014).

The National Cooperative Highway Research Program funded a project at the University of Houston in 2013 with the objective of developing a design guide specification for the design of concrete beams prestressed with CFRP for bridge applications. This guide will be produced in AASHTO LRFD format. The project is ongoing and includes the design, construction, and testing of full-scale bridge beams to validate the guide specification (Hanna 2013).

In 2013, the Louisiana Transportation Research Center externally strengthened the I-10 Littlewood Bridge with CFCC. The original bridge was constructed from prestressed concrete girders whose steel strands had experienced severe corrosion. Load cells were affixed to the

CFRP strands to monitor their behavior after installation (Morvant 2013). As of 2015, plans have been developed for the first FRP reinforced concrete bridge in Florida. The Halls River Bridge in Homosassa will be constructed with CFCC prestressed piles and hybrid composite girders. The pile caps, bridge deck, and guard rails will be reinforced with GFRP rebar (Masséus 2015).

The Virginia Department of Transportation (VDOT) will replace the existing beams of a bridge with CFCC prestressed beams in Halifax County in 2017. Each of the two continuous 85 ft. long spans will consist of four 45 in. tall prestressed bulb tee beams (Ozyildirim 2013a). VDOT will also use CFCC for prestressing strands and spiral reinforcement in the eighteen piles of a new bridge that will be constructed in Virginia Beach in 2019 (Ozyildirim 2013b).

**2.10 Conclusion**

Currently, ACI 440.1R (2006) and ACI 440.4R (2004) are design guides for FRP reinforced and prestressed structures, respectively. The next edition of ACI 318 is expected to include mandatory code language on the use of GFRP reinforcement in concrete structures. The current edition of the AASHTO Bridge Design Manual already includes this language. As mentioned in Section 2.9, development of an AASHTO design guide for FRP prestressed bridges is currently underway.

This project will add to the cumulative knowledge about the bond strength of FRP tendons in comparison to steel tendons discussed in Section 2.5. The experimental program will also provide information about the design and performance of CFRP prestressed beams with GFRP stirrups, which is currently absent in the literature. Results from the shear tests of CFRP prestressed cored slabs will augment the scarce data available on the topic.

# CHAPTER 3: Material Characterization

This chapter describes the material testing that was performed to compare the behavior of the selected FRP materials with steel. Direct tension tests were conducted on samples of the CFRP prestressing strands and GFRP reinforcing bars to evaluate their strength and elastic modulus. Beam-end specimens embedded with CFRP and steel prestressing strands were used to compare the bond strength of each material.

## 3.1 Material Background

CFRP prestressing strands were used for longitudinal reinforcement because of their high strength and stiffness. The product chosen was Carbon Fiber Composite Cable (CFCC) manufactured by Tokyo Rope. Figure 3.1 and Figure 3.2 show a standard steel strand and a CFCC strand. CFCC has the same twisted 7-wire geometry as a steel strand, making it ideal for prestressing applications. The material properties for typical steel prestressing strands and the manufacturer-supplied properties for the CFCC strands are shown in Table 3.1. Due to the brittle failure mode of FRP, the guaranteed rupture stress for the CFCC is significantly lower than the mean rupture stress.

**Figure 3.1: Steel (top) and CFCC (bottom) prestressing strands**

**Figure 3.2: Cross section of steel (left) and CFCC (right) prestressing strands**

**Table 3.1: Material properties of typical steel and CFCC prestressing strands**

| | Guaranteed Rupture Stress (ksi) | Mean Rupture Stress (ksi) | Rupture Strain | Tensile Modulus (ksi) |
|---|---|---|---|---|
| Steel Strand | 270 | 282 | 6.0% | 29000 |
| CFCC | 339 | 463 | 2.1% | 21900 |

GFRP bars were chosen to replace the mild steel rebar used as stirrups and the top reinforcement because the stress requirements are not high in these zones, and the cost of GFRP is significantly less than CFRP. The GFRP material chosen was Aslan 100 GFRP rebar manufactured by Hughes Brothers, shown in Figure 3.3 with steel rebar. Material properties of the steel and Aslan 100 bar as given by the manufacturer are summarized in Table 3.2.

**Figure 3.3: Steel (top) and GFRP (bottom) rebar**

**Table 3.2: Material properties of steel and GFRP rebar**

| | Yield Stress (ksi) | Rupture Stress (ksi) | Rupture Strain | Tensile Modulus (ksi) |
|---|---|---|---|---|
| Steel Rebar | 60 | 90 | > 10% | 29000 |
| Aslan 100 | N/A | 105 | 1.6% | 6700 |

## 3.2 Direct Tension Tests

### 3.2.1 CFRP Prestressing Strands

Six tension specimens of 0.6 in. diameter CFRP prestressing strand were fabricated by the manufacturer and sent to the Constructed Facilities Laboratory. The specimens were 4 ft. long, and had 1 ft. long steel sleeves filled with expansive material attached to each end. These sleeves allowed the laboratory testing machine to grip the specimen in the transverse direction without locally damaging the strands. The sleeves were necessary because unlike steel which can be gripped directly by the testing machine, FRP is anisotropic. While it has high strength in longitudinal tension, it is weak in transverse compression. A cross section of the sleeve assembly, provided by the manufacturer, is shown in Figure 3.4.

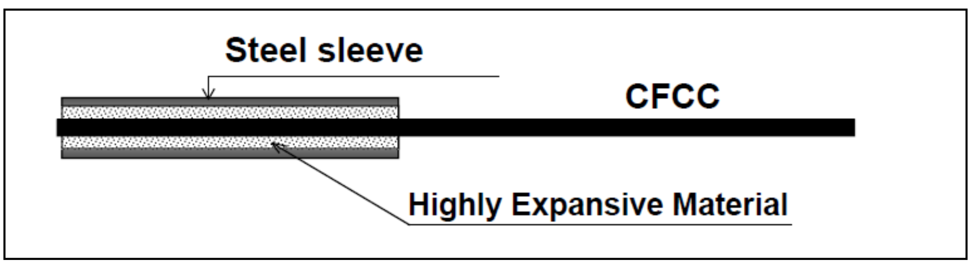


**Figure 3.4: Diagram of CFRP with sleeves installed**

Two methods were used to measure strain in the strand during testing. The first method was the use of a uniaxial strain gage. First, the surface of the CFRP was carefully sanded down to expose a smooth contact surface, as shown in Figure 3.5. Then, the strain gage was applied to the strand, and covered with polyurethane to prevent damage during loading into the test machine. A CFRP specimen with a strain gage attached is shown in Figure 3.6.

**Figure 3.5: Strand surface after sanding**

**Figure 3.6: CFRP specimen with strain gage**

Strain gages were used to measure the strain of the first two CFRP specimens. However, during testing, the strain gage debonded at 40% and 60% of ultimate stress for the first two tests, respectively. For the remaining tests, an extensometer was used to measure the axial strain in the specimen. However, due to the violent nature of CFRP rupture, the extensometer was removed when the load reached 70% of the ultimate. Also, a Plexiglas tube was placed around the specimens to prevent the fibers from exploding out into the lab during failure. Figure 3.7 shows a specimen loaded into the testing machine inside the clear plastic tube.

**Figure 3.7: CFRP specimen (inside Plexiglas tube) with an extensometer**

CFRP specimens were loaded monotonically at a rate of 0.05 in/min. The failure mode was rupture for each specimen. A tested specimen is shown in Figure 3.8. Although strain data were only collected for the first 40% - 70% of the loading curve, the force at rupture was known, so the stress-strain curve was extrapolated to the failure stress. Due to the elastic nature of FRP, the slope of the line was assumed to be the same for the duration of loading until rupture.

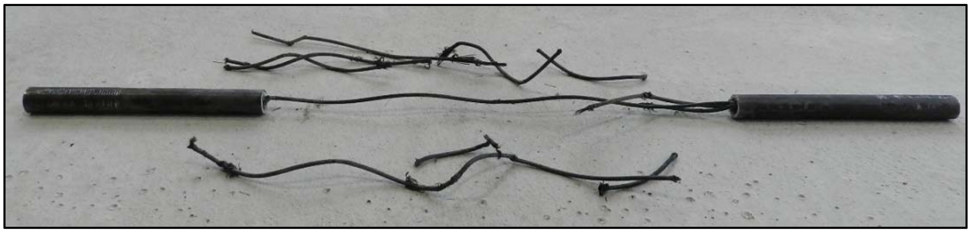

**Figure 3.8: CFRP tension specimen after testing**

Table 3.3 shows the results from the six tension tests, the values given by the manufacturer, and the percent difference between the average of the experimental tests and the given manufacturer values. Young's modulus was calculated using two points on the stress-strain curve. The rupture strain was calculated by dividing the rupture stress by the Young's modulus. The material properties obtained from laboratory testing verified the accuracy of the manufacturer's values.

**Table 3.3: Results from CFRP tension tests**

| Test # | Rupture Load (k) | Rupture Stress (ksi) | Young's Modulus (ksi) | Rupture Strain |
|---|---|---|---|---|
| 1 | 84.1 | 469.7 | 22010 | 2.13% |
| 2 | 77.3 | 431.8 | 20941 | 2.06% |
| 3 | 83.1 | 464.3 | 21741 | 2.14% |
| 4 | 84.5 | 472.0 | 21322 | 2.21% |
| 5 | 84.9 | 472.3 | 23938 | 1.97% |
| 6 | 81.1 | 453.1 | 21926 | 2.07% |
| Standard Deviation | 2.9 | 15.8 | 1040 | 0.08% |
| Average | 82.5 | 460.5 | 21980 | 2.10% |
| Data from Manufacturer | 83.0 | 462.7 | 21900 | 2.11% |
| % Difference | -0.61% | -0.47% | +0.36% | -0.80% |

### 3.2.2 GFRP Reinforcing Bars

Direct tension tests were also performed on six No. 5 GFRP tension specimens. These specimens were 4 ft. long with 7 in. long steel sleeves on each end installed by the manufacturer using a mechanical process.  As was the case with the CFRP strand, these sleeves are necessary to grip the specimen without damaging it during testing.  One of these specimens is shown in Figure 3.9.

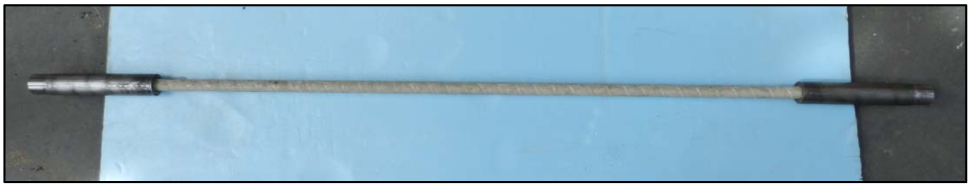

**Figure 3.9: GFRP specimen prior to testing**

To measure strain during testing, an extensometer was attached to the specimen.  Rupture of the GFRP bars was not as explosive, so no protective tube was used for these tests.  A specimen loaded into the MTS machine and ready for testing is shown in Figure 3.10.

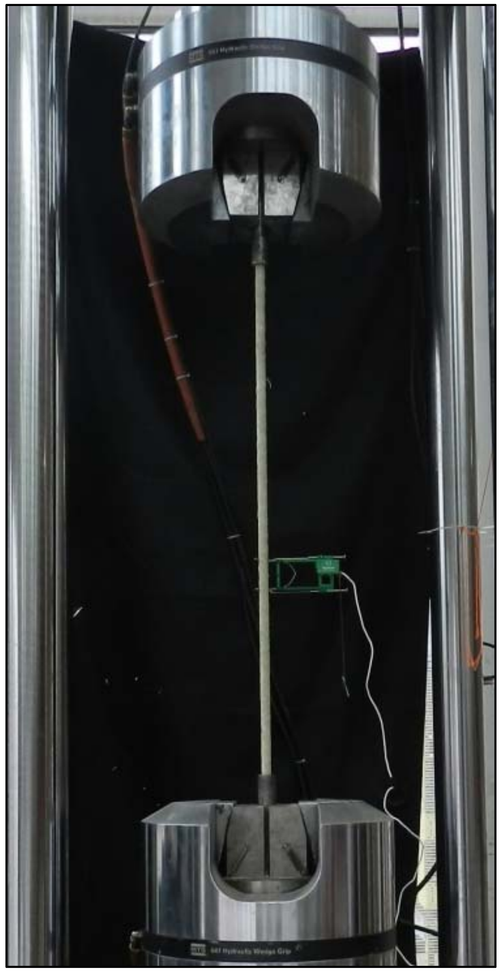

**Figure 3.10: GFRP specimen loaded into MTS machine**

The GFRP bars were also loaded monotonically at a rate of 0.05 in./min until failure. The extensometer was removed at around 70% of the peak load, to prevent damage during rupture. As with the CFRP strand, fully elastic behavior of the bars allowed the full stress-strain relationship to be obtained from the strain measurement of the first 70% of the loading curve. While the specimens did not rupture in an explosive manner, failure was sudden and caused the bars to splinter, as shown in Figure 3.11.

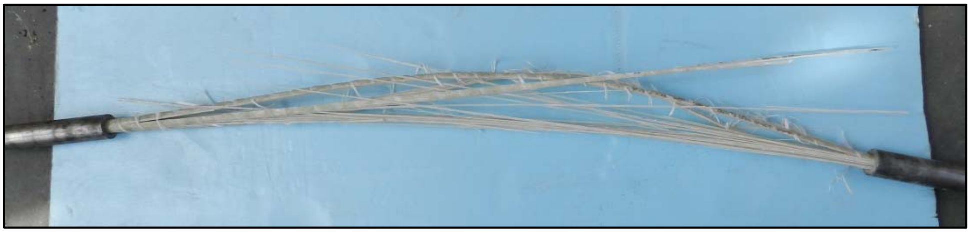

**Figure 3.11: GFRP specimen after testing**

The results from the six tension tests, the given values from the manufacturer, and the percent difference between the average of the experimental tests and the manufacturer values are shown in Table 3.4. Note that for the first test, the extensometer was not properly attached to the bar, and no strain data are available for that test. The values supplied by the manufacturer closely matched experimental results.

**Table 3.4: Results from GFRP tension tests**

| Test # | Rupture Load (k) | Rupture Stress (ksi) | Young's Modulus (ksi) | Rupture Strain |
|---|---|---|---|---|
| 1 | 34.2 | 111.5 | -- | -- |
| 2 | 34.0 | 110.9 | 6235 | 1.78% |
| 3 | 34.2 | 111.5 | 6403 | 1.74% |
| 4 | 32.4 | 105.7 | 5965 | 1.77% |
| 5 | 33.2 | 108.2 | 6074 | 1.78% |
| 6 | 33.8 | 110.1 | 6281 | 1.75% |
| Standard Deviation | 0.7 | 2.3 | 173 | 0.02% |
| Average | 33.7 | 109.6 | 6192 | 1.76% |
| Data from Manufacturer | 32.2 | 105.0 | 6700 | 1.57% |
| % Difference | +4.39% | +4.40% | -7.59% | +12.41% |

### 3.2.3 Comparison of CFRP and GFRP

Figure 3.12 shows the stress-strain graphs from all CFRP and GFRP tension tests. The solid lines represent the part of the test for which strain data were collected. The dashed lines represent perfectly linear behavior with the average Young's modulus and rupture stress from all tests.

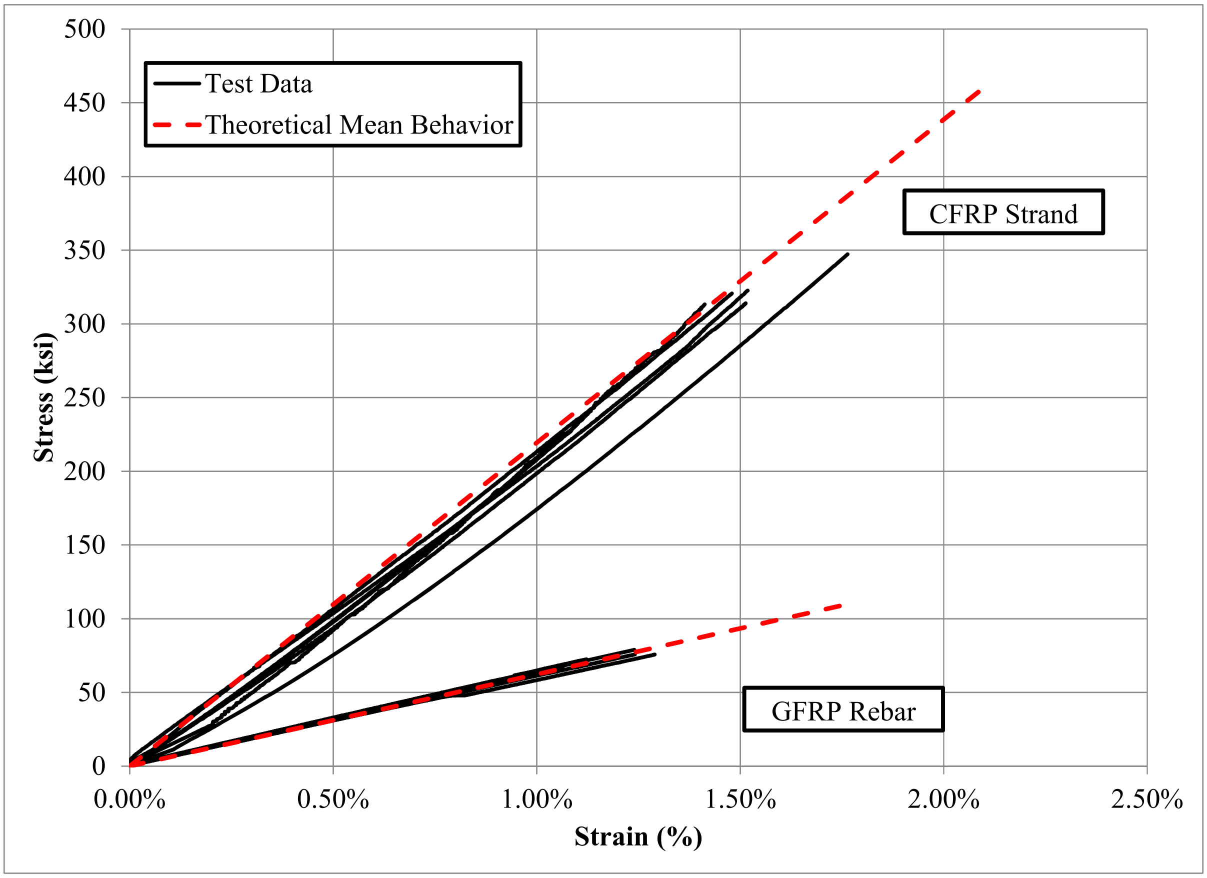


**Figure 3.12: Stress-strain graph for CFRP and GFRP tension tests**

### 3.2.4 Comparison with Steel

The stress-strain behavior of the CFRP strands and GFRP bars using the average values from experimental testing is shown in Figure 3.13, along with the typical behavior of 270 ksi ASTM A416 steel prestressing strand and grade 60 ASTM A615 steel rebar. For both prestressing strand and rebar, the FRP reinforcement has a higher rupture stress, but a lower rupture strain.

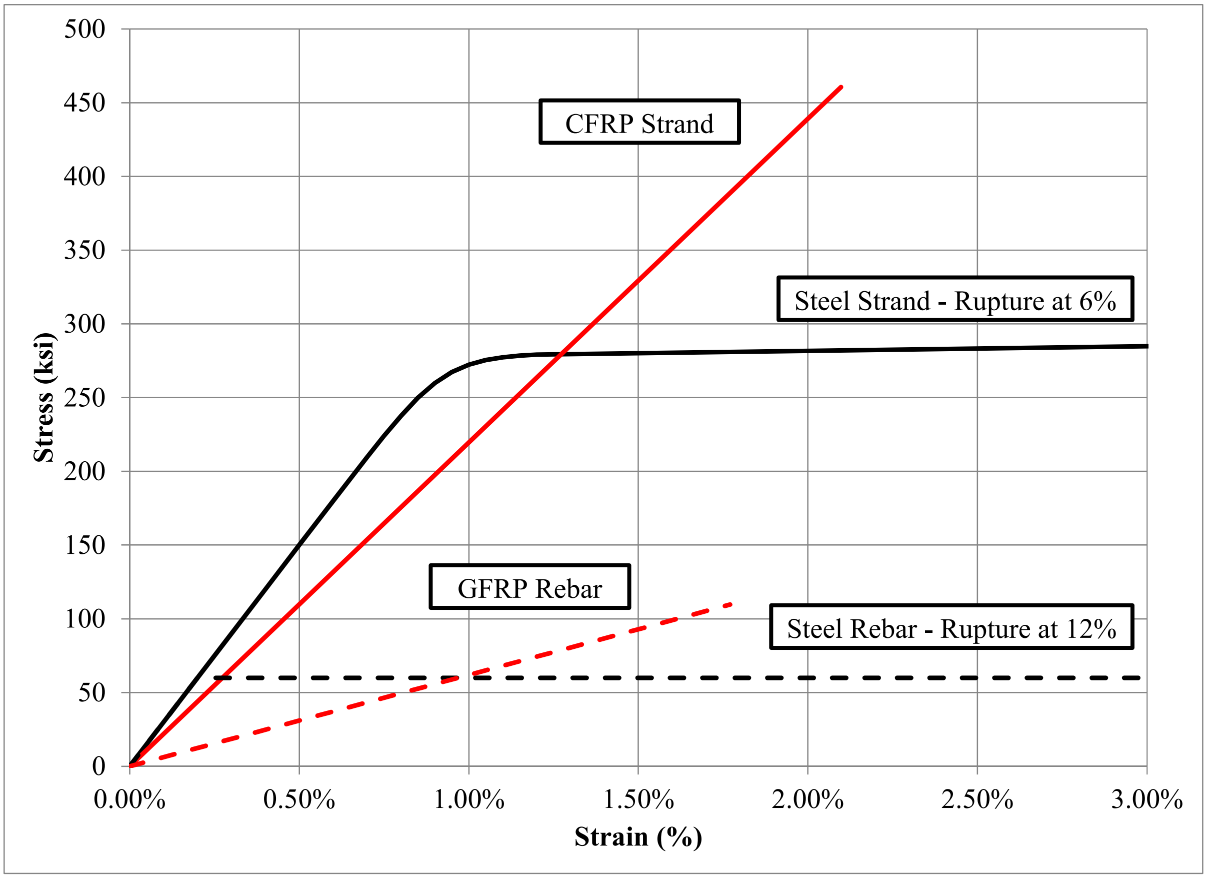


**Figure 3.13: Stress-strain comparison of CFRP, GFRP, and steel**

The mechanical properties given by the manufacturers were used for the initial design of the cored slabs in the testing program. Experimental results from material testing were used for analysis to predict experimental behavior of the cored slabs.

### 3.3 CFRP Bond Strength Testing

Beam-end tests are used to evaluate the strength of the bond between reinforcement and the concrete that surrounds it. Ten beam-end specimens were designed, fabricated, tested, and analyzed to evaluate the bond strength of the CFRP prestressing strand in comparison to steel prestressing strand.

### 3.3.1 Development Length Calculations

The predicted flexural bond length, $L_{fb}$, for the CFRP strand was calculated using the following ACI 440.4R (2004) equation:

$$L_{fb} = \frac{(f_{pu} - f_{pe})\, d_b}{\alpha_{fb}\, {f'_c}^{0.67}} \tag{3.1}$$

where $f_{pu}$ is the rupture stress, $f_{pe}$ is the effective prestress in the strand, which for these non-prestressed specimens was zero, $d_b$ is the diameter of the CFRP strand, $\alpha_{fb}$ is an adjustment factor for units and CFRP strand manufacturer (for in.-lb units and CFCC, $\alpha_{fb}$ is 14.8), and $f'_c$ is the 28 day concrete strength. For the strands used in this experimental program, the predicted flexural bond length was 52 in., or approximately 87 $d_b$. Typically, $L_{fb}$ is added to the transfer length, $L_t$, to find the development length, $L_d$. However, because the strands in these specimens were not prestressed, $L_{fb}$ was taken to be equal to $L_d$.

Prestressed reinforcement has better bond characteristics than non-prestressed reinforcement due to both compression of the concrete surrounding the strand, and the Hoyer effect (Domenico et al. 1998). Because the ACI 440.4R (2004) equation was developed for prestressed strands, the actual development length was expected to be longer. To calculate the development length for non-prestressed reinforcement, the following equation for FRP bars from ACI 440.1R (2006) was used:

$$L_d = \frac{\alpha \frac{f_{fr}}{\sqrt{f'_c}} - 340}{13.6 + \frac{C}{d_b}}\, d_b \tag{3.2}$$

where $\alpha$ is a top-cast factor, $f_{fr}$ is the required stress in the bar, and $C$ is the distance from the center of the bar to the face of the concrete. The $L_d$ calculated for the CFRP strands was 170 in., or approximately 283 $d_b$. This value exceeds a reasonable development length because the $f_{fr}$ value was set equal to the rupture stress of the CFRP strands, 461 ksi. Equation (3.2 was developed for use with standard FRP bars, which have significantly lower rupture stress values than CFRP strands. Given these theoretical values, the experimental development length of the CFRP strands was expected to be greater than 87 $d_b$.

ACI 318 (2011) gives the following equation for the development length of non-prestressed deformed bars or wire smaller than 7/8 in. in diameter, with spacing greater than $d_b$, in tension:

$$L_d = \frac{f_y \psi_t \psi_e}{25\,\lambda \sqrt{f'_c}}\, d_b \tag{3.3}$$

where $f_y$ is the yield stress of the strand (in this case the rupture stress was used instead), $\psi_t$ is a top-cast factor, $\psi_e$ is a bar coating factor, and $\lambda$ is a lightweight concrete factor. The predicted development length using this equation is 80 in. or 134 $d_b$.

The calculated values for the expected experimental development lengths for non-prestressed strands were used in the design of the beam-end specimens.

### 3.3.2 Experimental Plan

The standard for testing beam-end specimens is given by ASTM A944 (2010). The procedure involves casting concrete blocks with a selected length of reinforcement bonded to the concrete in each block. The reinforcement extends out the end of the block so that it can be gripped and pulled out of the specimen, simulating what happens to reinforcement inside a beam. When a tensile load is applied to the reinforcement being tested, the test setup reacts with a compressive force against the bottom of the specimen. In this way, the block is acting like an upside-down half of a beam. Each specimen is tested until either pullout or rupture failure occurs. If the reinforcement pulls out, then the bonded length tested is less than $L_d$. If the reinforcement ruptures, then the bonded length tested is greater than $L_d$.

The ten specimens were cast and tested in two phases. Because no experimental values for beam-end tests with non-prestressed CFRP strands were available in the literature, the first phase specimens were cast with a varied range of bonded lengths to establish a narrower range around $L_d$. The second phase specimens were cast with variation kept in this range. Specimens with steel strands were only cast and tested in phase two.

### 3.3.3 Phase 1

#### 3.3.3.1 Beam-End Specimen Design

The first phase of specimens covered a wide breadth of bonded lengths, from 33 to 150 $d_b$, as shown in the test matrix in Table 3.5.

**Table 3.5: Beam-end phase 1 test matrix**

| Specimen ID | Bonded Length (in) | Bonded Length ($d_b$) |
|---|---|---|
| 1 | 20 | 33 |
| 2 | 30 | 50 |
| 3 | 45 | 75 |
| 4 | 65 | 108 |
| 5 | 90 | 150 |

The CFRP strands used for these specimens were prepared by the manufacturer. Each strand was 12 ft. long with a 1 ft. steel anchor on one end (see Figure 3.4). The anchor end of the strand protruded from the surface of the concrete by 3 ft. as illustrated in Figure 3.14, to allow the strand to be pulled by a hydraulic jack. PVC pipe segments were used to debond the first 6 in. of strand from the block, to prevent a cone-type failure of the concrete. Another PVC pipe was used at the back end of the block to expose the end of the strand for slip measurement, to prevent anchorage from compressive stresses due to the block restraint, and to vary the bonded length in each specimen. The variable geometry of each specimen is shown in Table 3.6. In order to prevent a top-cast effect of weaker concrete around the strand, the specimen was cast with the strand on the bottom and flipped over before testing. Two transverse PVC pipes were cast in the specimen to allow for lifting.

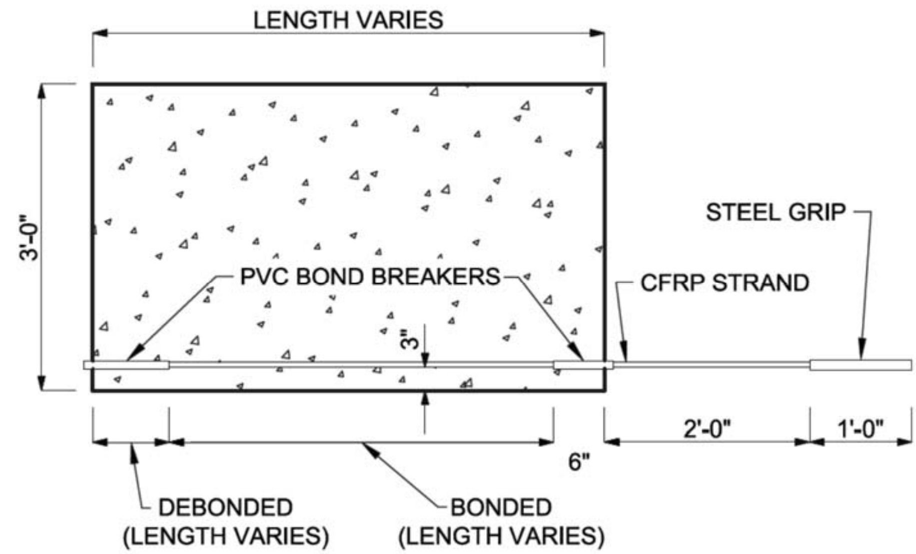


**Figure 3.14: Phase 1 CFRP strand layout schematic in as-cast orientation**

**Table 3.6: Beam-end phase 1 specimen geometry**

| Specimen ID | Block Length (ft) | Bonded Length (in) | Debonded Length (in) |
|---|---|---|---|
| 1 | 5 | 20 | 34 |
| 2 | | 30 | 24 |
| 3 | | 45 | 9 |
| 4 | 9 | 65 | 37 |
| 5 | | 90 | 12 |

Test specimens were designed to follow ASTM A944 (2010) as closely as possible, however, due to the high strength of the CFRP strands, the dimensions of the concrete blocks were increased. Concrete blocks having shorter bonded lengths were 5 ft. long, while blocks with longer bonded lengths were 9 ft. long. To ensure that the strain in the compression zone of the concrete would remain well below the crushing strain of 0.3% when the CFRP reached its rupture stress, the blocks were designed to be 3 ft. tall. To prevent cracking in the concrete surrounding the strands, two No. 8 flexural steel reinforcing bars were used. Although shear was not expected to be a factor, No. 3 shear stirrups spaced at 8 in. were also used. ASTM A944 (2010) designates that in order to prevent confinement of the test strand, no reinforcing bars should be cast in the horizontal direction perpendicular to the strand being tested. Therefore, two independent mats of reinforcing steel were cast on either side of the strand, as shown in Figure 3.15. Schematics of the design of the 5 and 9 ft. blocks are depicted in Figure 3.16 and Figure 3.17, respectively.

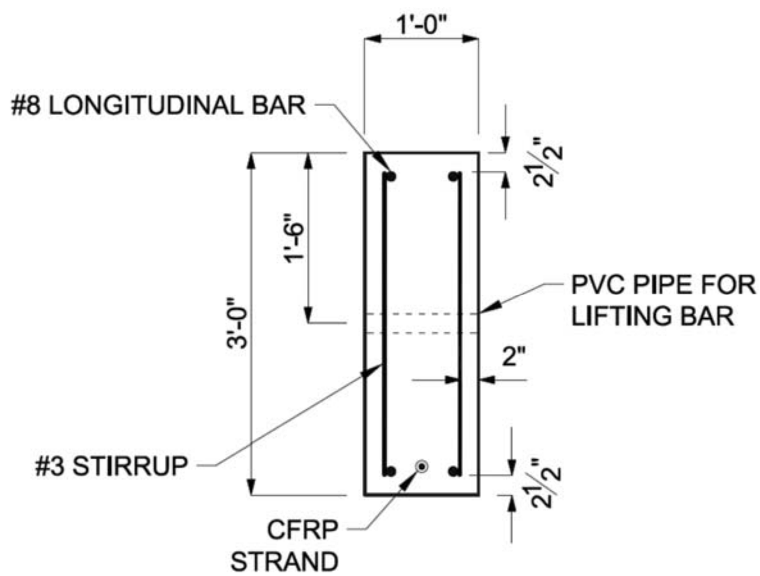


**Figure 3.15: Cross section of phase 1 reinforcement**

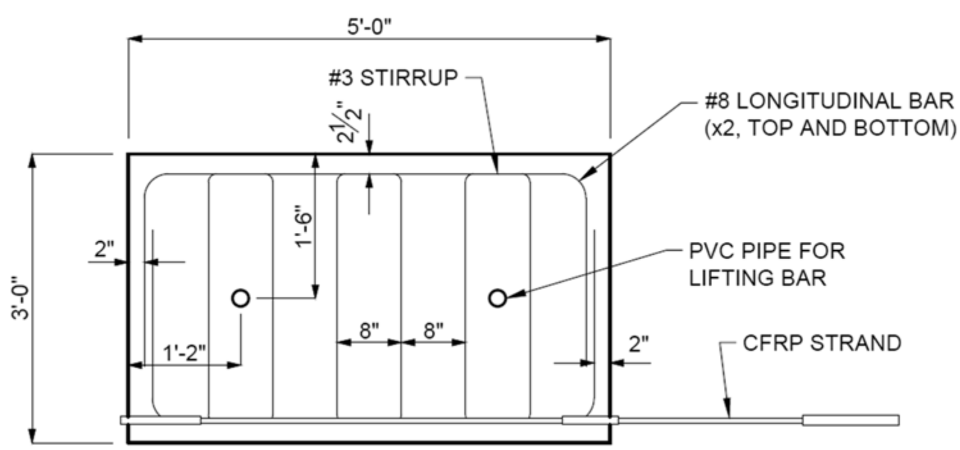


**Figure 3.16: Elevation view of phase 1 reinforcement (5 ft. block)**

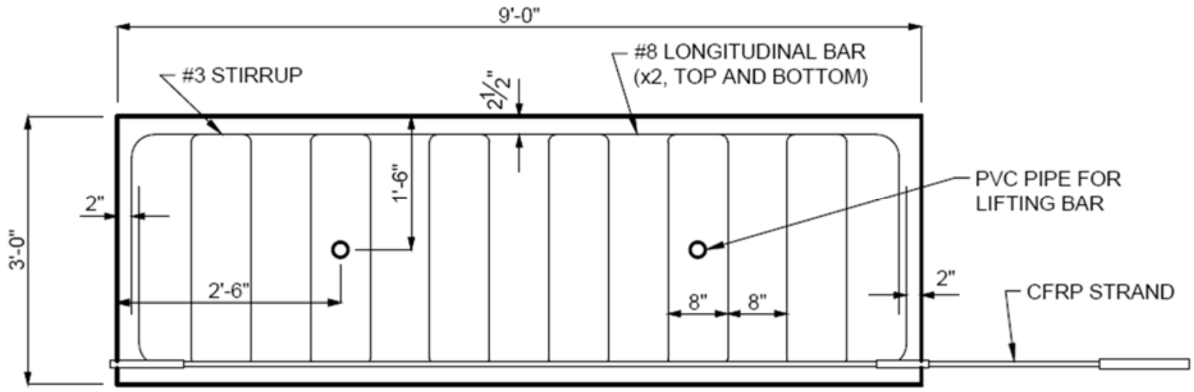


**Figure 3.17: Elevation view of phase 1 reinforcement (9 ft. block)**

### 3.3.3.2 Beam-End Specimen Fabrication

Beam-end specimens were cast in forms assembled from steel-ply panels, plywood, and PVC pipe. The flexible CFRP strand was kept in position with plastic chairs that were stapled to the formwork. Rebar mats were tied outside of the forms, then placed into the forms, as illustrated in Figure 3.18. Completed formwork ready for casting is shown in Figure 3.19.

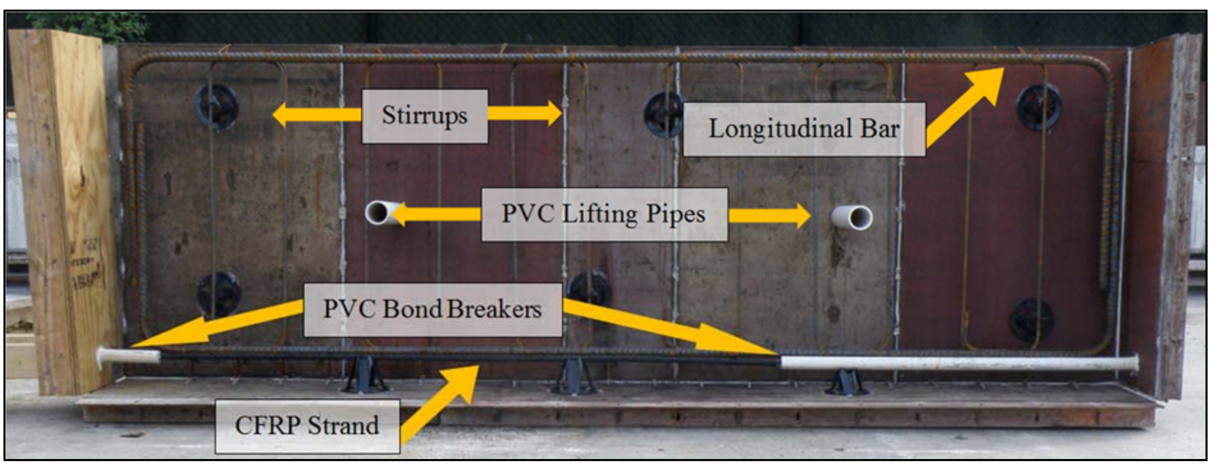


**Figure 3.18: Formwork with one side missing**

**Figure 3.19: Phase 1 formwork before casting**

The specimens were cast with a 5000 psi concrete from a local supplier. The forms were filled halfway, then consolidated with a vibrator. Care was taken to ensure that the corners of the specimen were thoroughly consolidated. Cast specimens are depicted in Figure 3.20. Several 4 in. x 8 in. test cylinders were cast simultaneously with the blocks. After the initial set, curing compound was applied to the top surface of the concrete. Seven days after casting, the formwork was stripped and the test cylinders were removed from their molds.

**Figure 3.20: Phase 1 specimens after casting**

### 3.3.3.3 Beam-End Testing and Results

A test setup was fabricated to restrain the beam-end specimen during testing and to apply tension to the exposed strand. A steel assembly tied to the laboratory strong floor was used to hold the specimen and to provide reaction points, as shown in Figure 3.21. A linear potentiometer was attached at the left end of the block to measure the slip of the strand during testing. Three linear potentiometers were placed around the strand at the right end of the specimen 120° from each other. The average of the three potentiometer readings gave the extension of the exposed strand. A schematic and photograph of this test setup are shown in Figure 3.21 and Figure 3.22, respectively.

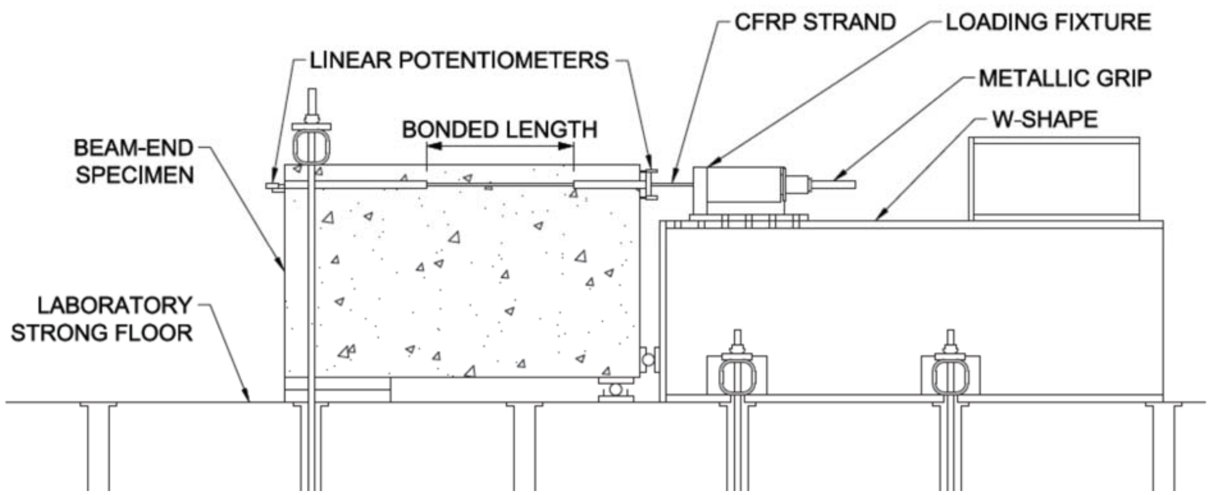


**Figure 3.21: Beam-end test setup schematic**

**Figure 3.22: Beam-end test setup in the laboratory**

After the specimen was loaded into the test setup, a steel plate and a chuck supplied by the CFRP manufacturer, shown in Figure 3.23, was placed on the steel sleeve to grip the strand. The hydraulic jack was loaded at a rate of 0.25 in/min. Loading continued until the strand ruptured or slipped. Slipping was defined by any significant measurement read from the left end potentiometer (> 0.1 in.) accompanied by a decrease in load.

**Figure 3.23: Plate and chuck used to grip CFRP strand**

Results from the five tests of phase 1 are depicted in Figure 3.24. Specimen 5 (150 $d_b$ bond length) ruptured at a load of 75.1 kips, 9.0% lower than the average rupture load of 82.5

kips from tension testing. The other specimens failed by strand pullout. A linear regression of the tests that failed from pullout yielded the black trendline on the graph in Figure 3.24. The experimental $L_d$ is the intersection of the black trendline and the red rupture limit. This experimental development length ($L_d$) is represented by the blue dot at 118 times the bar diameter (118*$d_b$). The average concrete cylinder strength at the time of testing was 6300 psi.

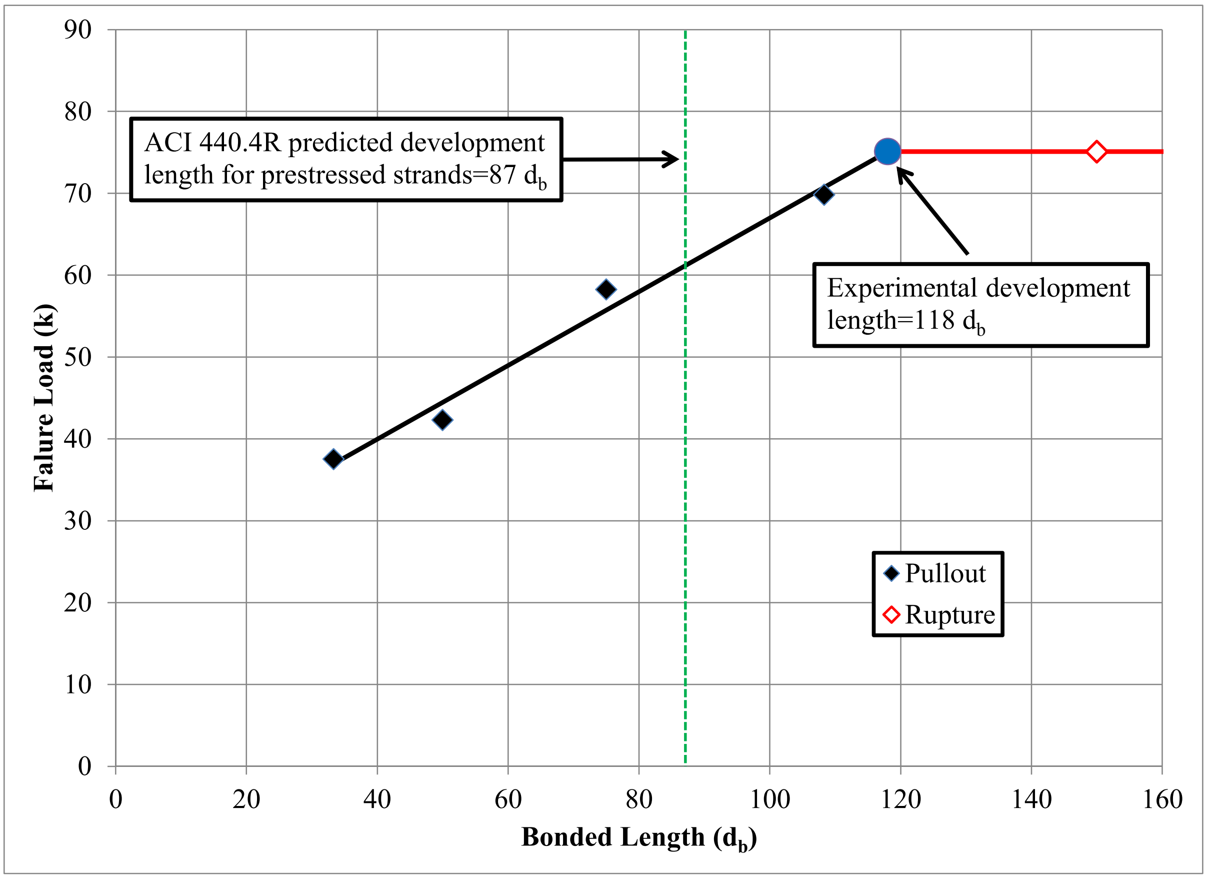


**Figure 3.24: Phase 1 bond strength results**

### 3.3.4 Phase 2

#### 3.3.4.1 Beam-End Specimen Design

Due to the results of phase 1 testing, additional beam-end specimens were designed in increments of 5 strand diameters, from 115 to 135 $d_b$. The specimens were also cast with a steel strand embedded on the other side of the block. This allowed each specimen to be tested twice, to allow for comparison between the bond strength of the CFRP and traditional steel strands. The calculated value from ACI 318 (2011) for the $L_d$ of steel strands was 134 $d_b$. Therefore, bonded lengths for the steel strands were varied in increments of 10 strand diameters, from 110 to 150 $d_b$. All blocks were 9 ft. long in this phase. The second phase test matrix is summarized in Table 3.7.

**Table 3.7: Beam-end phase 2 test matrix**

| | CFRP | | Steel | |
|---|---|---|---|---|
| Specimen ID | Bonded Length (in) | Bonded Length ($d_b$) | Bonded Length (in) | Bonded Length ($d_b$) |
| 6 | 69 | 115 | 66 | 110 |
| 7 | 72 | 120 | 72 | 120 |
| 8 | 75 | 125 | 78 | 130 |
| 9 | 78 | 130 | 84 | 140 |
| 10 | 81 | 135 | 90 | 150 |

In order for the specimens to be loaded into the test setup, the strands had to face different directions. This strand layout is shown in Figure 3.25 with other reinforcement details excluded from the drawing for clarity.

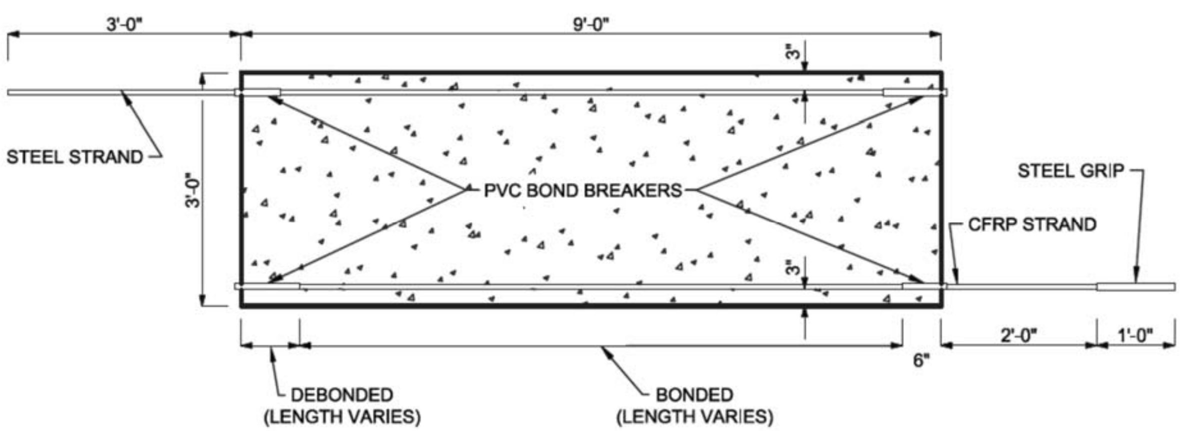


**Figure 3.25: Phase 2 strand layout schematic**

In order to negate the top-cast effect that would cause different concrete strengths in the top and bottom of the specimen, and for ease of construction, the specimens were cast on their sides, and turned prior to testing. To suspend the top mat of steel in the forms, two straight 10 ft. long No. 4 casting support bars were run through holes in the ends of the forms, as illustrated in Figure 3.26 and Figure 3.27.

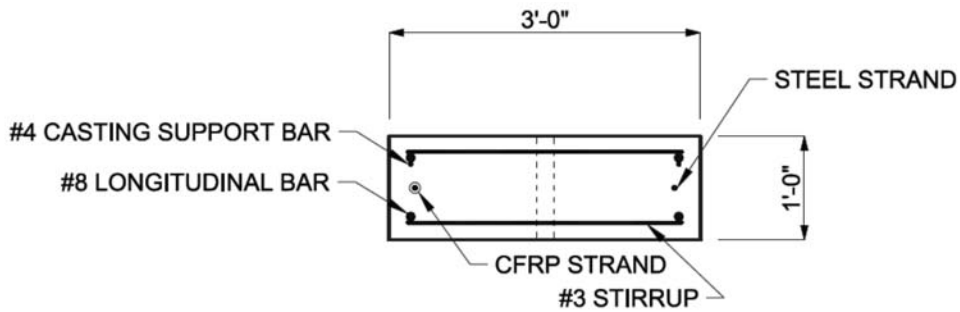


**Figure 3.26: Cross section of phase 2 reinforcement (casting orientation)**

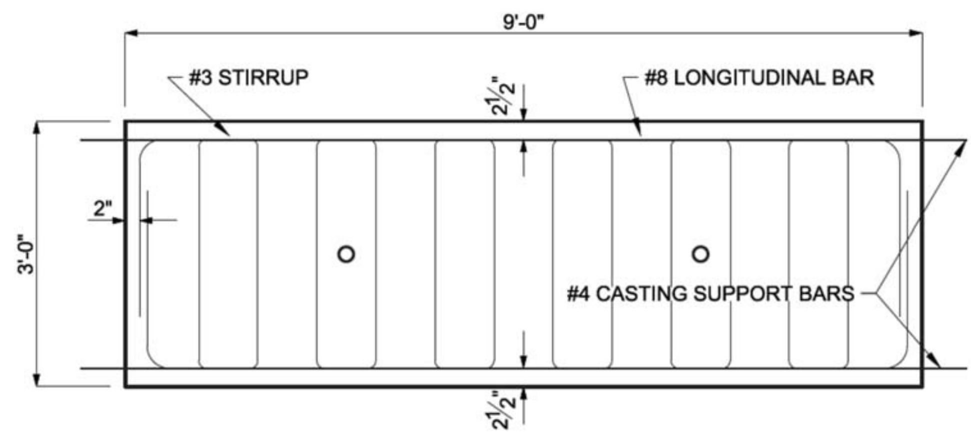


**Figure 3.27: Plan view of phase 2 reinforcement (strands not shown for clarity)**

### 3.3.4.2 Beam-End Specimen Fabrication

Figure 3.28 and Figure 3.29 show formwork ready for casting and the specimens after casting, respectively.


**Figure 3.28: Phase 2 formwork before casting**

**Figure 3.29: Phase 2 specimens after casting**

### 3.3.4.3 Beam-End Testing and Results

The testing procedure was the same as for the phase 1 blocks. After the first test on a given block, it was flipped over, turned around, and placed back into the setup. Care was taken not to damage the exposed strands during handling. A standard steel prestressing chuck, depicted in Figure 3.30, was used to grip the steel strand. The steel strand was loaded at a rate of 0.4 in./min.

**Figure 3.30: Steel prestressing chuck**

Results from the phase 2 tests on the CFRP strands are added to the results from phase 1 in Figure 3.31. All five of the strands ruptured. The average rupture load was 85.4 kips. The average concrete cylinder strength at the time of testing was 6500 psi. Based on these results, it is assumed that $L_d$ is between 108 and 115 $d_b$ for the CFRP strand.

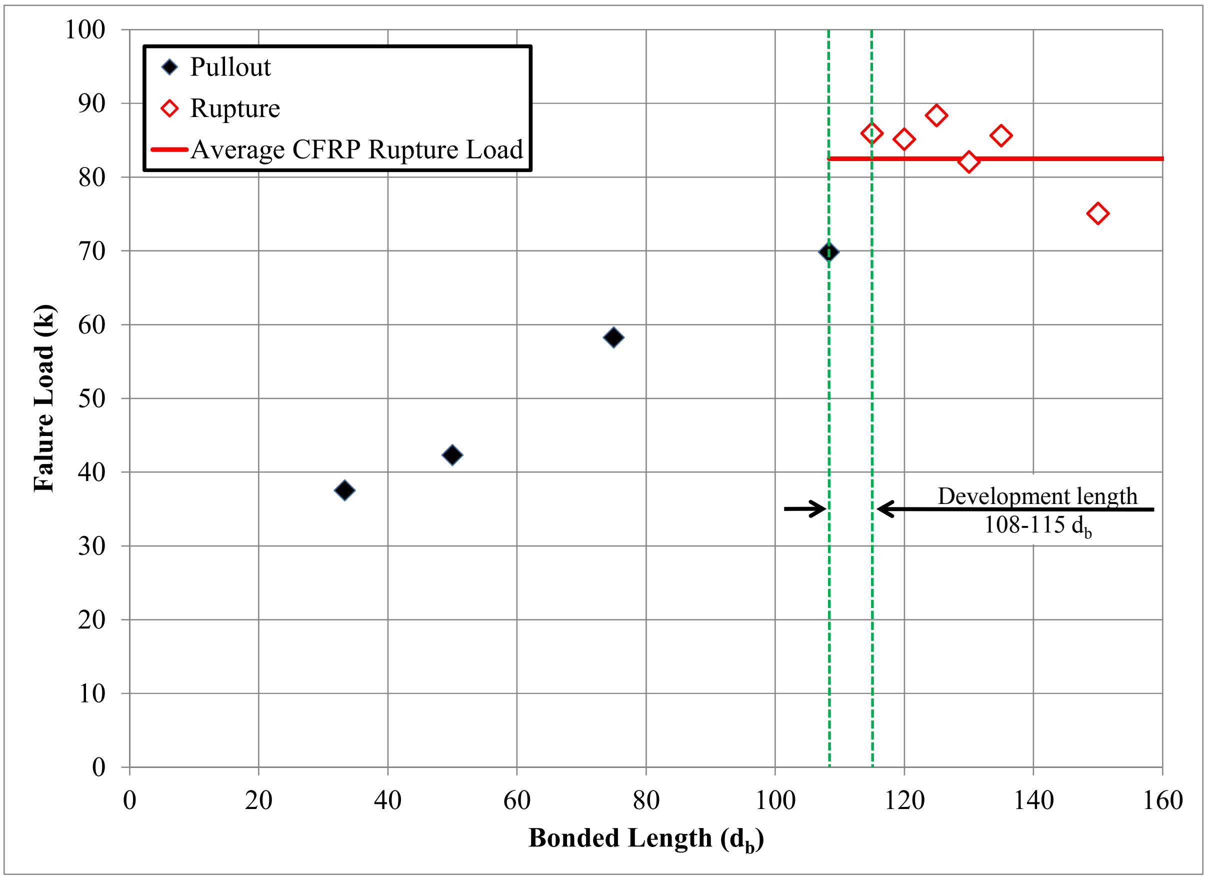


**Figure 3.31: Phase 2 CFRP bond strength results**

Beam-end test results from phase 2 tests on steel strands are illustrated in Figure 3.32. The red line represents the expected failure load for the 0.6 in. diameter steel prestressing strand. Each of the strands ruptured. The average failure load was 60.7 kips. Due to the lack of a pullout failure, the results for the development length of the steel strands were inconclusive, but appear to be less than 110 times the strand diameter which is less than the ACI 318 predicted value.

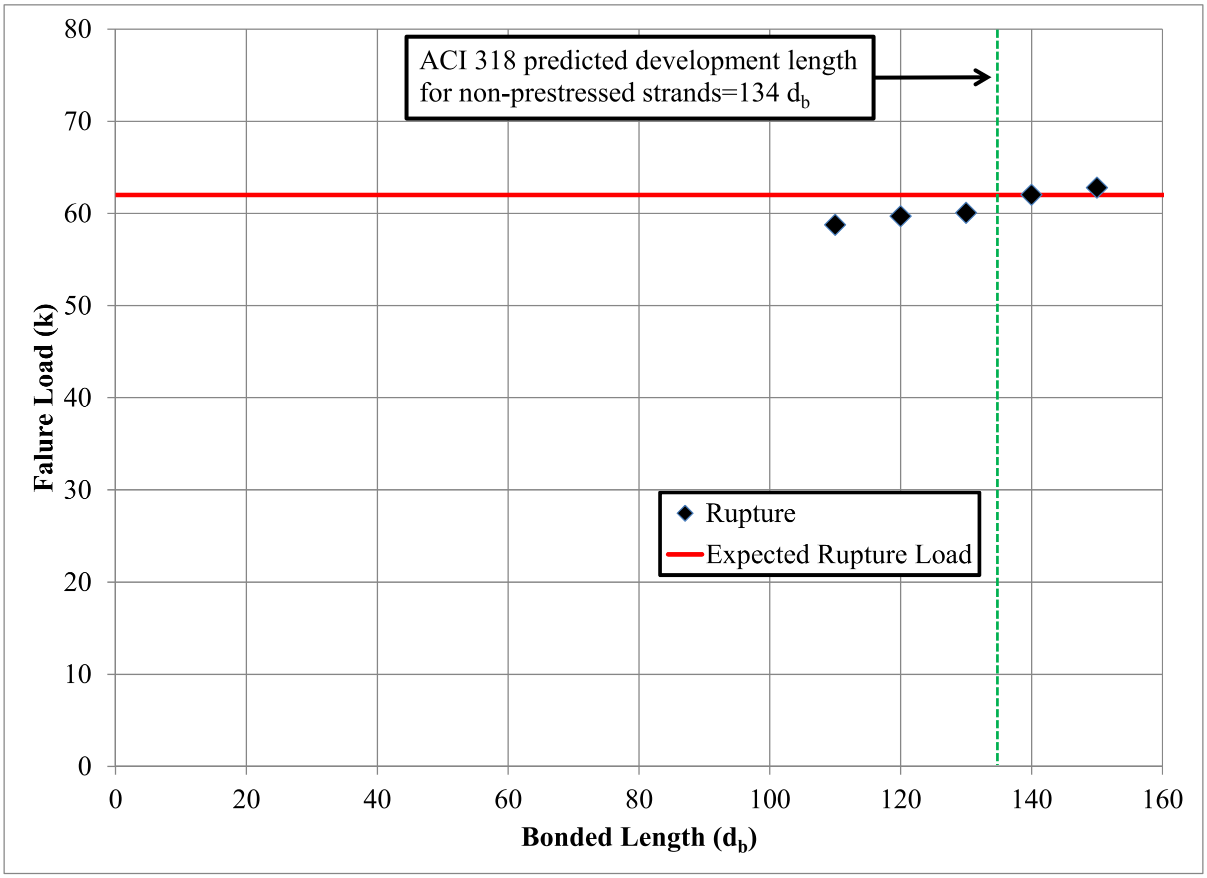


**Figure 3.32: Phase 2 steel bond strength results**

### 3.3.5 Discussion

Because tests were conducted on unstressed strands, the experimentally observed development lengths from this testing are only valid for strands used as non-prestressed reinforcement. Furthermore, the lengths found were the lengths necessary to develop the full rupture stress of the strands. For the steel strands, this is approximately 280 ksi, which is only slightly higher than the stress that steel strands can face under in-service loading. However, while the rupture stress of the CFRP strands is 461 ksi, the guaranteed stress value is 339 ksi. Structures prestressed with CFRP strands are designed using the guaranteed stress. Therefore, the strands do not need to develop their full rupture strength. Figure 3.33 shows the CFRP test results with the load corresponding to the guaranteed stress represented by the horizontal blue line.

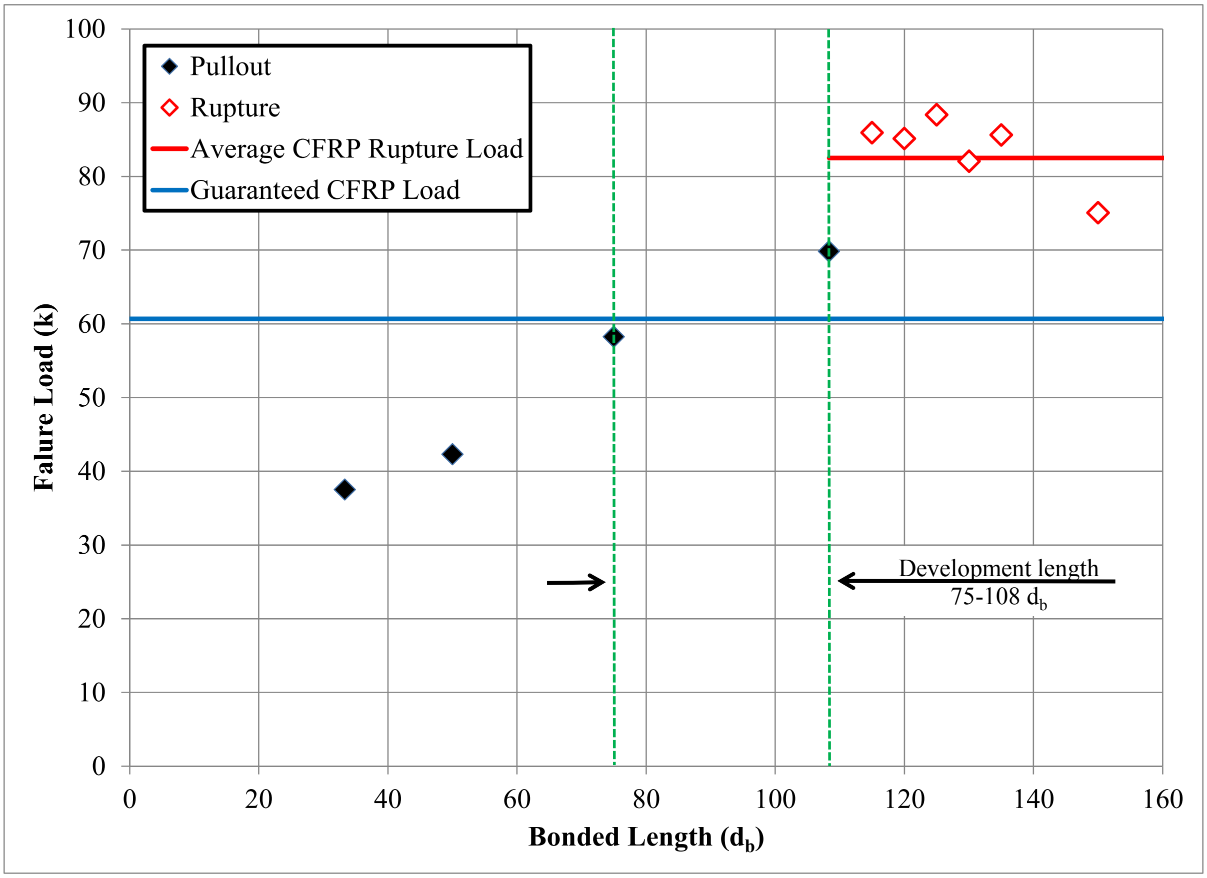


**Figure 3.33: Phase 2 CFRP bond strength results for guaranteed stress**

Based on these data, the expected length needed to develop the guaranteed stress for unstressed CFRP strands is between 75 and 108 $d_b$. This 33 $d_b$ range is large because of the wide breadth of $d_b$ values chosen for phase 1 specimens. Test results indicate that the length needed to develop the full rupture stress of non-prestressed steel strands is less than 110 $d_b$. This suggests that the ACI 318 (2011) value of 134 $d_b$ is conservative.

# CHAPTER 4: Flexural Behavior

This chapter describes the design, manufacture, testing, and analysis of cored slabs with all-FRP reinforcement and control slabs with steel reinforcement. The cored slabs contained CFRP prestressing strands and GFRP stirrups designed according to the recommendations given in ACI440.4R (2004) and ACI440.1R (2006), respectively. A steel-reinforced control slab and two identical FRP-reinforced slabs were cast at a precast concrete plant. The cored slabs were delivered to the Constructed Facilities Laboratory at North Carolina State University and were tested monotonically to failure using a four-point bending configuration. Load, midspan deflection, strand slip, and midspan curvature were measured during testing. The observed experimental behavior was compared to theoretical predictions. The behavior of the FRP reinforced section was compared to that of the standard steel reinforced section to determine if it is a suitable structural replacement.

## 4.1 Flexural Cored Slab Design

### 4.1.1 Steel Reinforced Cored Slab Design

To enable evaluation of the experimental FRP reinforced cored slabs, a steel control specimen was designed according to the NCDOT standard design plans for steel prestressed cored slabs (NCDOT 2015). A 45 ft. long, 36 in. wide, and 21 in. deep section was chosen for this experimental program. The NCDOT standard longitudinal reinforcement scheme and stirrup placement for a cored slab with these dimensions is shown in Figure 4.1. The section has two 12 in. diameter voids at mid-depth, spaced at 16 in. on center horizontally. Shear keys on both sides of the specimen are filled with grout during bridge construction, allowing the cored slab units to transfer force to adjacent slabs. The longitudinal reinforcement in the control slab included thirteen 0.6 in. diameter 270 ksi low-relaxation ASTM A416 steel strands. Eleven of the strands, at a depth of 19 in. in the section, provided the primary flexural capacity. Two strands in the top corners at a depth of 2.5 in. provided cracking resistance at release and during handling, and allowed the transverse steel to be tied more easily. Each steel strand was prestressed to 43,950 lbs., equivalent to 75% of its rupture strength. Two No. 4 60 ksi ASTM A615 longitudinal bars, also at a depth of 2.5 in., provided additional cracking resistance to the top of the section.

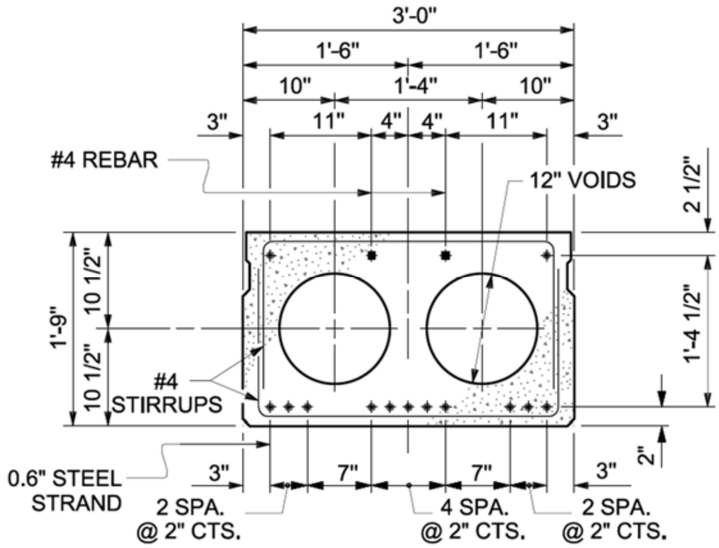


**Figure 4.1: Steel reinforced cored slab cross section**

A 3 ft. long solid zone at each end of the cored slab is used to increase shear capacity at the end zones. Solid zones were used in steel and FRP slabs. Shear reinforcement in the steel slab consisted of two overlapping U-shaped No. 4 60 ksi ASTM A615 steel stirrups. The first stirrup is placed 12 in. from each end of the specimen. Spacing for the next 54 in. was 9 in. on center and the midspan region spacing was 12 in. on center. This stirrup spacing is depicted in Figure 4.2. Two pairs of No. 5 stirrups, each enveloping one of the cores, were placed with 1 in. clear cover from each end of the cored slab to provide strand confinement. This detail is illustrated in Figure 4.3.

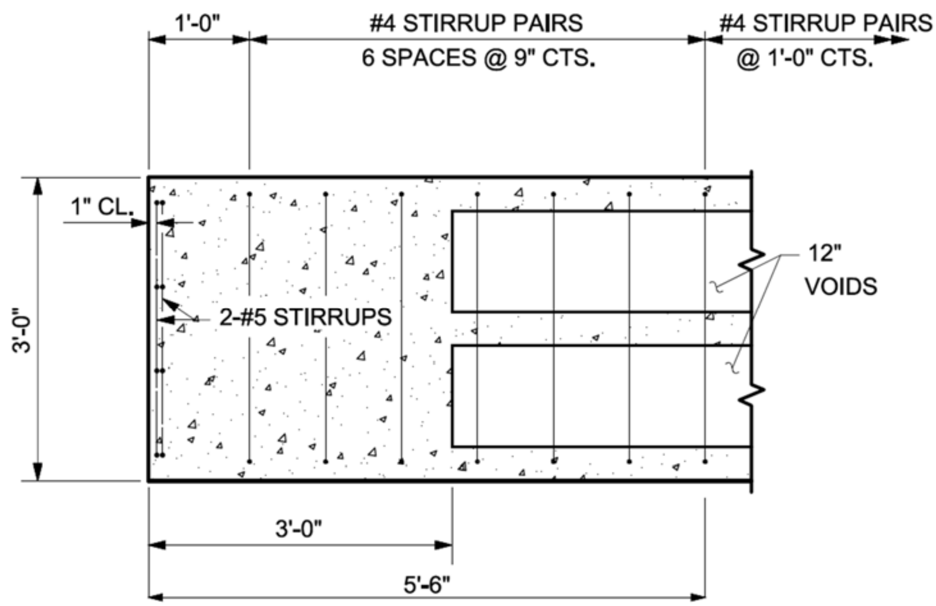


**Figure 4.2: Steel reinforced slab shear detail (plan view)**

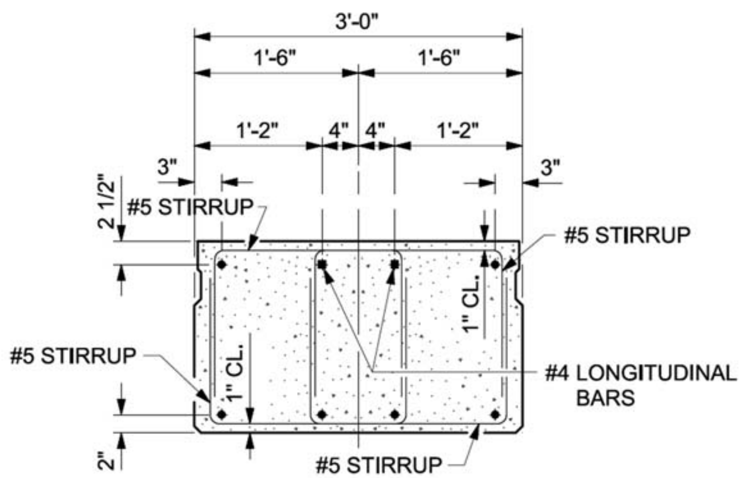


**Figure 4.3: Steel reinforced cored slab end shear reinforcement detail**

The NCDOT standard design includes 8 in. solid zones at both third-points of the span which traditionally allow for transverse post tensioning ducts. The standard specification also includes vertical dowel holes in the end solid zones to attach the cored slabs to the bridge bents. Solid zones were included in the test beams, but ducts and dowel holes were not. The cored slabs were all designed with 6500 psi concrete target strength using Type III high early strength cement in order to reach release strength quickly.

### 4.1.2 FRP Reinforced Cored Slab Preliminary Design

The CFRP prestressed cored slabs were designed to be a direct replacement for their existing steel prestressed counterparts so that they could be cast at precast plants that have existing forms and bulkheads in place for standard NCDOT cored slab sizes. Therefore, the design was kept as similar as possible to the current standard NCDOT geometric details. Key parameters controlled by the standard design details included the geometry of the concrete section and the location of the prestressing strands.

The final CFRP prestressed section is shown in Figure 4.4 where it can be seen that the 13 steel strands were replaced by 15 CFRP strands of the same size. The CFRP strands were prestressed to 39,450 lb due to the ACI 440.4R (2004) jacking force limit of 65% of the guaranteed strength of the strand. Therefore, two additional CFRP strands were required to have a similar total prestress force so that a similar design flexural capacity could be achieved. These two strands were placed in a second layer in the section where strands are placed for longer spans. Therefore, the existing bulkheads at the casting facility included holes for these strands. The two longitudinal No. 4 mild steel bars were replaced with No. 5 GFRP bars in the FRP design.

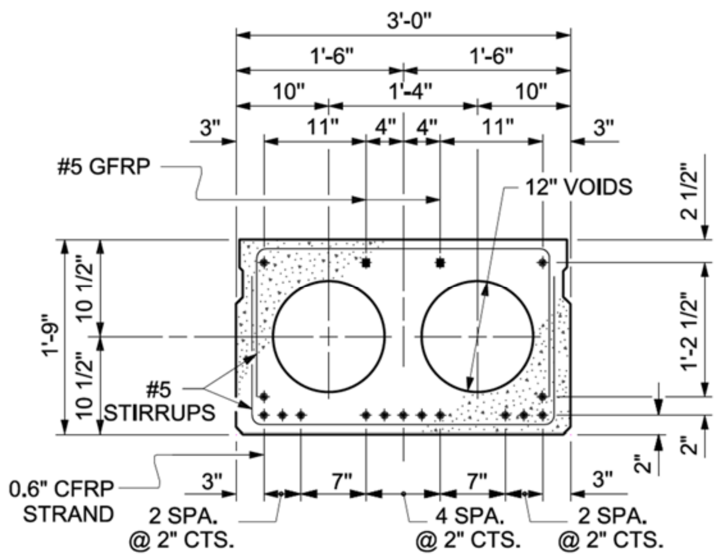


**Figure 4.4: FRP reinforced cored slab cross section**

The No. 4 mild steel stirrups were also replaced with No. 5 GFRP stirrups. ACI 440.1R (2006) limits the available stress in GFRP stirrups to the lower of either the stress corresponding to a strain of 0.4%, or the maximum stress that can be achieved in a bent GFRP stirrup. The strain limit, imposed to limit crack width, was the limiting factor. This caused an increase in the size of the stirrups, and a reduction in stirrup spacing to maintain equivalent shear capacity. The final design included No. 5 GFRP stirrups spaced at 7 in. throughout the length of the cored slab, as depicted in Figure 4.5. The end stirrup arrangement is the same for the FRP slabs as it is for the steel slabs, except that No. 6 GFRP stirrups were used.

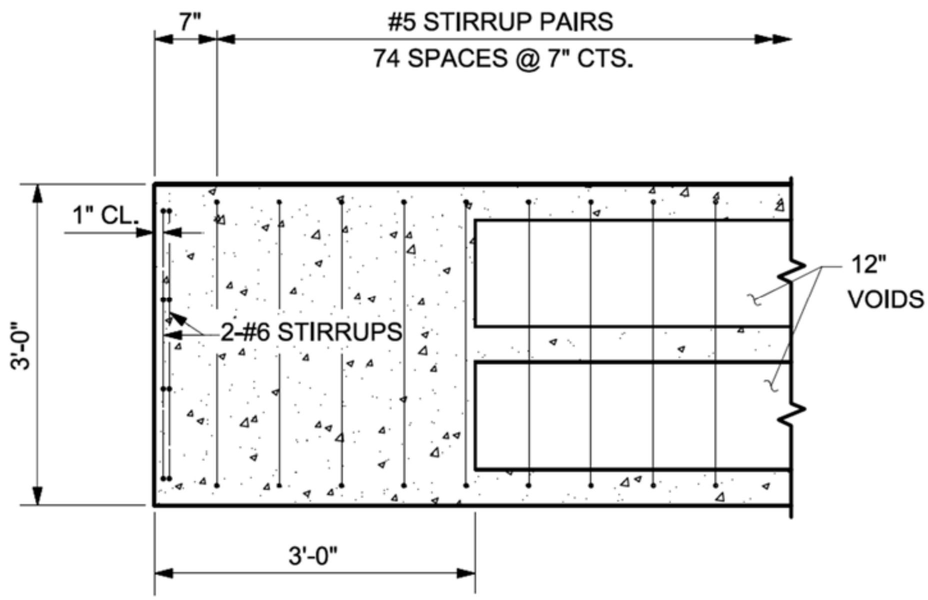


**Figure 4.5: FRP reinforced slab shear detail (plan view)**

### 4.2 Flexural Cored Slab Analysis and Predictions

A strain compatibility analysis in accordance with ACI 318 (2011) was performed to ascertain the flexural strength of the steel reinforced cored slabs. The predicted failure mode was crushing of the concrete in the compression zone after yielding of the strands. The predicted strength values from these calculations in terms of moment and total load in the experimental test setup are summarized in Table 4.1.

The flexural capacity of the FRP reinforced cored slabs was evaluated in accordance with ACI 440.4R (2004). While the mean rupture stress of the CFRP strands was 461 ksi, the guaranteed stress was 339 ksi. Therefore, while the experimental failure mode was predicted to be crushing of the concrete in the compression zone, strand rupture governed for the ACI prediction. An equivalent stress block was used to approximate the stress in the concrete at the theoretical rupture of the CFRP strands prior to crushing. Detailed calculations can be found in Appendix A. The results of these calculations in terms of moment and total test load are shown in Table 4.1.

**Table 4.1: ACI flexural strength predictions**

| | | Moment Capacity (k-ft) | Test Load (k) |
|---|---|---|---|
| Steel $\Phi$=0.9 | Unfactored | 950 | 110 |
| | Factored | 855 | 97 |
| FRP $\Phi$=0.85 | Unfactored | 1120 | 133 |
| | Factored | 952 | 111 |

After the initial design was completed and the ACI capacities were calculated, the slabs underwent a more detailed investigation to predict their expected performance. The flexural capacity and behavior for all the cored slabs were predicted using a layered sectional analysis approach.

The cross section was discretized into horizontal layers, as illustrated in Figure 4.6. The top strain, $\varepsilon_{c\ max}$, was varied from 0.1% to -0.3% in 0.005% increments. Tensile (positive) top strains were used to account for camber. For each top strain, the strain at the middle of each layer was calculated based on an assumed neutral axis depth and a linear strain distribution.

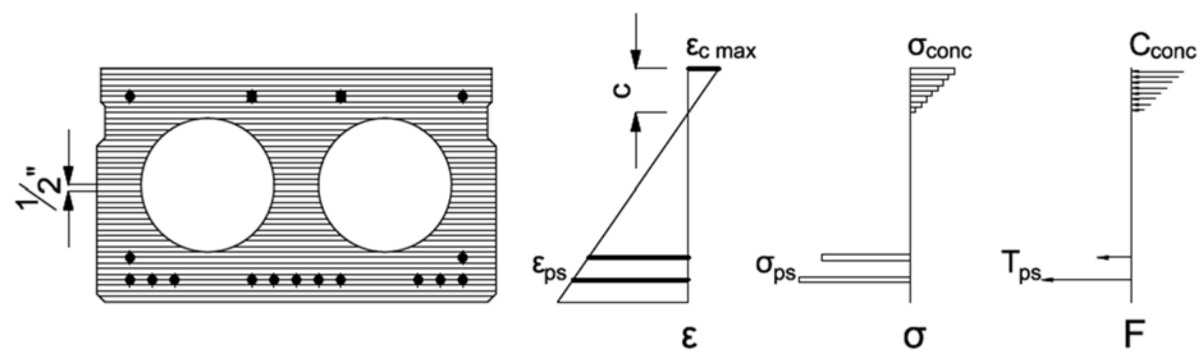


**Figure 4.6: Layered sectional analysis schematic**

Because the specified concrete strength was 6500 psi, the initial analysis used the Hognestad (1951) parabolic model to relate concrete compression strain and stress:

$$\sigma_c = f_c' \left[ 2\frac{\varepsilon_c}{\varepsilon_{co}} - \left(\frac{\varepsilon_c}{\varepsilon_{co}}\right)^2 \right] \tag{4.1}$$

where $\sigma_c$ is the concrete stress, $\varepsilon_c$ is the concrete strain, and $\varepsilon_{co}$ is the strain corresponding to $f'_c$. However, the measured 28-day concrete strength exceeded 9000 psi. To characterize the stress-strain relationship of this high-strength concrete in the cored slabs, the Popovics (1973) constitutive model was used to represent the concrete in compression because it gives a more accurate representation of the response of high-strength concrete:

$$\sigma_c = f_c' \left( \frac{n\left(\frac{\varepsilon_c}{\varepsilon_{co}}\right)}{(n-1) + \left(\frac{\varepsilon_c}{\varepsilon_{co}}\right)^n} \right) \tag{4.2}$$

where

$$n = 0.4\, x\, 10^{-3} f_c' + 1.0 \tag{4.3}$$

This model was used to find the stress in each layer of concrete based on its strain. The tensile strength of uncracked concrete was ignored. The stress was multiplied by the area of each layer to calculate the resultant compressive force exerted on that layer, as shown in Figure 4.6.

The strain in the prestressing strands was calculated by adding the effective prestressing strain to the concrete strain value obtained from the linear strain distribution at the level of the prestressing strand. The strain in the rebar was assumed to be equal to the strain in the concrete at the same depth as the rebar. A modified Ramberg-Osgood model (Collins and Mitchell 1991) was used to represent the steel tensile prestressing strand behavior:

$$\sigma_{ps} = E_{ps}\varepsilon_{ps} \left[ A + \frac{1-A}{\left[1 + \left(B\varepsilon_{ps}\right)^C\right]^{1/C}} \right] \tag{4.4}$$

where $\sigma_{ps}$ is the stress, $E_{ps}$ is the Young's modulus, and $\varepsilon_{ps}$ is the strain in the prestressing strands, while $A$, $B$, and $C$ were calibrated to 0.01, 107.5, and 13, respectively, using the mill certification for the steel prestressing strands used. A bilinear stress-strain model with a yield stress of 60 ksi was used for the rebar. A simple linear-elastic relationship was used to model the tensile behavior of the CFRP strands. Following the recommendations in ACI 440.1R (2006), the strength contribution from the GFRP bars in compression was ignored. The stress obtained from the applicable model was multiplied by the area of the reinforcement at a given section depth to find the resultant tensile force generated by the reinforcement at that depth.

The (negative) compressive forces from all layers of concrete and rebar in compression and the (positive) tensile forces from the prestressing strands were summed. Then, the value for neutral axis depth was varied until the sum of the forces in the section was equal to zero. When this equilibrium condition was reached, the moments generated by each force were summed about the top of the section to find the moment capacity. The corresponding curvature was calculated by dividing $\varepsilon_{c\ max}$ by the neutral axis depth.

In this manner, the moment and curvature for the full range of $\varepsilon_{c\ max}$ values was determined. This data was used to generate the full predicted moment-curvature response for the steel and FRP prestressed sections, shown in Figure 4.7. The graph starts with negative curvature due to the presence of camber. The failure moment was predicted to be 966 kip-ft. for the steel reinforced specimen and 1283 kip-ft. for FRP the reinforced specimen, 33% higher than the steel reinforced specimen. The plateau portion of the prediction curve for the steel cored slab represents yielding of the prestressing strands. Because the strands yield before the concrete crushes, a tension failure mode was predicted. Although curvature comparable to that of the steel slab was predicted for the FRP reinforced slabs, a tension failure is not possible because CFRP strands do not yield. A compression failure was predicted due to crushing of the concrete in the compression zone before strand rupture.

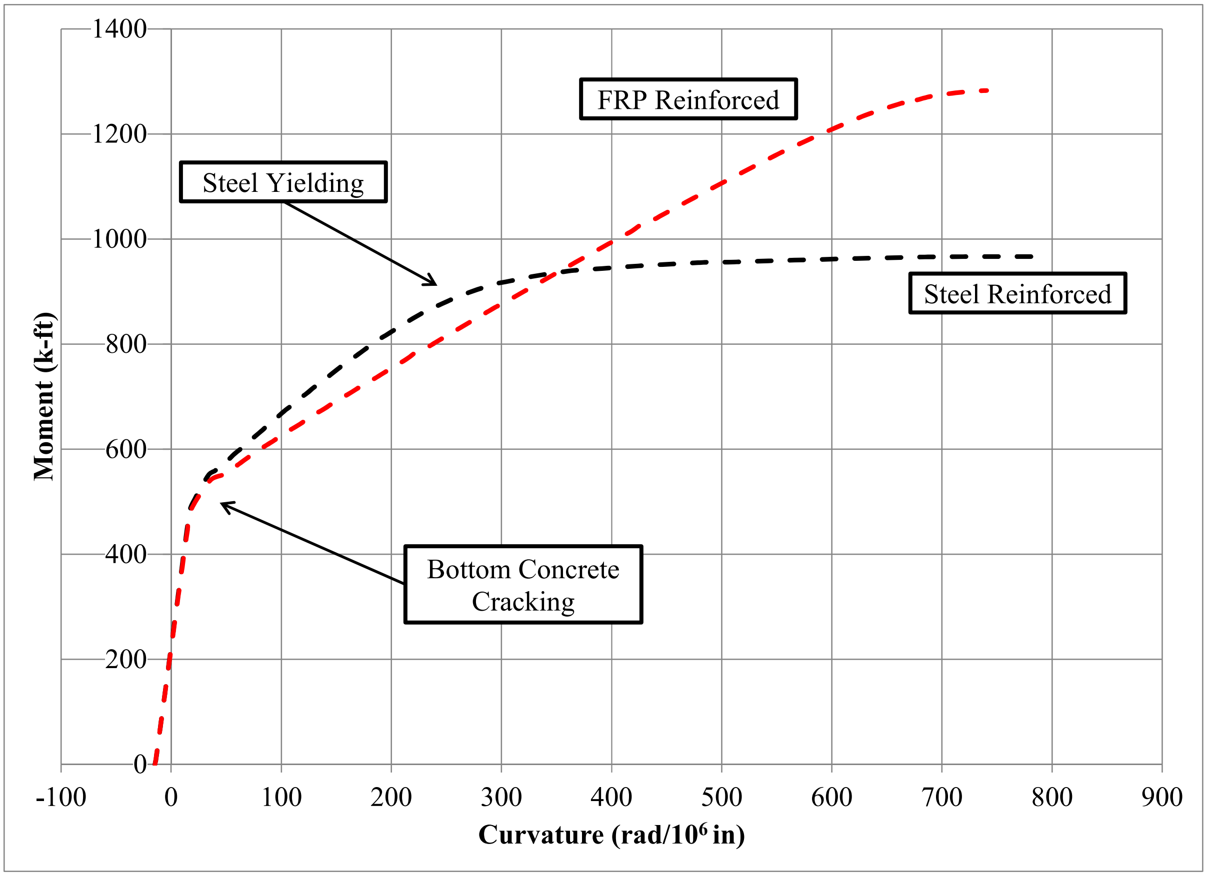


**Figure 4.7: Moment-curvature response predictions**

The load-deflection behavior of the cored slabs was also predicted using the results of the layered sectional analysis. The slab was discretized along its length into 6 in. sections, as depicted in Figure 4.8. The maximum (midspan) total moment was varied from zero to the failure moment in 5 kip-ft. increments. At each increment, the moment at the middle of each 6 in. segment was calculated. Then, the curvature corresponding to that moment was taken from the moment-curvature response and assumed constant over that increment. The curvature distribution from support to midspan of the cored slabs was integrated over each segment to calculate the midspan deflection. For the steel section, the deflection calculation was problematic because of the flat segment of moment-curvature response leading up to failure. The cored slab can continue to deflect with very little increase in load, making the deflection at failure difficult to predict. Deflection calculations are further complicated by cracked segments of the cored slabs, where curvature is concentrated, because the analysis assumes a smooth curvature distribution.

This deflection calculation was made for each increment of maximum moment. The load at each moment increment was calculated based on a simply-supported, four-point bending test configuration. The predicted load-deflection curves for the steel and FRP cored slabs generated by this analysis are plotted with the ACI strength predictions in Figure 4.9. The steel reinforced specimen was expected to fail at a load of 113 kips, with 17.0 in. of deflection. Failure of the FRP reinforced specimen was predicted to occur at a load of 151 kips, with 17.9 in. of deflection.

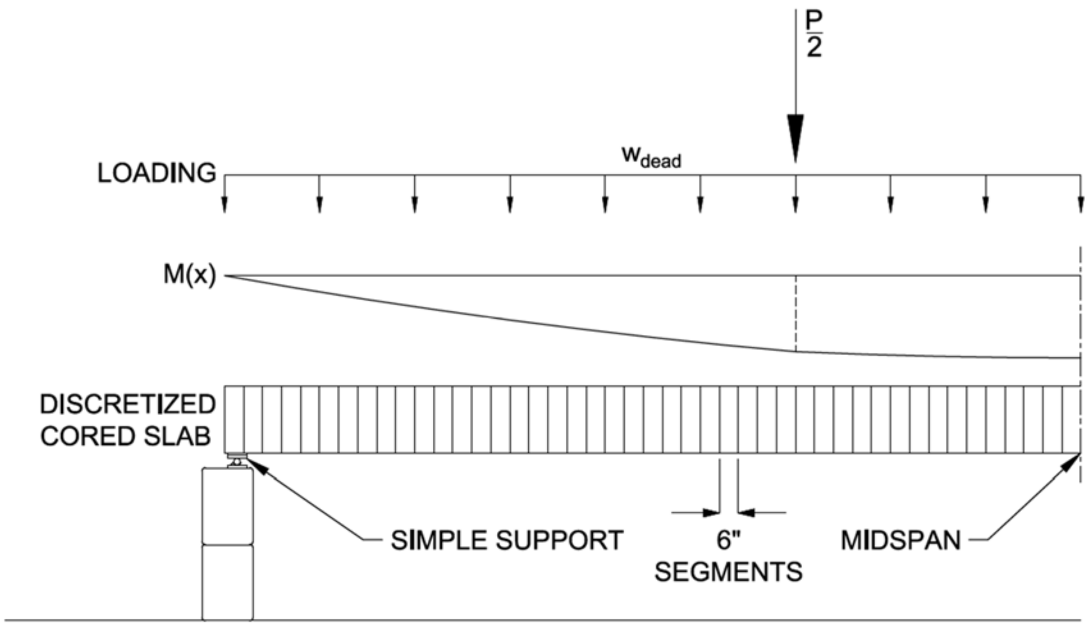


**Figure 4.8: Deflection calculation schematic**

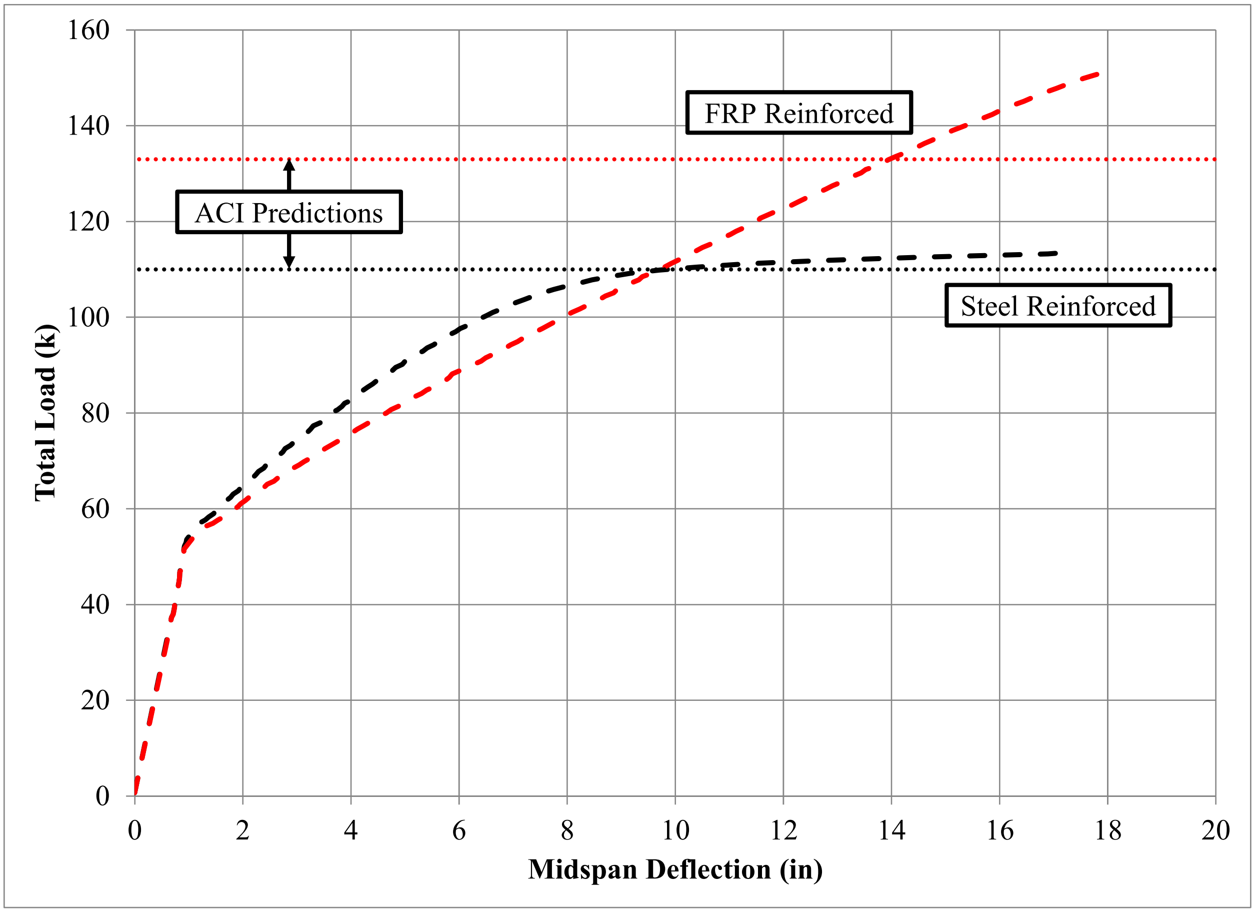


**Figure 4.9: Load-deflection behavior prediction**

### 4.3 Flexural Cored Slab Fabrication

Test specimens were cast at a precast plant that regularly produces cored slabs. While the standard procedure for casting cored slabs was used for the steel reinforced specimens, a special procedure was required to cast the FRP reinforced specimens.

#### 4.3.1 Steel Reinforced Cored Slab Fabrication

The first step in the construction of the steel-reinforced slabs was running the steel strands down the length of the casting bed through the bulkheads and end plates, placing chucks on the ends of the strands against the bulkheads, and stressing the strands. Next, the cardboard void tubes were placed into the forms to create the hollow cores, and the stirrups were tied to the strands with steel rebar ties. Concrete was then poured into the forms. Several 4 in. x 8 in. test cylinders were cast simultaneously with the cored slabs. After 14 hours, the concrete had reached its release strength of 4500 psi, the strands were detensioned with a torch cutter, as shown in Figure 4.10, and the cored slabs were removed from the forms.

**Figure 4.10: Detensioning with torch cutter**

### 4.3.2 FRP Reinforced Cored Slab Fabrication

In order to avoid local crushing failure of the CFRP prestressing strands, due to transverse stresses at end anchorages, standard steel prestressing chucks cannot be used. Hence, special anchorages specific to the CFRP prestressing strands must be used, as provided by the manufacturer. The CFRP strands were run through the end plates of the cored slabs, but not the bulkheads. They were cut shorter than the casting bed and the ends were attached via couplers to short segments of steel strand that ran from the couplers through the bulkheads at either end of the casting bed, as shown in Figure 4.11.

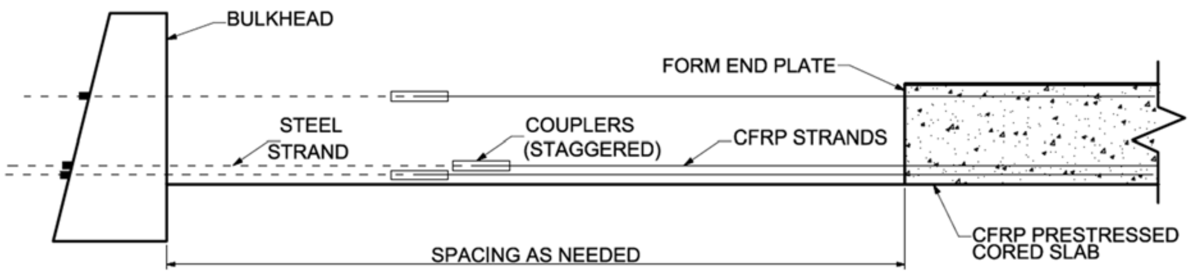


**Figure 4.11: CFRP prestressing schematic (elevation view)**

The couplers are a proprietary anchorage system developed by the CFRP strand manufacturer to connect the CFRP strands to steel strands. A schematic of the coupler system is depicted in Figure 4.12.

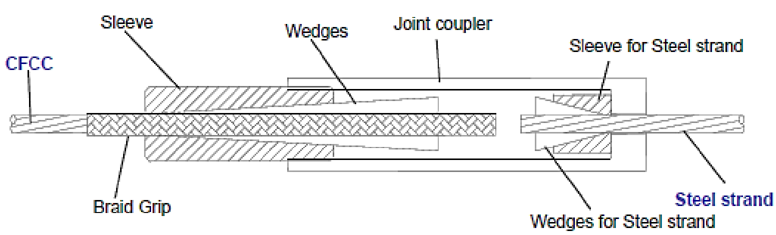


**Figure 4.12: Coupler schematic**

The installation of the anchorage and coupler system for the CFRP prestressing strands is summarized in Figure 4.13. Coupler installation began by affixing two layers of buffer material to the ends of the CFRP strands. This buffer material protected the strand by dissipating the transverse force applied to the strand by the couplers. The first layer was a helical mesh wrap. One end of it was attached to the end of the strand with electrical tape. Then, the rest of the wrap was tightly would around the strand, and taped at its other end, as shown in Figure 4.13(a). The second layer, a metal jacket, was placed over the first mesh layer. One end of it was taped to the strand with electrical tape, and then the rest of the jacket was tightly squeezed around the CFCC. Then, the other end of the jacket was taped around the strand, as shown in Figure 4.13(b).

After the buffer material was attached, the CFRP strands were inserted into the couplers. The CFRP chuck was similar to a standard wedged steel chuck, except that the wedges were significantly longer, and they were arranged around the buffer material instead of directly onto the strand. Both of these modifications allow for better distribution of clamping force onto the FRP strand. The wedges were placed into a rubber wedge guide, which was then slid into the chuck, as shown in Figure 4.13(c). To ensure a tight grip on the strand, the chuck was placed into a seating ram assembly. A hand pump was used to the push the wedges into the chuck, as shown in Figure 4.13(d).

A standard steel chuck was slid onto the steel strand segment, as shown in Figure 4.13(e). The other half of the coupler bore against the steel chuck, and was screwed onto the CFRP chuck, as shown in Figure 4.13(f). The diameter of the couplers exceeded the strand spacing. Therefore, the couplers had to be staggered to prevent them from touching, as shown in Figure 4.13(g).

(a) Helical mesh is wrapped around the end of the CFRP

(b) A metal jacket is taped over the mesh wrap

(c) Wedges are placed around the strand and fed into a chuck

(d) A hand pump presses the wedges into the chuck

(e) A standard steel chuck is placed onto the steel strand

(f) The two halves of the coupler are screwed together

(g) Couplers are staggered so they do not touch during tensioning

**Figure 4.13: Coupler installation**

After the couplers were attached, the ends of the steel strands were passed through the bulkheads and tensioning could take place in the same manner as that of standard steel strands. The GFRP stirrups were tied using plastic zip ties to eliminate all steel in the cored slabs except for the lifting hooks tied into both ends of the cored slabs, as depicted in Figure 4.14. The rest of the casting process was the same as the process for casting the steel prestressed cored slabs. Figure 4.15 illustrates the final arrangement of reinforcement and cores before casting. The casting process is shown in Figure 4.16.

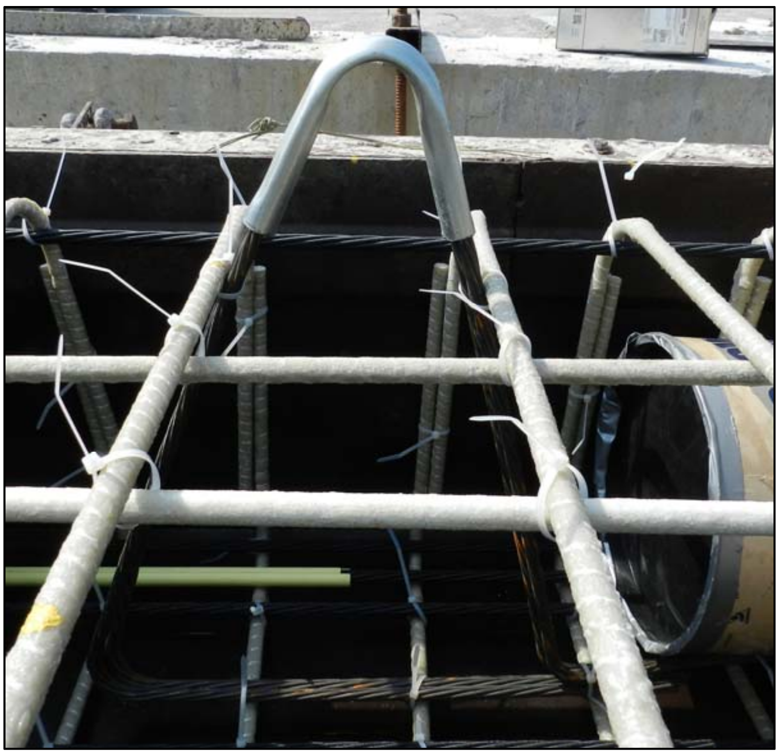

**Figure 4.14: Steel lifting hooks**

**Figure 4.15: Overall reinforcing layout for CFRP prestressed cored slabs**

**Figure 4.16: Cored slab casting**

### 4.4 Flexural Cored Slab Testing

The cored slabs were loaded monotonically to failure in four-point bending on a simple span. A 220 kip capacity hydraulic actuator hanging from a reaction frame was placed at the midspan of the beam. The reaction frame was post-tensioned to the laboratory strong floor. A 15 ft. long spreader beam was bolted to the bottom of the actuator. Pin and roller supports attached to plates on the bottom of the spreader beam transferred load at third points through 8 in. wide steel plates resting on the top of the cored slab specimen. A schematic of the test setup for the 45 ft. long cored slabs is depicted in Figure 4.17.

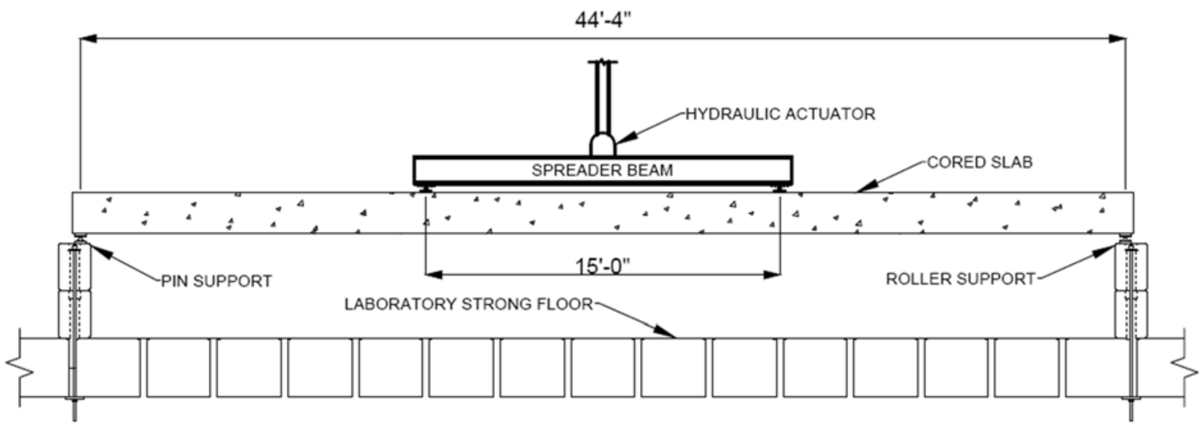


**Figure 4.17: Test setup schematic**

String potentiometers were used to measure deflection at the load points and at midspan. Pi gages at midspan on the top and bottom of each cored slab measured average concrete strain. This instrumentation is illustrated in Figure 4.18. Linear potentiometers were also used to measure strand slip at one end of each cored slab.

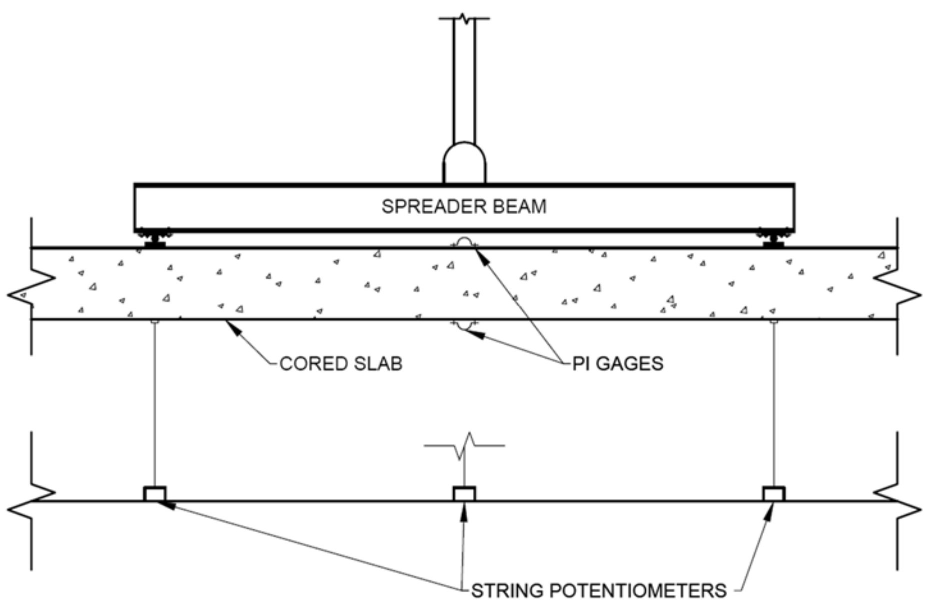


**Figure 4.18: Flexural test instrumentation**

Each flexural specimen was designated with the first two letters "FL". The steel prestressed control cored slab was named FL-ST, and the CFRP prestressed cored slabs were named FL-CF-1 and FL-CF-2.

All specimens were loaded at a rate of 0.15 in/min up to the cracking load. Post-cracking, the load rate was increased to 0.5 in/min until failure. Figure 4.19 illustrates an overall view of the test setup prior to testing. Figure 4.20 shows FL-CF-2 during testing, deflecting 8 in. at midspan. The blue line represents the location of the bottom of the beam when it was flat.

**Figure 4.19: FL-CF-1 before testing**

**Figure 4.20: FL-CF-2 during testing**

## 4.5 Flexural Cored Slab Test Results

In each test, slabs failed near one of the load points, due to the stress concentration caused by interaction of the maximum moment and maximum shear. Figure 4.21, Figure 4.22, and Figure 4.23 depict the areas where failure occurred for FL-ST, FL-CF-1, and FL-CF-2, respectively. Each of these failures occurred on a diagonal plane from the loading plate towards the end of the slab. This failure plane suggests that the effects of shear stresses in the section were a contributor to the failure of the cored slabs.


**Figure 4.21: FL-ST after testing**


**Figure 4.22: FL-CF-1 after testing**


**Figure 4.23: FL-CF-2 after testing**

A comparison of the flexural performance of FL-ST, FL-CF-1, and FL-CF-2 is summarized in Figure 4.24. The behavior of all three slabs was the same until cracking. The cracking load was approximately 55 kips, which is equivalent to a total moment of 540 kip-ft. All cored slabs demonstrated significant cracking throughout the maximum moment region. After cracking, the load increased for the steel specimen until the steel yielded. This initial portion of the post-cracking curve had a higher slope for the steel section than for the FRP section due to the higher stiffness of the steel. The steel continued to yield until the concrete crushed, resulting in a tension failure. The FRP cored slabs exhibited bi-linear behavior. After cracking, the load increased linearly with increasing deflection, until the concrete crushed. Because the CFRP strands cannot yield and did not rupture, this was a compression failure. However, due to extensive concrete cracking and substantial strain in the CFRP strands at the time of failure, the section had significant deformation capacity.

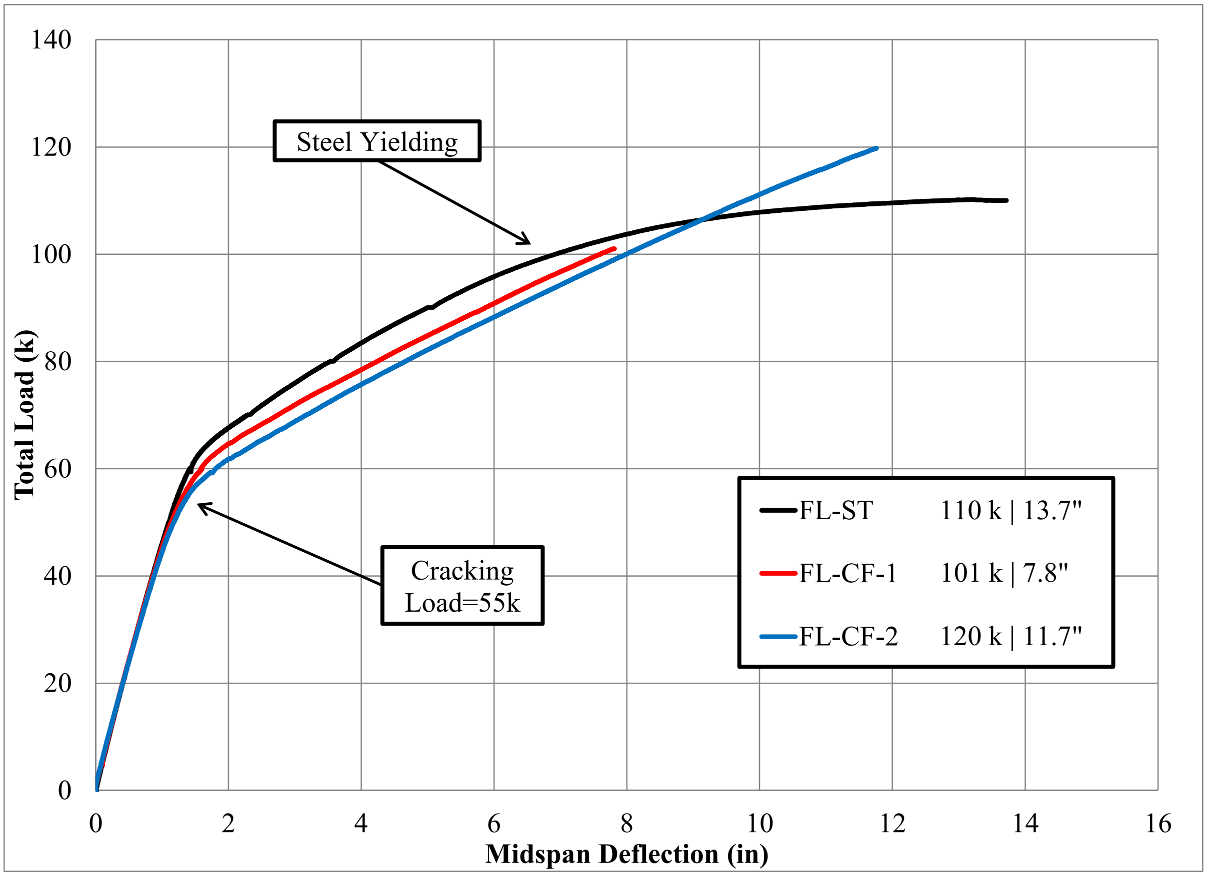


**Figure 4.24: Flexural test results**

The strain data from the top surface pi gages at the midspan of each specimen are shown in Figure 4.25. All strain gages remained attached to the compression face of the specimen until failure. Both FL-ST and FL-CF-2 reached peak compression strains at failure acceptably near 0.3%, which supports a flexural failure accompanied by concrete crushing at the ultimate load. FL-CF-1 failed from concrete crushing at a strain of 0.184%, considerably lower than 0.3%. Because the CFRP strands were still intact after this failure, it was hypothesized that another mechanism caused this premature failure. This will be discussed further in Section 4.6.2

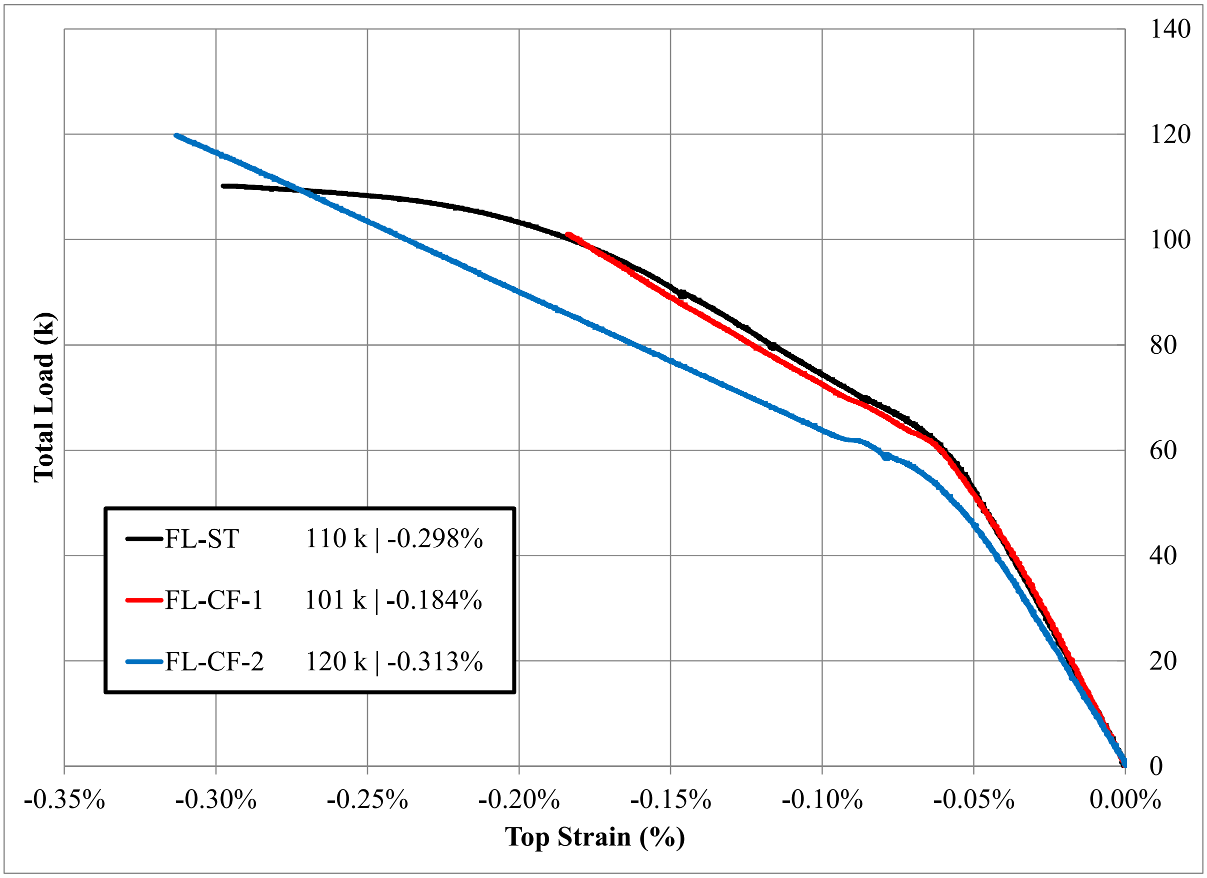


**Figure 4.25: Strain data from flexural tests**

Cylinders produced at the production facility with the beams were not available for testing at the time of the cored slabs were tested in the laboratory (cylinders were damaged or lost at the precast facility). Therefore, cores were extracted from each cored slab after testing. Cylinders were broken by the precaster at 28 day strength, and those reported values are compared to the cores taken at the laboratory in Table 4.2. Because the entire CF series was cast at the same time on the same casting bed, there is one set of cylinders for all slabs. Due to the high variability of test cylinders for FL-ST and cores for the CF series, all cored slab concrete was assumed to have a compressive strength of 9500 psi.

**Table 4.2: Concrete compressive strength of 28 day cylinders and cores**

| | Concrete Compressive Strength (psi) | | |
|---|---|---|---|
| | FL-ST | FL-CF-1 | FL-CF-2 |
| Test Cylinders 28 days | 7552 | 9225 | |
| | 8256 | 9593 | |
| | 9022 | 9391 | |
| Average | 8277 | 9403 | |
| Standard Deviation | 735 | 184 | |
| Cored Specimens FL-ST: 131 days FL-CF:188 days | 9485 | 9334 | 8596 |
| | 10164 | 9170 | 8141 |
| | 9157 | 9426 | 8732 |
| | 9784 | 7268 | 6792 |
| | - | 6246 | 7286 |
| | - | 8494 | - |
| Average | 9648 | 8323 | 7909 |
| Standard Deviation | 429 | 1297 | 843 |

### 4.6 Flexural Cored Slab Discussion

This section compares the performance of the flexural cored slabs tested to each other and to the predictions discussed in Section 4.2.

#### 4.6.1 FL-ST

The tension controlled failure of the control slab was the expected behavior of the specimen. A comparison of the test results with the prediction from the layered sectional analysis is illustrated in Figure 4.26. The measured experimental capacity of the cored slab was 110 kips, equal to the ACI 318 (2011) capacity, and 2.7% lower than the predicted capacity of 113 kips.

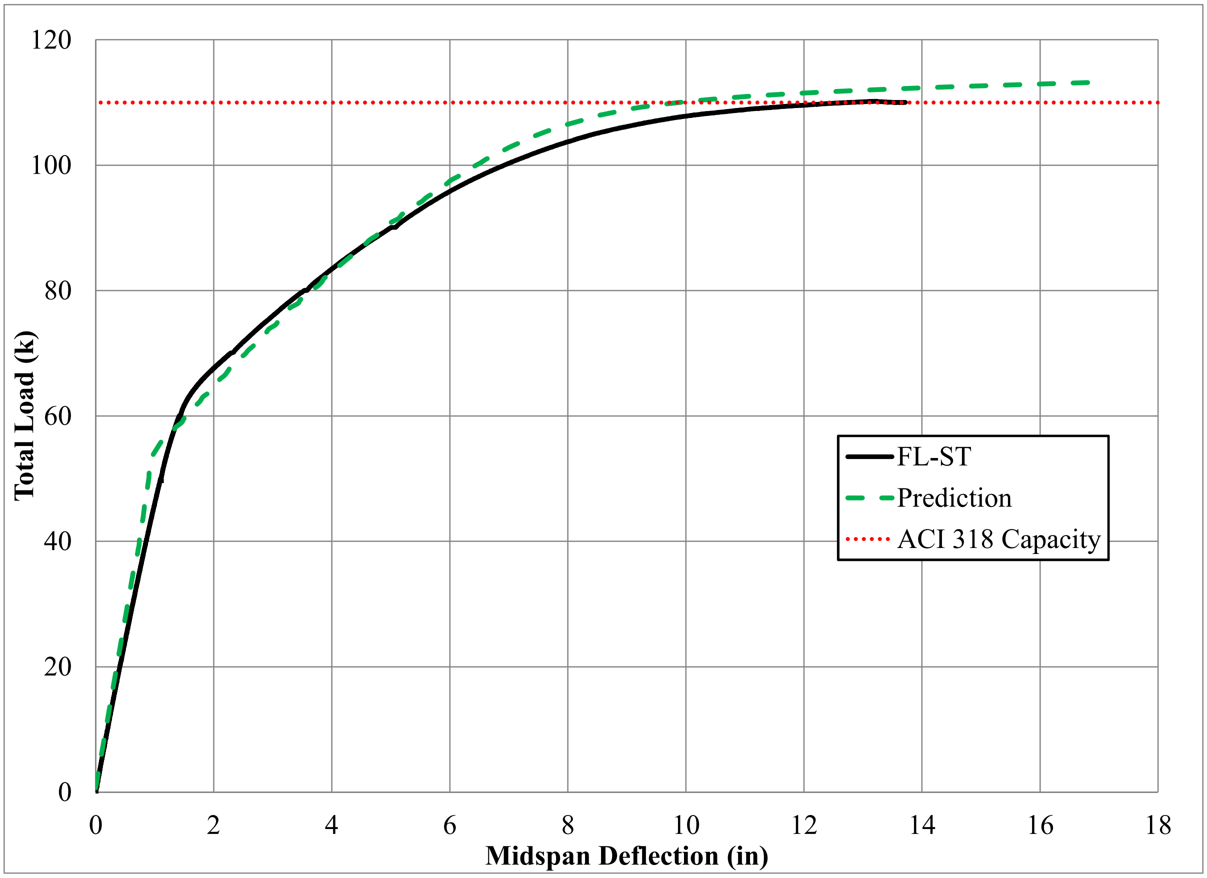


**Figure 4.26: Prediction and behavior of FL-ST**

### 4.6.2 FL-CF-1

Figure 4.27 shows the test results from the first FRP reinforced specimen alongside the predicted behavior. The predicted capacity was 151 kips, and the actual capacity was 101 kips. While this 50% error is larger than a reasonable experimental error, the test curve closely follows the predicted curve. Because the CFRP strands did not rupture, this result suggests that a deficiency in the concrete caused this premature failure.

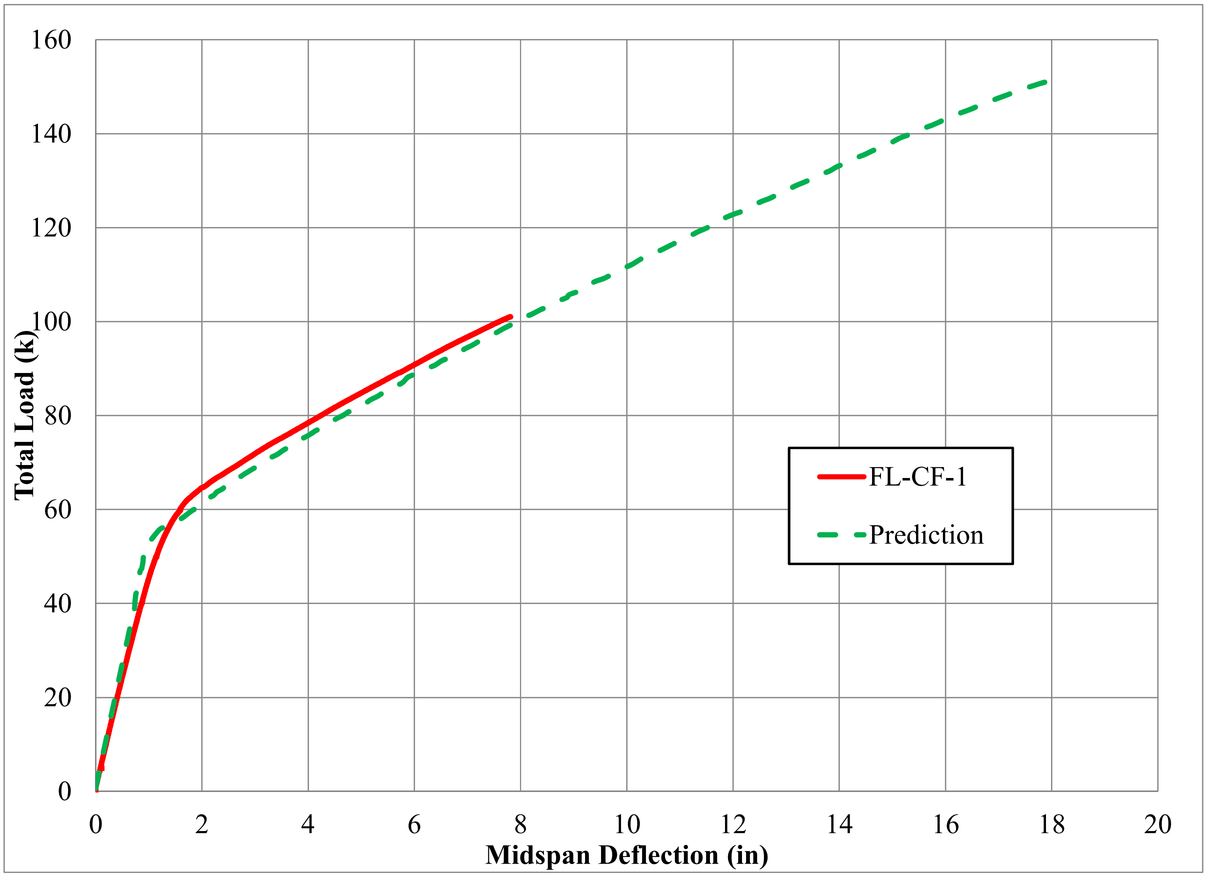


**Figure 4.27: Prediction and behavior of FL-CF-1**

Upon inspection of the tested specimen, it was apparent that it contained a manufacturing defect. One of the void tubes used to create the hollow cores had floated from its designated location at the mid-height of the section upward close to the surface of the cored slab. This is depicted in Figure 4.28 immediately after failure and in Figure 4.29 after the cored slab had been broken apart for disposal. Because the cross section of the cored slabs is short and wide, the compression zone is relatively shallow, about 4 in. deep. Therefore, when the void floated to the top of the cored slab, it created a large void in the compression zone, as illustrated in Figure 4.30. This defect was particularly problematic because it occurred at a third-point of the cored slab at the location of maximum moment and shear, as mentioned in Section 4.5.

**Figure 4.28: Elevation view of floated void tube in FL-CF-1**

**Figure 4.29: Cross section view of floated void tube in FL-CF-1**

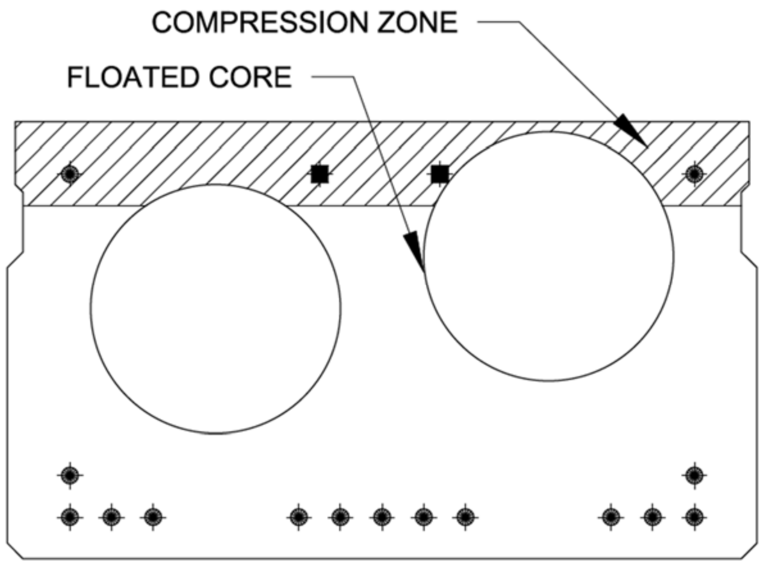


**Figure 4.30: Floating core schematic**

When the forms are being prepared for casting, void tubes are supported from the bottom by a loop of tie wire that is attached to the top of the form. After the concrete is poured, the voids are pushed upwards by the buoyant force of the surrounding concrete. To keep the tubes from floating, plastic cradles are suspended from above by bolts that are attached to a steel bar. The steel bar is then bolted to the sides of the form to keep it in place. This system is shown in Figure 4.31. The bolts holding the cradles are cast into the cored slabs. Before detensioning, the bolts are removed and the holes are filled with grout.

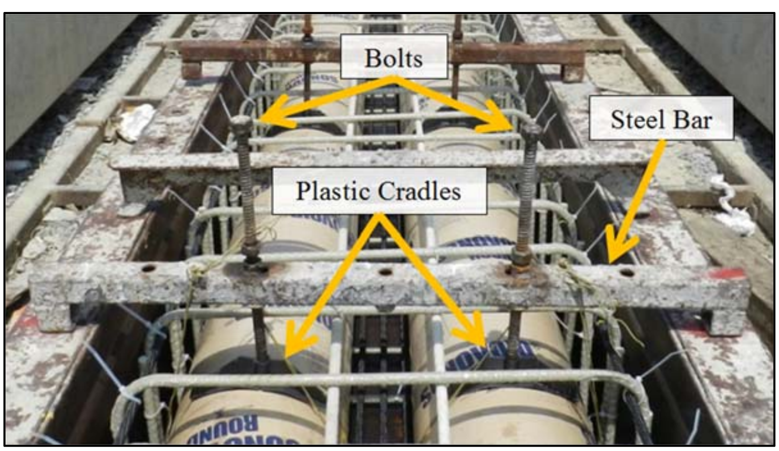


**Figure 4.31: Void hold-down supports**

It is clear from inspection of the failed FL-ST-1 specimen that some component of the system used to keep the void tubes from floating failed during casting. This floating hollow core reduced the size of the compression zone. This phenomenon was also observed by Storm et al. (2013).

### 4.6.3 FL-CF-2

The behavior of the second FRP reinforced cored slab is depicted alongside its predicted behavior in Figure 4.32. The unfactored and factored ACI 440.4R (2004) predicted capacities are also shown. It was noted that although the strength of FL-CF-2 was 10% lower than the unfactored ACI value, it was 8% higher than the factored ACI value.

In a similar fashion to FL-CF-1, the predicted response curve was followed closely, but FL-CF-2 failed at 120 kips. Again, since the CFRP strands did not rupture at failure, this 26% difference must be attributed to other components of the section.

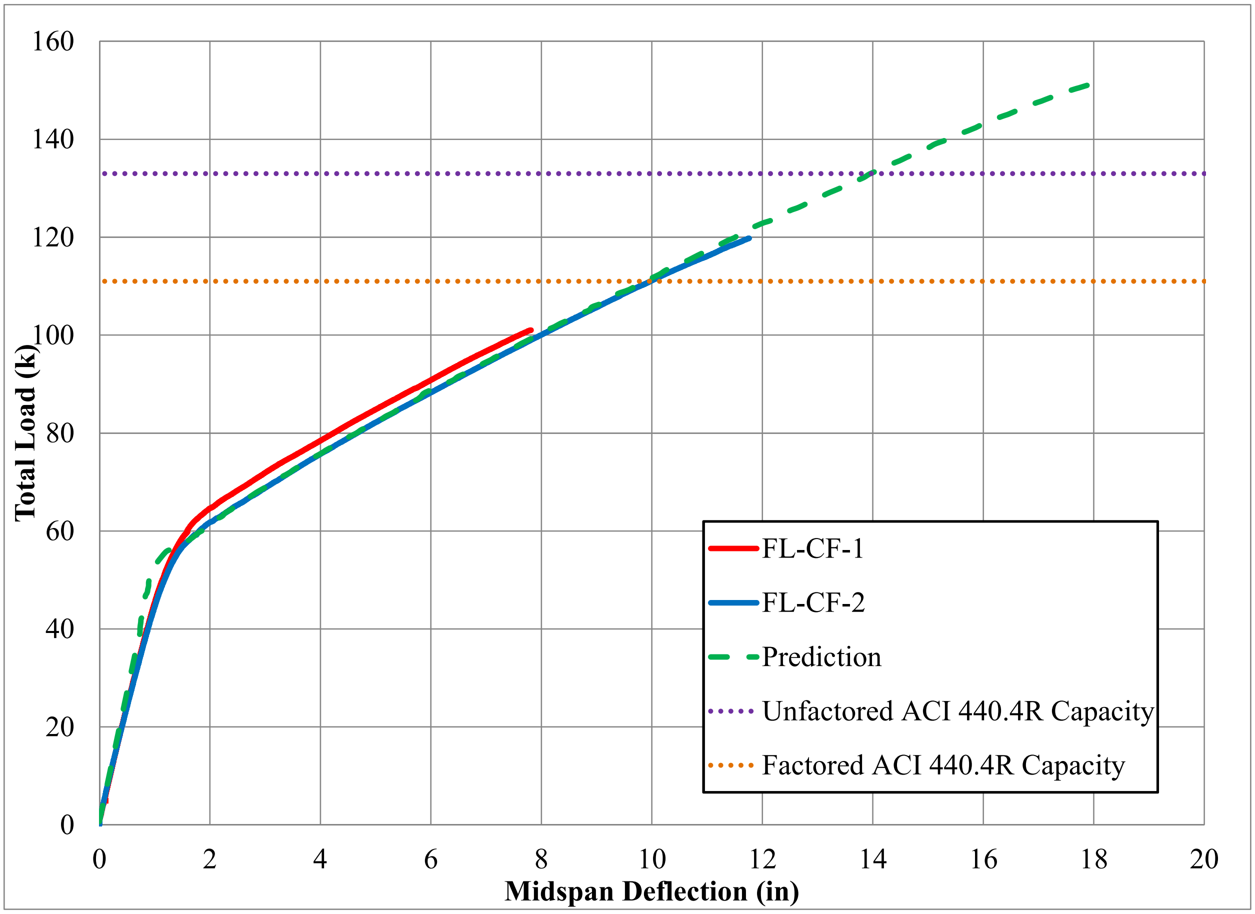


**Figure 4.32: Prediction and behavior of FRP reinforced cored slabs**

Inspection of the tested specimen revealed that the void tubes were at the correct height in this section. However, just before failure, while the concrete was beginning to crush, a crack developed on the side of the cored slab at the depth of the stirrups crossing through the compression zone, as illustrated in Figure 4.33. The concrete in the compression zone of FL-ST failed erratically in small pieces that separated from the top of the section, as depicted in Figure 4.34. During the failure of FL-CF-2, the top cover concrete separated from the specimen in a defined layer, exposing the top of the GFRP stirrups, as shown in Figure 4.35. This suggests that the presence of the GFRP stirrups in the compression zone may have contributed to the premature failure of the compression zone concrete.

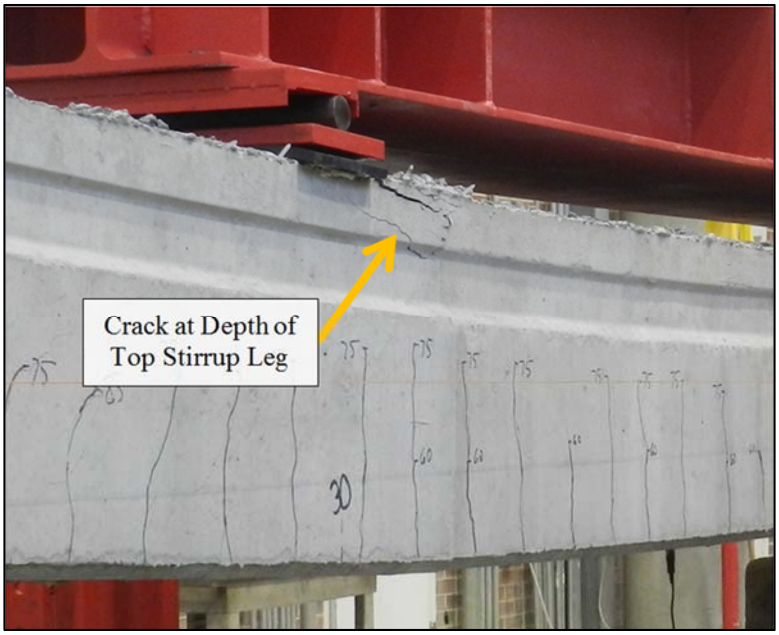


**Figure 4.33: Longitudinal crack forming at depth of stirrup in FL-CF-2**

**Figure 4.34: Top of FL-ST after failure**

**Figure 4.35: Top of FL-CF-2 after failure**

In steel reinforced cored slabs, the top segment of the steel stirrup is present in the compression zone. During loading, the concrete around the stirrups is compressed in the longitudinal direction due to bending. This compresses the stirrups in their transverse direction. But, because steel is an isotropic material with stiffness greater than concrete, the presence of the stirrups likely does not diminish the strength of the surrounding concrete.

Conversely, GFRP stirrups are anisotropic. They are manufactured to have high tensile strength in their longitudinal direction, but are not intended to resist compressive stresses in their transverse direction. GFRP bars loaded in transverse compression rely on the stiffness of their epoxy, which is significantly less than that of concrete. Additionally, due to Poisson's effect, when the GFRP bars are compressed in the horizontal transverse direction, they expand in the vertical transverse direction. This applies a splitting force to the concrete in the compression zone, as illustrated in Figure 4.36. The solid area represents the reinforcement and the hatched area represents the compression zone. The cross sectional area occupied by the stirrups in the concrete compression zone reduces the strength of the concrete.

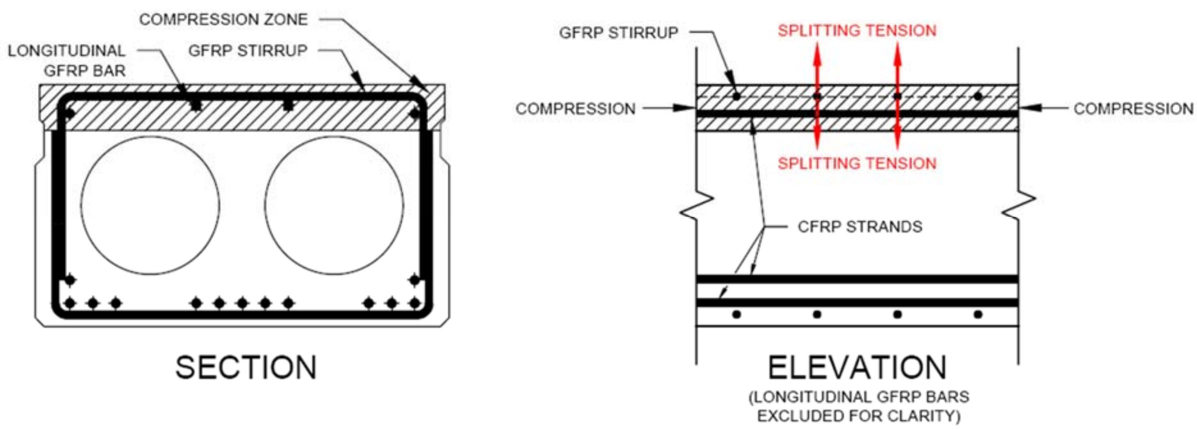


**Figure 4.36: Schematic of GFRP bars in the compression zone**

This effect was particularly detrimental to the strength of the cored slab because the large No. 5 stirrups were spaced closely at 7 in. and had approximately 1 in. of concrete cover. The cover was decreased from 1.5 in. for the steel reinforced slabs to 1 in. for GFRP reinforced slabs because the strand pattern was not changed, the stirrup size was increased from No. 4 to No. 5, and the steel and GFRP stirrups had bend radii of 1.5 and 2.25 in., respectively. The stirrups occupy 15.9% of the cross sectional area of the compression zone. ACI 440.1R (2006) does not include provisions to design for this weakening of the concrete due to GFRP stirrups, and no literature was found on this topic. It is speculated that this phenomenon is at least one factor leading to the lower than expected capacity of FL-CF-2.

Another factor that could have contributed to the lower than expected strength of FL-CF-2 was the effect of the stress concentration at the load points discussed in Section 4.5. At the failure location, there is the potential for adverse interaction between maximum moment and shear immediately outside the constant moment region. Some evidence of this is the diagonal nature of the failure planes that developed for the FL cored slab series, rather than only vertical flexural cracking, which would be expected in a pure moment failure.

### 4.6.4 Comparison of Specimens

The capacity predictions of the cored slabs presented in Section 4.2 were validated by the testing of FL-ST. These predictions were used to evaluate the performance of the FRP reinforced cored slabs. The results from FL-CF-1 highlighted a fabrication error that can significantly diminish the capacity of any cored slab, whether it is reinforced with steel or FRP.

FL-CF-2 revealed the potential negative effect of GFRP stirrups in the compression zone of the FRP reinforced cored slabs. However, this and other possible issues must be studied further so that they can be quantified. Although this specimen did not perform as well as predicted, it outperformed FL-ST, which was representative of the standard NCDOT design. Therefore, this test verified that an all-FRP reinforced cored slab can exhibit similar or better flexural performance compared to current steel reinforced cored slabs.

# CHAPTER 5: Shear Behavior

This chapter details the experimental program undertaken to investigate the shear strength of FRP reinforced cored slabs in comparison to steel reinforced cored slabs. One steel reinforced and two identical CFRP reinforced 15 ft. long cored slabs were designed. They were fabricated at the same time as the flexural specimens presented in Chapter 4. A test setup was designed and fabricated to cause the cored slabs to fail in shear. The cored slabs were delivered to the Constructed Facilities Laboratory at North Carolina State University. Both ends of each specimen were tested to failure on a shear span equal to the depth of the section. Results for the steel and FRP cored slabs were analyzed and compared and presented herein.

## 5.1 Shear Cored Slab Analysis and Predictions

Designing cored slab sections that would fail in shear required accurately analyzing the shear capacity of the section. The shear capacity was calculated using the following equations from ACI 318 (2011):

$$V_n = V_c + V_{reinf} \tag{5.1}$$

where $V_n$ is the nominal shear resistance, $V_c$ is the shear resistance provided by the concrete, and $V_{reinf}$ is the shear resistance provided by the steel or GFRP reinforcement.

$V_c$ is defined as the lesser of $V_{ci}$, the shear resistance to flexural-shear cracks, and $V_{cw}$, the resistance to web-shear cracks. $V_{ci}$ is calculated using:

$$V_{ci} = 0.6\,\lambda\sqrt{f'_c}\,b_w d_p + V_d + \frac{V_i M_{cre}}{M_{max}} \tag{5.2}$$

where $b_w$ is the width of the web, $d_p$ is the depth of the centroid of prestressing steel, $V_d$ is the shear force due to dead load, $V_i$ and $M_{max}$ are the shear and moment computed from the loading causing maximum moment, and $M_{cre}$ is the cracking moment, given by:

$$M_{cre} = \frac{I}{y_t}\left(6\,\lambda\sqrt{f'_c} + f_{pe} - f_d\right) \tag{5.3}$$

where $I$ is the section moment of inertia, $y_t$ is the distance from the centroidal axis to the tension face, $f_{pe}$ is the compression stress at the tension face due to prestressing, and $f_d$ is the stress at the tension face due to dead load.

The web-shear crack resistance is calculated using the following equation:

$$V_{cw}=\left(3.5\lambda\sqrt{f'_c}+0.3f_{pc}\right)b_w d_p \tag{5.4}$$

where $f_{pc}$ is the compression stress at the centroidal axis due to prestressing.

$V_{reinf}$ was calculated using the following:

$$V_{reinf}=\frac{A_v\, f_*\, d}{s} \tag{5.5}$$

where $A_v$ is the cross sectional area of two stirrup legs, $f_*$ is the yield ($f_y$) or maximum design ($f_{fv}$) stress of steel or GFRP, respectively, $d$ is the distance from the top compression fiber to the centroid of the tension reinforcement, and $s$ is the stirrup spacing. To make accurate predictions, average expected values for $f_y$ and $f_{fv}$ were applied. The value used for $f_y$ was 68 ksi, a typical value for yield stress of grade 60 bars. Testing from the manufacturer of the GFRP bars showed that bent No. 5 bars ruptured at approximately 82 ksi, so this value was used for $f_{fv}$ (Hughes Brothers, unpublished internal report, June 2008). The rupture stress of the straight GFRP bars was 105 ksi, but the ACI 440.1R (2006) stress limit of the bent bars was 50 ksi.

Initially, calculations were made for inducing a shear crack through the 3 ft. long solid zones at the ends of the specimens, which would mimic the in-service placement and loading of the slabs. However, the shear capacity of the section exceeded the shear force that could be applied by the largest hydraulic actuator available at the Constructed Facilities Laboratory, which has a load capacity of 450 kips. Therefore, the capacity of the cored slabs was calculated for a crack going through the hollow cores adjacent to the solid zones. A schematic of this shear span is shown in Figure 5.1. This setup reduced $b_w$ from 36 in. to 12 in., which decreased the value of $V_{cw}$ by 67%, as illustrated in Figure 5.2. However, while some of the concrete above and below the cores contributed to $V_{cw}$, this contribution could not be quantified using Equation (5.4). Therefore, the $V_{cw}$ calculated using a $b_w$ of 12 in. is a lower bound value.

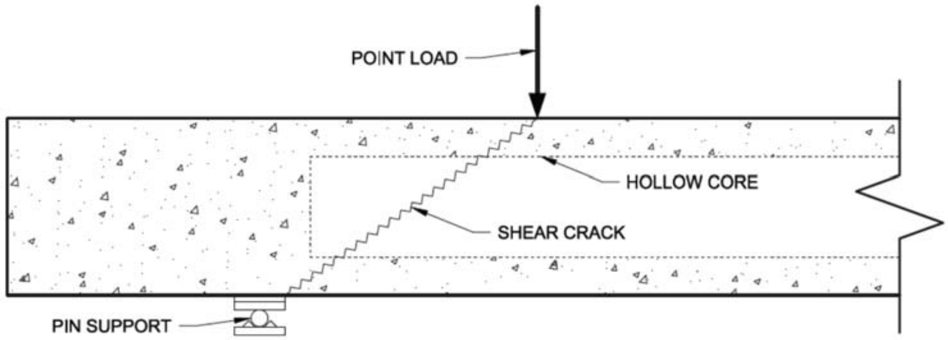


**Figure 5.1: Schematic of shear test alignment**

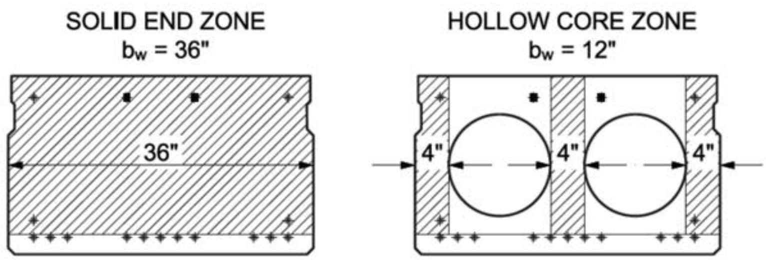


**Figure 5.2: Schematic of web widths of solid ends and cored middle regions of slabs**

To analyze the cored slabs for this test setup, $V_{ci}$, $V_{cw}$, $V_{reinf}$, and $V_A$, the applied shear for a given load from the actuator, were calculated at 3 in. intervals along the length of the slab from the face of the support to midspan. Then the $V_c$ values were added to the $V_{reinf}$ values to obtain the total shear resistance of the cored slab. Both steel and FRP reinforced sections were predicted to fail due to web-shear cracking. Figure 5.3 and Figure 5.4 show the predicted shear resistance and applied loading necessary to cause failure for the steel and FRP reinforced sections, respectively. The predicted loading from the actuator at failure was 248 and 323 kips for the steel and FRP reinforced specimens, respectively. The predicted capacity of the FRP reinforced specimens is significantly higher mostly because of the larger cross sectional area and high rupture stress of the GFRP stirrups. ACI 440.1R (2006) limits the shear crack width of members reinforced with FRP stirrups by limiting the maximum strain in the stirrups to 0.4%. While tests performed by the manufacturer indicated that the ultimate stress of the bent bars was

82 ksi, this serviceability requirement limits $f_{fv}$ in the GFRP rebar to 27 ksi for the ACI strength calculation.

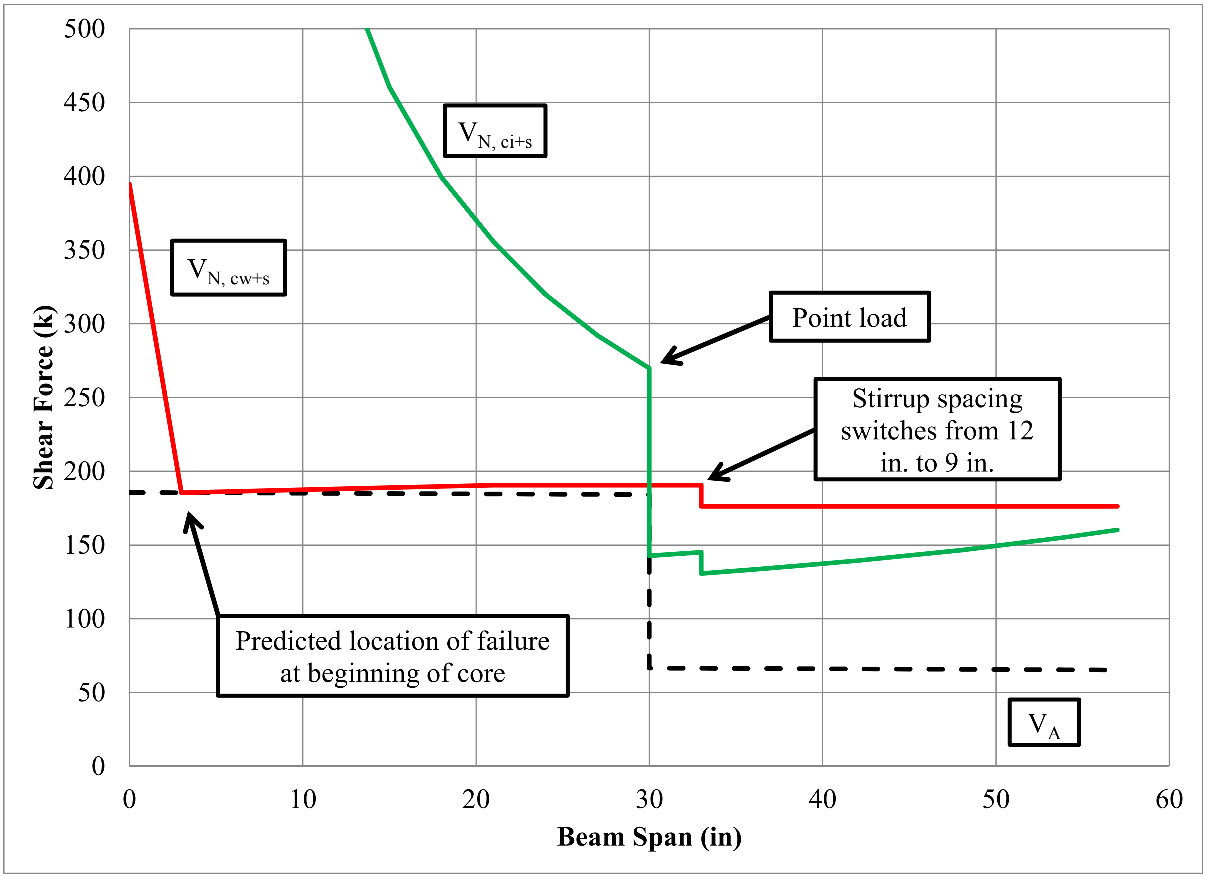


**Figure 5.3: Predicted shear behavior of steel reinforced specimen**

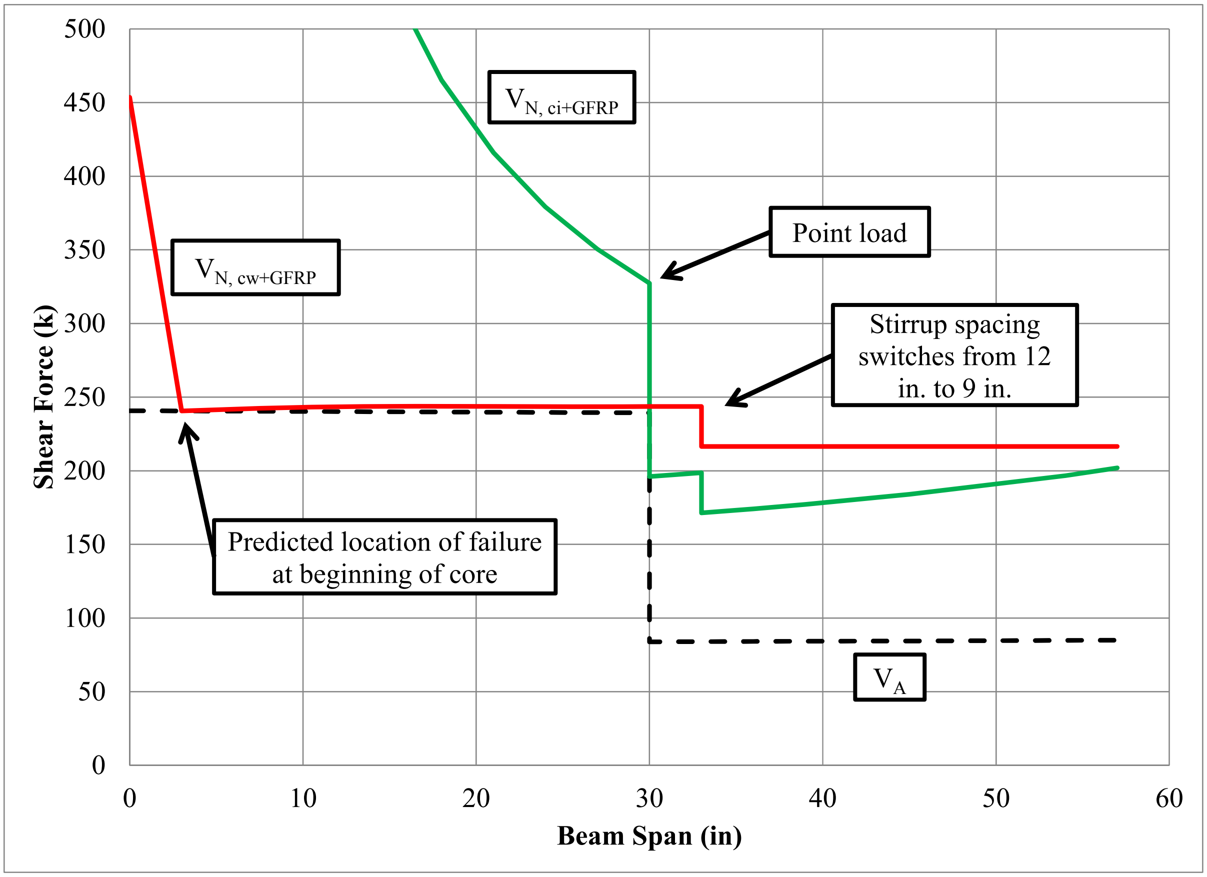


**Figure 5.4: Predicted shear behavior of FRP reinforced specimen**

To ensure that the shear failure mode governed, the flexural capacity and total moment were plotted along the same intervals as the shear force and resistance. The moment plots for the steel and FRP reinforced specimens are shown in Figure 5.5 and Figure 5.6, respectively. This analysis showed that the test setup chosen would cause a shear failure in the section when the total moment in the cored slabs was less than 55% of the moment capacity for both steel and FRP reinforced sections. The moment capacity varied along the length of the beam because the length that the strands were bonded to the concrete was less than the transfer length for some of the strands and less than the development length for all of the strands in this region of the cored slabs. A standard sectional analysis was carried out at each interval. The total prestressing force was equal to the amount allowed assuming a linear variation from zero to their effective stress along their transfer length. Likewise, the stress in the prestressing strands was limited to the stress they were able to achieve assuming a linear variation from zero to their rupture stress along their development length.

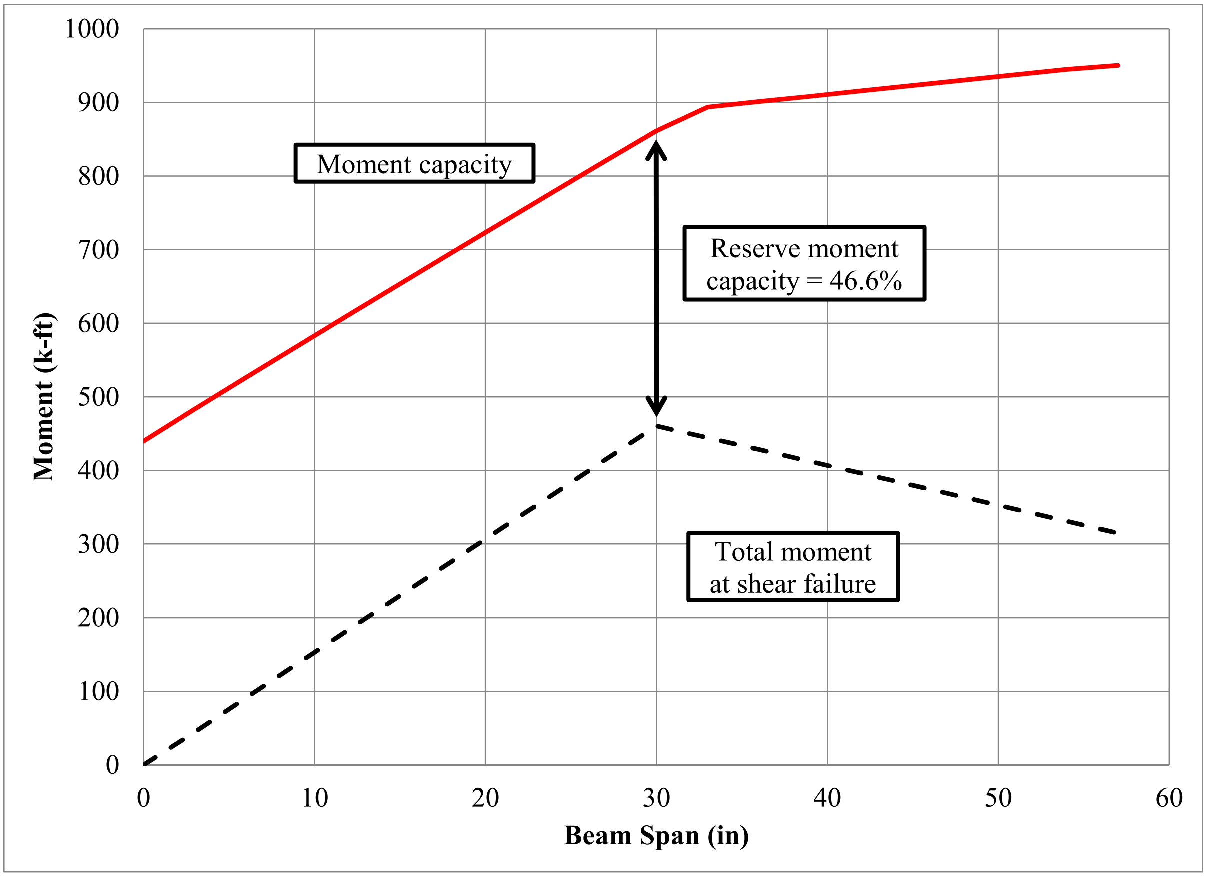


**Figure 5.5: Reserve moment capacity for steel reinforced specimen**

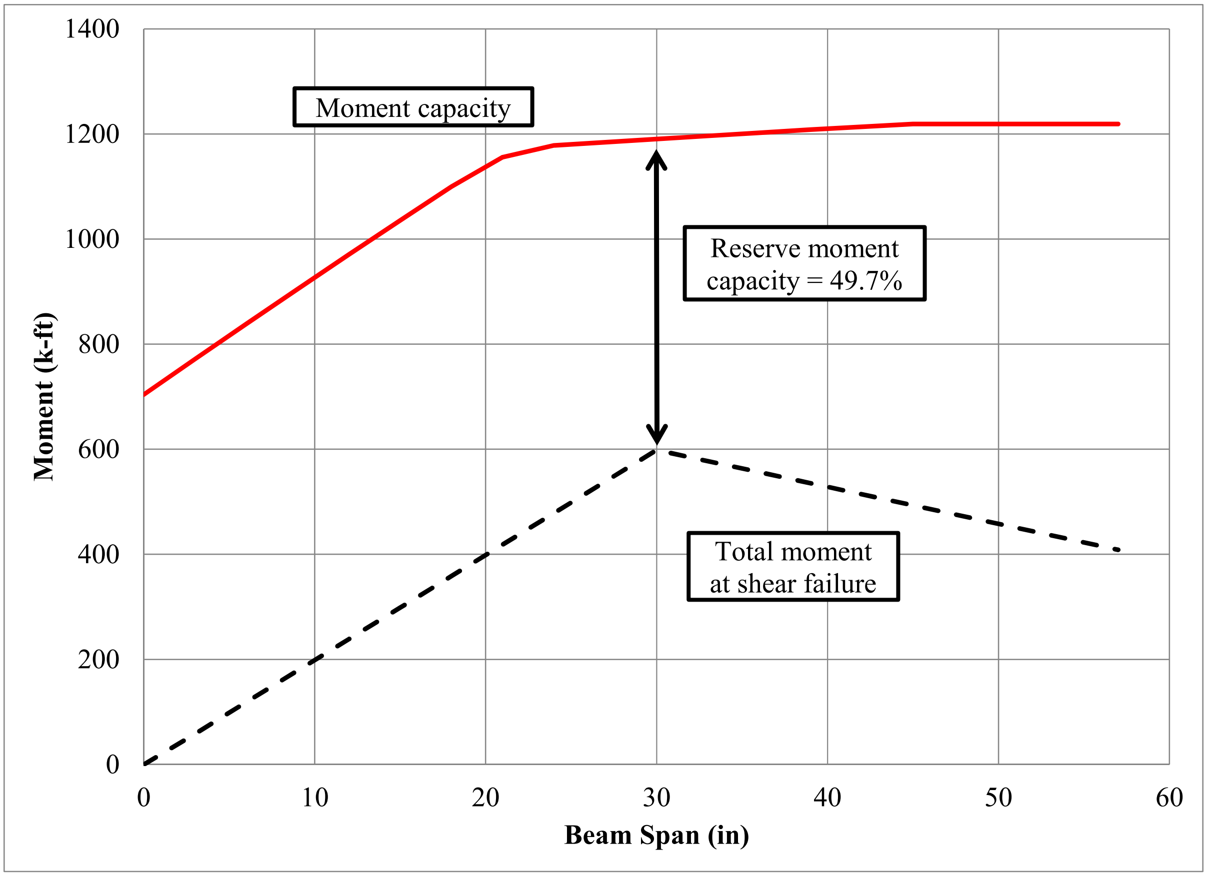


**Figure 5.6: Reserve moment capacity for FRP reinforced specimen**

The development lengths used in these calculations were based on the results from Section 3.3. ACI 318 (2011) gives the following equation for the transfer length of steel strands:

$$L_t = \frac{f_{pe}\, d_b}{3000} \tag{5.6}$$

where $f_{pe}$ is the effective stress in the prestressing strand.

The transfer length for the CFRP strand was calculated using the following equation from ACI 440.4R (2004):

$$L_t = \frac{f_{pe}\, d_b}{\alpha_t\, f'^{\,0.67}_c} \tag{5.7}$$

where $\alpha_t$ is an adjustment factor for units and CFRP strand manufacturer (for in.-lb units and CFCC, $\alpha_t$ is 11.2). These transfer and development lengths are summarized in Table 5.1.

**Table 5.1: Transfer and development lengths for shear analysis**

| | Transfer Length (in) | Development Length (in) |
|---|---|---|
| Steel Strand | 30 | 66 |
| CFRP Strand | 25 | 67 |

## 5.2 Shear Cored Slab Design and Fabrication

### 5.2.1 Steel Reinforced Cored Slab Design

The design of the shear control specimen was the same as the flexural control specimen, described in Section 4.1.1 except that the span was 15 ft. long instead of 45 ft. long. Therefore, only one pair of void tubes was used, and there were no solid zones in the middle of the cored slab. The cross section view and end reinforcement detail are the same as the flexural specimens, and the plan view of the shear reinforcement is illustrated in Figure 5.7.

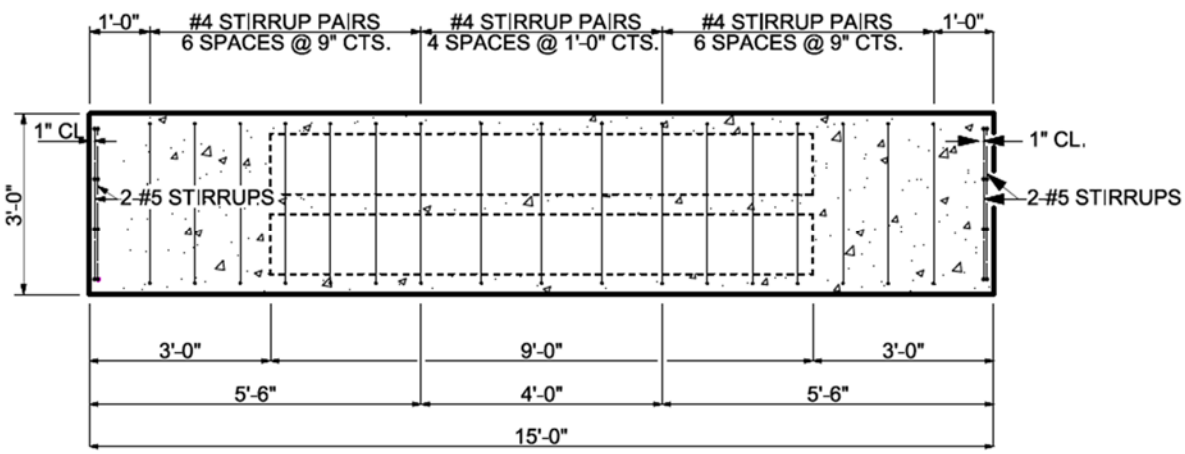


**Figure 5.7: Plan view of steel reinforced shear specimen**

### 5.2.2 FRP Reinforced Cored Slab Design

The FRP reinforced shear slabs were also the same as their flexural counterparts, discussed in Section 4.1.2, except for the stirrup spacing. The 7 in. spacing of GFRP stirrups did not allow the section to fail in shear with sufficient reserve moment capacity, calculated using the process described in Section 5.1. Therefore, the standard NCDOT stirrup spacing, also used for the steel reinforced specimen, was used. This reinforcing scheme is shown in Figure 5.8.

With the increased stirrup spacing, the ACI440.1R (2006) limit on stirrup strain was exceeded. Therefore, while this cored slab design would not be put into service, the design was necessary to enable the specimen to fail in shear.

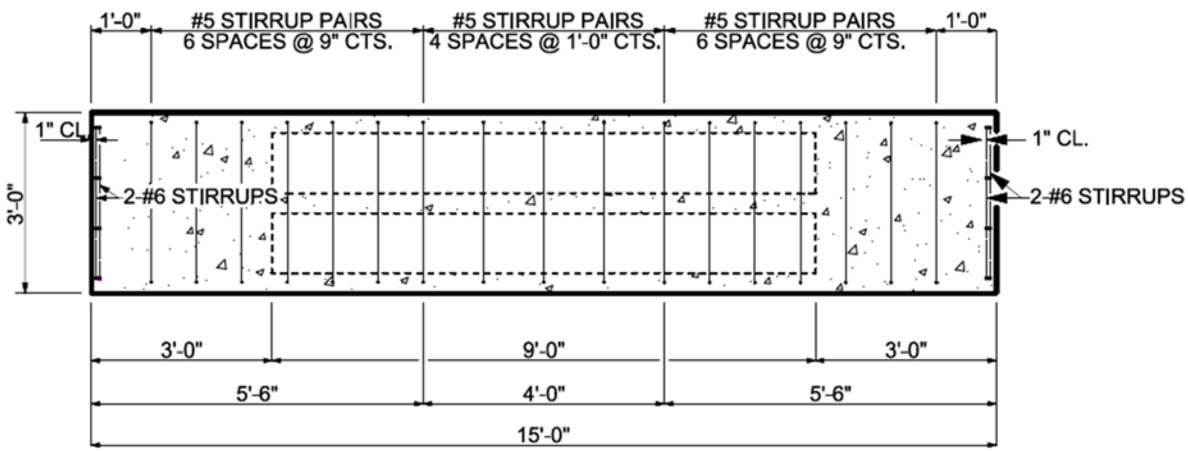


**Figure 5.8: Plan view of FRP reinforced shear specimen**

### 5.2.3 Shear Cored Slab Fabrication

The 15 ft. long cored slabs were cast at the same time, on the same casting beds as the 45 ft. long cored slabs. The manufacturing was identical to the process described in Section 4.3. Figure 5.9 shows all four FRP reinforced cored slabs on the casting bed after detensioning.

**Figure 5.9: FRP reinforced cored slabs on casting bed**

### 5.3 Shear Cored Slab Testing

The simply-supported test setup shown in Figure 5.10 was designed to test this series of cored slabs. Two concrete blocks were grouted to the strong floor, and a pin and roller support fabricated from steel plates and 2 in. steel round stock were grouted to the blocks. If the bottom surface of the cored slab contained any deformations, an elastomeric bearing pad was placed between the slab and the support. If the surface was flat, it was placed directly on the steel plate. Two 6x6x1/2 HSS sections were bolted to the bottom of the actuator to transfer the load to the specimen. Elastomeric bearing pads were used between the HSS and the specimen.

Shear cracks typically occur through a reinforced concrete beam at a 45° angle. In prestressed members, cracks are often flatter. Due to the size of the actuator, the load was applied by the two 6 in. wide HSS sections spaced 6 in. apart. This loaded the slab in an area across the full width of the section, along 18 in. in the longitudinal direction of the specimen. The face of the support made a 45° angle with the outside face of the HSS and a 35° angle with the centerline of the actuator.

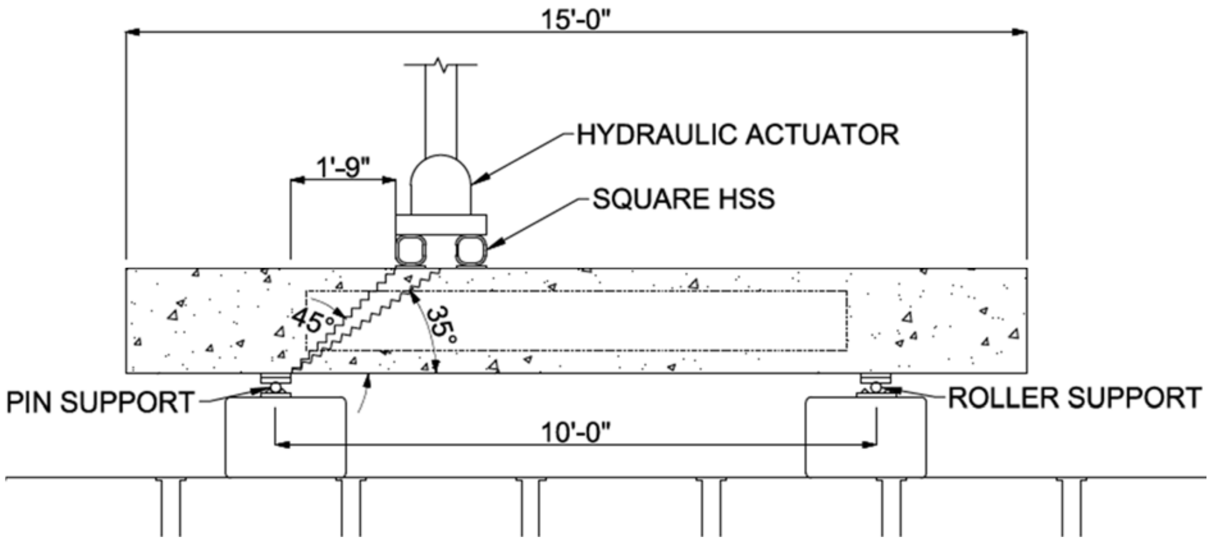


**Figure 5.10: Shear test setup schematic**

Two string potentiometers under the center of the actuator measured deflection. If a bearing pad was used, then a linear potentiometer measured the compression of the pad to be subtracted as support displacement. This instrumentation is shown in Figure 5.11.

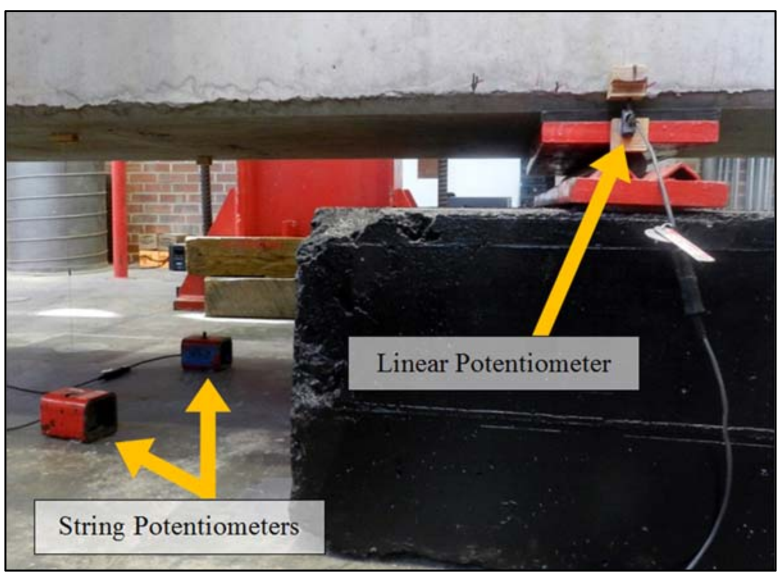


**Figure 5.11: Shear test instrumentation**

The specimens were loaded at a rate of 0.085 in./min until failure. Although this displacement rate was low, it caused the load to be increased at a rate of about 30 kips/min, due to the high stiffness of the cored slabs deforming in shear. An overall view of the test setup is depicted in Figure 5.12. A cored slab during testing is shown in Figure 5.13. Lines drawn with marker on the side of the specimen indicate where cracks had formed.

**Figure 5.12: Shear test setup**

**Figure 5.13: Shear specimen during testing**

The steel reinforced slab was labeled SH-ST and the FRP reinforced slabs were labeled SH-CF-1 and SH-CF-2. Both ends of each cored slab were tested to failure. The first and second ends were labeled tests A and B, respectively.

### 5.4 Shear Cored Slab Results

The results of the six tests are presented in this section. Comparison to predicted values and discussion of the significance of the results are presented in Section 5.5.

#### 5.4.1 SH-ST-A

The specimen was loaded up to 450 kips, which is the load capacity of the hydraulic actuator. Cracks formed in the shear span of the section, the slab deflected 0.28 in., but no failure occurred. The specimen after testing is shown in Figure 5.14.

**Figure 5.14: SH-ST-A after testing**

#### 5.4.2 SH-ST-B

The cored slab was rotated 180° and placed back on the testing frame. Again, the specimen was loaded up to 450 kips, cracks developed, but no failure occurred. Figure 5.15 shows SH-ST-B after the first cycle of loading.


**Figure 5.15: SH-ST-B after one cycle of loading**

The specimen was unloaded, then reloaded at the specified displacement rate six times. Each time it was reloaded, the deflection increased marginally. To induce a shear failure, the load was increased from zero load to 450 kips at the fastest rate the actuator would allow, approximately 100 kips/sec. This was repeated seven times until the specimen failed. While this loading did not yield any quantitative data about the shear capacity of the section, it confirmed that the section failed in shear and demonstrated the failure mode. At failure, the load was 456 kips and the deflection at failure was 0.48 in. The cored slab after testing is shown in Figure 5.16.

**Figure 5.16: SH-ST-B after failure**

### 5.4.3 SH-CF-1-A

This test had the same result as SH-ST-A. The slab was loaded to 450 kips and deflected 0.39 in., but did not fail. The specimen after testing is shown in Figure 5.17.

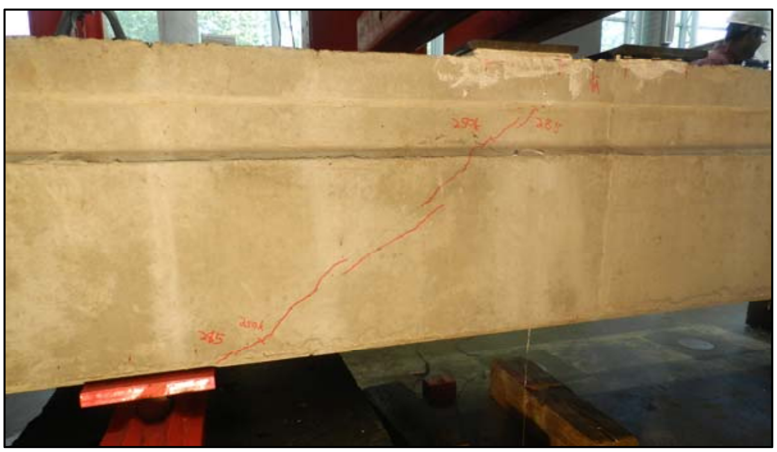

**Figure 5.17: SH-CF-1-A after testing**

### 5.4.4 SH-CF-1-B

This side of the slab failed after being loaded monotonically up to 446 kips. The deflection at failure was 0.44 in. The specimen is shown after failure in Figure 5.18.

**Figure 5.18: SH-CF-1-B after failure**

### 5.4.5 SH-CF-2-A

This specimen failed from monotonic loading at a load of 381 kips and a deflection of 0.31 in. The failed cored slab is shown in Figure 5.19.

**Figure 5.19: SH-CF-2-A after failure**

### 5.4.6 SH-CF-2-B

In order to test side B of this specimen after side A had failed, the supports had to be adjusted to extend the damaged portion of the slab past the support. The roller support was brought in 30 in. towards the middle of the span, just past the failure zone, as shown in Figure 5.20. The original location of the roller support is shown in dashed lines. The failed side of the slab before testing is depicted in Figure 5.21. By keeping the same length of shear span, but shortening the total simply-supported span, the maximum shear force that could be achieved in the shear span decreased from 332 kips to 289 kips, a 12.8% reduction.

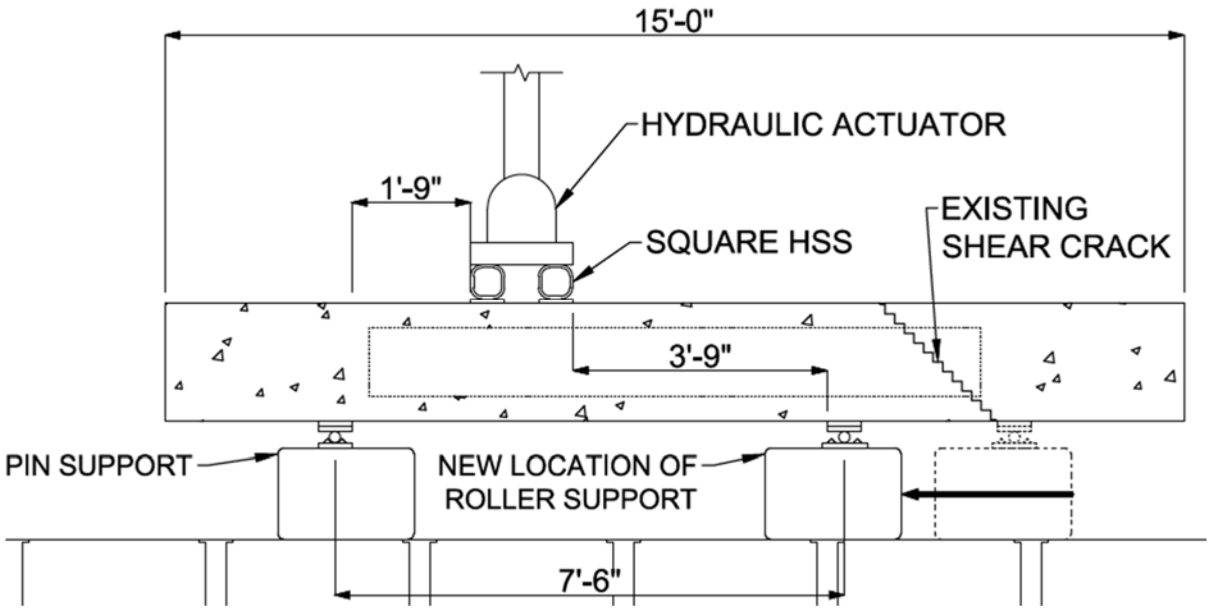


**Figure 5.20: Test setup for SH-CF-2-B**

**Figure 5.21: Relocated roller support before testing SH-CF-2-B**

The specimen was loaded once at the prescribed rate and did not fail. After two cycles of rapid loading, the slab failed with 455 kips of load on the side that had already failed. The measured deflection at failure was 0.29 in., the least of any of the tests. However, this deflection was low because the measurements were made on the side that was expected to fail, but not the side that did fail. The specimen after failure is shown in Figure 5.22. While the failure plane is flatter than the other tests, this is a shear failure.

**Figure 5.22: SH-CF-2-B after failure**

### 5.5 Shear Cored Slab Discussion

Figure 5.23 shows the shear force in the specimens at failure for all six tests along with the predicted values for shear resistance. These results are also summarized in Table 5.2. During the tests where no failure occurred, significant shear cracks developed in the section, indicating that the specimens were loaded into the inelastic portion of their response. The load-deflection curve for SH-CF-1-A, shown in Figure 5.24, confirms this. After the specimen was unloaded, it retained 0.08 in. of residual deflection, or 21% of its maximum deflection of 0.39 in.

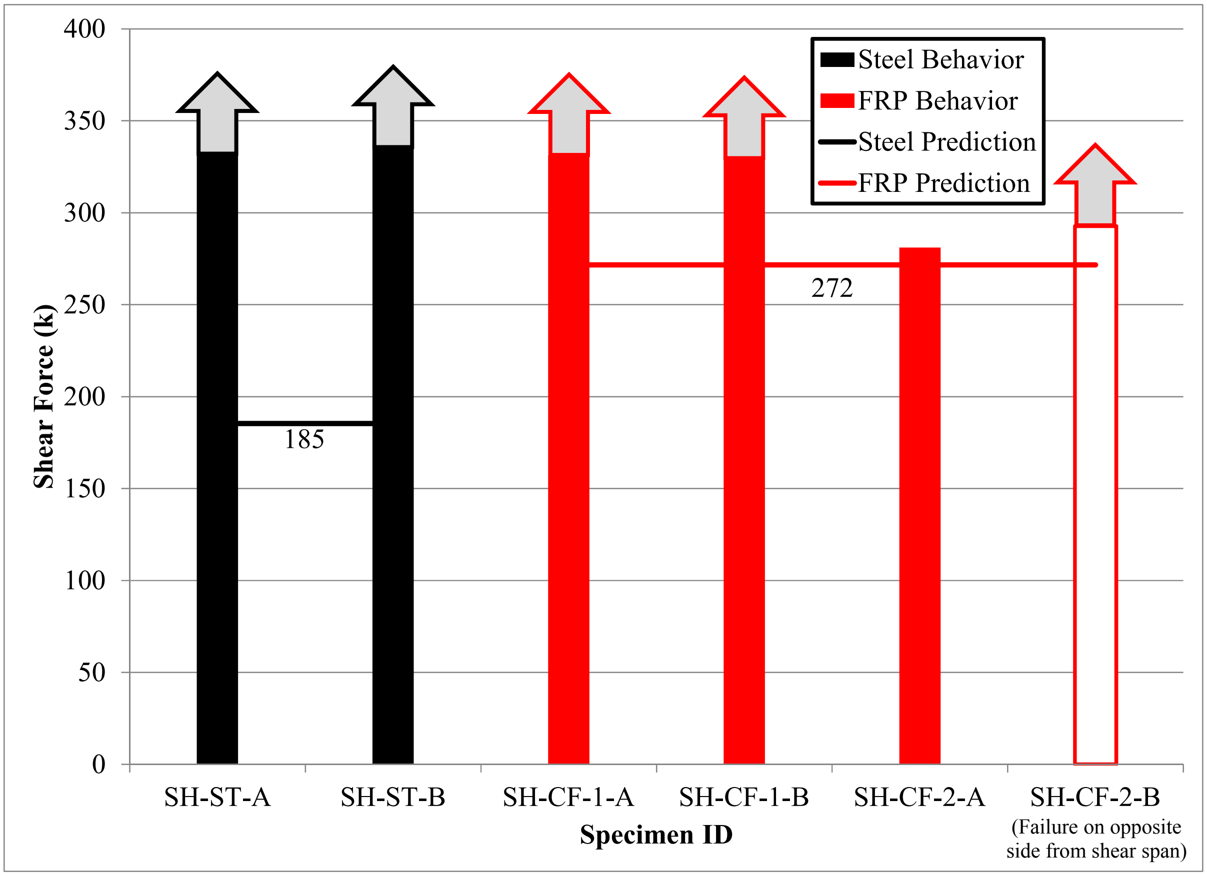


**Figure 5.23: Shear test results and predictions**

**Table 5.2: Shear test result summary**

| Test | Peak Actuator Load (k) | Peak Shear Force (k) | Peak Deflection (in) | Failure | Notes |
|---|---|---|---|---|---|
| SH-ST-A | 450 | 332 | 0.28 | None | No Failure |
| SH-ST-B | 456 | 336 | 0.48 | None | Failure occurred after 6 regular loading cycles and 7 rapid loading cycles |
| SH-CF-1-A | 450 | 331 | 0.39 | None | No Failure |
| SH-CF-1-B | 446 | 329 | 0.44 | Monotonic Loading* | *Shear failure occurred on side B after side A was loaded to 450 kips then unloaded |
| SH-CF-2-A | 381 | 281 | 0.31 | Monotonic Loading | Shear Failure |
| SH-CF-2-B | 455 | 293 | 0.29 | None | Failure occurred on the same side as SH-CF-2-A after 1 regular loading cycle and 7 rapid loading cycles (result affected by previous test) |

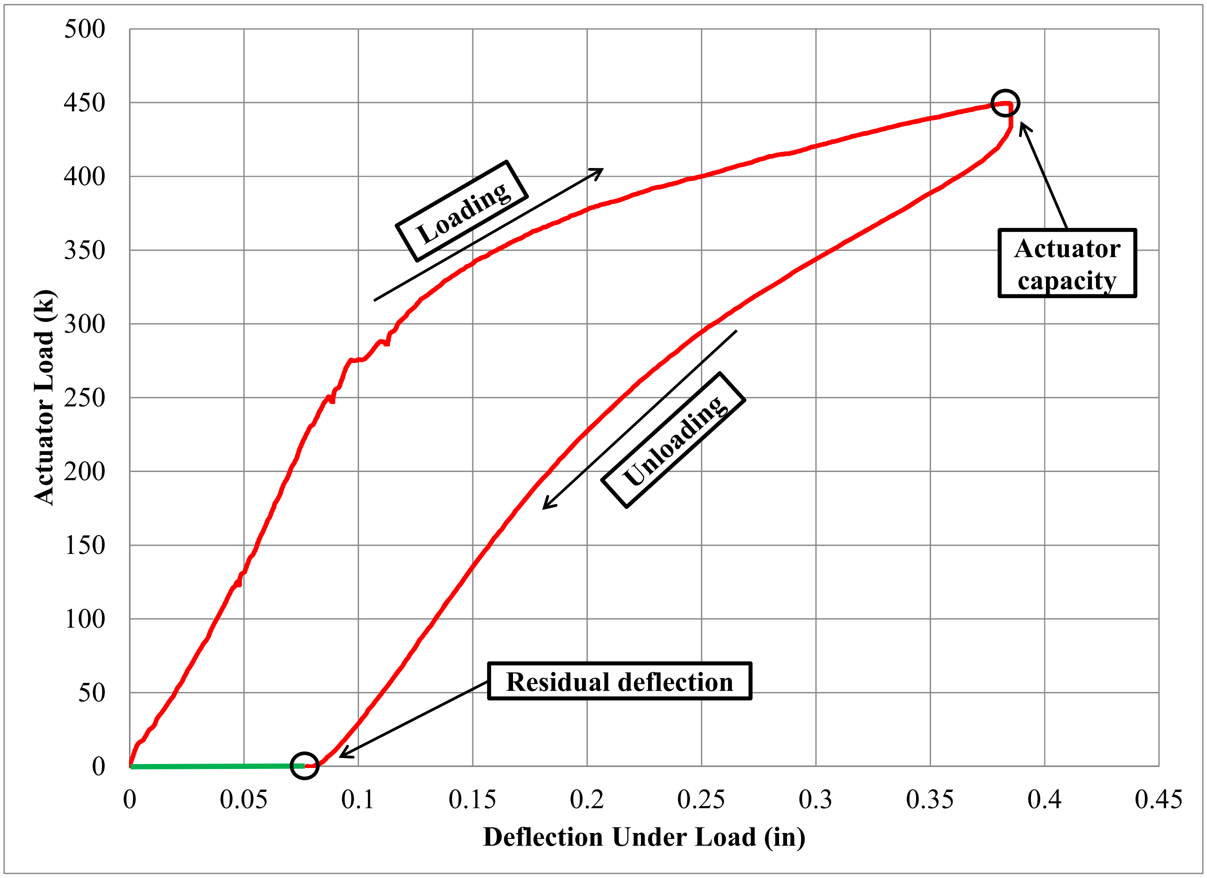


**Figure 5.24: Loading curve for SH-CF-1-A**

Note that SH-CF-2-A is the only specimen that failed under monotonic loading without the other end being damaged first. Therefore, the other specimens could have resisted more shear force if the loading increased. This is indicated by the arrows in Figure 5.23. While SH-CF-2-B failed at the maximum actuator load (450 kips), the shear force in the failure region of the slab (293 kips) was lower than the other specimens (330 kips) because the shear span was longer. Although predictions were made as accurately as possible, all of the specimens failed at a higher load than predicted. This shows that the ACI 318 (2011) provisions for calculating shear resistance give conservative values for short shear spans.

The steel and FRP reinforced cored slabs were predicted to have $V_{cw}$ values of 130 and 135 kips, respectively. However, concrete cracking did not occur until at least 180 kips of shear force were applied to the specimens. This behavior is reasonable considering that the calculation of $V_{cw}$ using Equation (5.4) gives a lower bound value, as discussed in Section 5.1.

Additionally, because the shear span was relatively short ($a/d$=1.4), the shear resistance during testing could have benefited by arching action in addition to beam action, which could have increased the capacity of the section. However, the failure of SH-CF-2-B occurred on the "wrong" side of the beam. Therefore, the failure occurred across a longer span ($a/d$=2.6), and appeared to be characterized more by beam action. Also, $V_{reinf}$ was calculated using $d/s$ = 2.3. However, inspection of specimens after testing showed that 3 stirrups spanned each shear crack, due to inclined cracks less than 45°, which increased $V_{reinf}$.

The specimens were only able to fail in shear when they were loaded through their hollow core zone. This is not a practical simulation of the loading the cored slabs face in service. The loads that were necessary to fail the sections in shear in the laboratory would have to be significantly higher to cause a shear failure to an in service beam because of the 3 ft. long solid zones at each end of the cored slabs. This implies that shear failure is not likely a concern for either steel or FRP reinforced cored slabs, and that the flexural failure mode dominates for this section.

# CHAPTER 6: Summary and Conclusions

This chapter summarizes key findings of the research project that was a comprehensive study of the application of FRP reinforcement in prestressed concrete cored slabs. The focus of the experimental program was to design and test a cored slab with all-FRP reinforcement that was similar in design and performance to the existing steel reinforced section. The results allowed an evaluation of the current design guidelines provided in ACI 440.4R (2004) and ACI 440.1R (2006).

## 6.1 Summary

This research project investigated the replacement of traditional steel reinforcement with FRP reinforcement in prestressed concrete cored slabs to prevent corrosion in aggressive environments. FRP is an attractive alternative to steel because it does not corrode and has high tensile strength. A series of tests were performed to characterize the behavior of the FRP reinforcement.

Tension tests were executed to verify the material properties given by the FRP manufacturers. Beam-end specimens were tested to compare the bond properties of the CFRP strands in comparison to steel strands. Full-scale flexural and shear specimens were tested to evaluate the performance of the FRP reinforced cored slabs in bending and shear relative to the steel reinforced cored slabs.

## 6.2 Conclusions

Based on the testing and results of this research project, the following conclusions are presented:

- The material properties for CFCC by Tokyo Rope and Aslan 100 Rebar by Hughes Brothers were accurate.
    - The guaranteed rupture stress given by Tokyo Rope for CFCC is highly conservative ($0.74f_u$).
- The development length of the CFCC strand used as non-prestressed reinforcement is between 108 and 115 $d_b$. The development length of steel prestressing strand used as non-prestressed reinforcement is less than 110 $d_b$.

- The flexural capacity of the properly manufactured FRP reinforced cored slab was 9% greater than the capacity of the steel reinforced control cored slab.
- A hollow core tube floating during casting dramatically weakens a cored slab section. Care must be taken to prevent this phenomenon during construction.
- The presence of closely spaced, large diameter GFRP stirrups in the compression zone of the FRP reinforced cored slabs appears to have caused premature failure of the specimens.
- Even with the effect from the GFRP stirrups, ACI 440.4R (2004) gives reasonable strength values for flexural capacity.
- ACI 440.4R (2004) also gives conservative values for shear strength.
- Due to the nature of the design of cored slabs, shear failure is unlikely to be a design concern, as the flexural failure mode dominates for this section.

Based on these conclusions, it can be said that the FRP reinforced cored slab design demonstrates equivalent or superior performance in monotonic flexure and shear compared to traditional steel reinforced cored slabs.

**6.3 Recommendations**

Based on the findings of this research program, the following recommendations are made.

- The performance demonstrated by the FRP reinforced sections in this experimental program, along with the excellent durability of the FRP reinforcement, should make the proposed cored slab design an effective and sustainable solution. Confidence in the system also comes from a growing number of field applications and the development of design codes for FRP reinforcement and prestressing.
- CFCC by Tokyo Rope and Aslan 100 rebar by Hugh Bros perform consistently with their published values. According to the literature, these FRP materials have excellent durability and should resist deterioration in harsh marine environments.

- The design procedure outlined in Section 4.1.2 should be used to design FRP reinforced cored slabs. When a total prestress force equal to the force used for steel-reinforced slabs is used, more strands will be required. This will lead to a conservative design. This initial design procedure should be followed by the calculations detailed in Appendix A.
- Due to the potential problem with closely space large diameter GFRP stirrups reducing concrete compression zone strength, other shear reinforcement options should be considered.
- Strict quality control measures should be taken to ensure that hollow core tubes do not float during casting.
- The significant additional time needed to install the coupler system during casting should be figured into the total cost of cored slab production. However, as more FRP prestressed concrete is cast, precasters will become more proficient at coupler installation.

### 6.4 Future Work

An unfunded research project at the North Carolina State University Constructed Facilities Laboratory is underway to better understand the effect of GFRP bars transverse to the direction of compression stress in concrete. This will test the proposed hypothesis that concrete in the compression zone of cored slabs is negatively affected by the presence of GFRP stirrups. It should be noted that this phenomenon has apparently not been observed in other published works on different reinforced concrete sections using more typical GFRP shear reinforcement details.

A life cycle assessment to evaluate the true economic benefit of replacing corrosive steel reinforced structural systems in aggressive environments with more durable FRP alternatives is also suggested.

## REFERENCES


Abdelrahman, A. A., and Rizkalla, S. H. (1998). "Serviceability of Concrete Beams Prestressed by Carbon Fiber-Reinforced-Plastic Bars." *ACI Structural Journal*, (94), 447–454.

Abdelrahman, A., Tadros, G., and Rizkalla, S. H. (1996). "Test model fot he first Canadian Smart Highway bridge." *ACI Structural Journal*, 92(4), 451–458.

ACI 318 (2011). "Building Code Requirements for Structural Concrete and Commentary." American Concrete Institute (ACI). Farmington Hills, Michigan.

ACI 440.1R (2006). "Guide for the Design and Construction Structural Concrete Reinforced with FRP Bars." American Concrete Institute (ACI). Farmington Hills, Michigan.

ACI 440.4R (2004). "Prestressing Concrete Structures with FRP Tendons." American Concrete Institute (ACI). Farmington Hills, Michigan.

ASTM A944 (2010). "Standard Test Method for Comparing Bond Strength of Steel Reinforcing Bars to Concrete Using Beam-End Specimens." American Society for Testing and Materials (ASTM). West Conshohocken, Pennsylvania.

Bank, L. C. (2007). *Composites for Construction: Structural Design with FRP Materials*. *Composites for Construction: Structural Design with FRP Materials*.

Braimah, A. (2000). "Long-Term and Fatigue Behaviour of Carbon Fibre Reinforced Polymer Prestressed Concrete Beams." Queen's University.

Brooks, T., and Cooper, M. D. (2003). *First CFRP Bridge in the USA: Michigan Researchers and Consultants Using Tomorrow's Technology Today*.

Clarke, J. L. (1993). *Alternative Materials for the Reinforcement and Prestressing of Concrete*. CRC Press, Boca Raton, FL.

Collins, M. P., and Mitchell, D. (1991). *Prestressed concrete structures*. Prentice-Hill, Englewood Cliffs, New Jersey.

Dolan, C. W., Hamilton III, H. R., Bakis, C., and Nanni, A. (2001). *Design Recommendations for Concrete Sturctures Prestressed with FRP Tendons*.

Domenico, N. G., Mahmoud, Z. I., and Rizkalla, S. H. (1998). "Bond properties of carbon fiber composite prestressing strands." *ACI Structural Journal*, 95(3), 281–290.

Ehsani, M. R., Saadatmanesh, H., and Nelson, C. T. (1997). “Transfer and Flexural Bond Performance of Aramid and Carbon FRP Tendons.” *PCI journal*, 42(1), 76–&.

Enomoto, T., Grace, N. F., and Harada, T. (2012). “Life Extension of Prestressed Concrete Bridges Using CFCC Tendons and Reinforcements.” *Proc., Conference on FRP Composites in Civil Engineering*, Rome, Italy.

Erki, M. A., and Rizkalla, S. H. (1993). “Anchorages For FRP Reinforcement.” *Concrete International*.

Fam, A. Z., Rizkalla, S. H., and Tadros, G. (1997). “Behavior of CFRP for prestressing and shear reinforcements of concrete highway bridges.” *ACI Structural Journal*, 94(1), 77–86.

Feng, W., Reifsnider, K., Sendeckyj, G., Chiao, T., Lien, P., Glaser, R., Moore, R., and Chiao, T. (1983). “Life Estimation of an S-Glass®/Epoxy Composite Under Sustained Tensile Loading.” *Journal of Composites Technology and Research*, 5(1), 21.

Gomez, J. (2014). “Innovative and Practical Research at VDOT.” *2014 Governor’s Transportation Conference*, Roanoke, Virginia.

Grace, N. F. (2000). “Transfer Length of CFRP / CFCC Strands for Double-T Girders.” *PCI Journal*, 45(5), 110–126.

Grace, N. F. (2014). “New Generation of Sustainable CFRP Prestressed Concrete Highway Bridges.” *Recent Research & Deployments*.

Grace, N. F., Asce, M., Jensen, E., Matsagar, V., and Penjendra, P. (2013a). “Performance of an AASHTO Beam Bridge Prestressed with CFRP Tendons.” *Journal of Bridge Engineering*, 18(2), 110–121.

Grace, N. F., Asce, M., Rout, S. K., Ushijima, K., and Bebawy, M. (2015). “Performance of Carbon-Fiber-Reinforced Polymer Stirrups in Prestressed-Decked Bulb T-Beams.” *Journal of Composites for Construction*, 19(3), 1–17.

Grace, N. F., Ushijima, K., Matsagar, V., and Wu, C. (2013b). “Performance of AASHTO-Type Bridge Model Prestressed with Carbon Fiber-Reinforced Polymer Reinforcement.” *ACI Structural Journal*, 110, 491–502.

Hanna, A. N. (2013). “Guide Specification for the Design of Concrete Bridge Beams Prestressed with CFRP Systems.” *TRB Projects*, <http://apps.trb.org/cmsfeed/TRBNetProjectDisplay.asp?ProjectID=3410>.

Hognestad, E. (1951). *A study on combined bending and axial load in reinforced concrete members*. Urbana-Champaign, Illinois.

Iyer, S. L. (1992). “Advanced Composite Demonstration Bridge Deck.” *ACI SP*, 138(49), 831–852.

Lu, Z., Boothby, T., Bakis, C., and Nanni, A. (2000). “Transfer and Development Lengths of FRP Prestressing Tendons.” *PCI journal PrecastPrestressed Concrete Institute*, (March-April), 80–91.

Mahmoud, Z. I., Rizkalla, S. H., and Zaghloul, E. E. R. (1999). “Transfer and development lengths of carbon fiber reinforced polymers prestressing reinforcement.” *ACI Structural Journal*, 96(4), 594–602.

Malvar, L. J. (2000). “Advanced Composites for the Navy Waterfront Infrastructure.” *ACI SP*, 196(2), 17–28.

Masséus, E. (2015). *Design of First FRP Reinforced Concrete Bridge in Florida*. Lake Buena Vista, Florida.

Mertol, H. C., Rizkalla, S. H., Scott, P., and Lees, J. M. (2007). “Durability of Concrete Beams Prestressed with CFRP Bars.” *ACI SP*, 245, 1–20.

Morvant, M. (2013). *I-10 Girder Repair Using Post-Tensioned Steel Rods and Carbon Fiber Composite Cables (CFCC)*. Baton Rouge, Louisiana.

Nagasaka, T., Fukuyama, H., and Tanigaki, M. (1993). “Shear performance of concrete beams reinforced with FRP sitrups.” *ACI SP*, 138(47), 789–812.

Nanni, A., Bakis, C., O’Neil, E., and Dixon, T. (1996). “Performance of FRP tendon-anchor systems for prestressed concrete structures.” *PCI journal*, (Jan-Feb), 34–44.

NCDOT. (2015). “Standard Design Plans.” <https://connect.ncdot.gov/resources/Structures/Pages/Standard-Design-Plans.aspx>.

Ozyildirim, H. C. (2013a). “Carbon-Fiber Composite Cable in Prestressed Bridge Beams.” *VCTIR Project Details*, <http://vtrc.virginiadot.org/ProjDetails.aspx?Id=575>.

Ozyildirim, H. C. (2013b). “Corrosion-Resistant Carbon-Fiber Composite Cable for Prestressed Bridge Piles.” *VCTIR Project Details*, <http://vtrc.virginiadot.org/ProjDetails.aspx?Id=462>.

Popovics, S. (1973). “A numerical approach to the complete stress-strain curves of concrete.” *Cement and Concrete Research*, 3(5), 583–599.

Rizkalla, S. H., Shehata, E., Abdelrahman, A. A., and Tadros, G. (1998). "The New Generation (Design and Construction of a Highway Bridge with CFRP)." *Concrete International*, 20(6), 35–38.

Rizkalla, S. H., and Tadros, G. (1994). "A smart highway bridge in Canada." *Concrete International*.

Saiedi, R., Green, M. F., and Fam, A. (2013). "Behavior of CFRP-Prestressed Concrete Beams under Sustained Load at Low Temperature." *Journal of Cold Regions Engineering*, 27(1), 1–15.

Santoh, N., Kimura, H., Enomoto, T., Kiuchi, T., and Kuzuba, Y. (1993). "Report on the Use of CFCC in Prestressed Concrete Bridges in Japan." *ACI SP*, 138(52), 895–912.

Sen, R., Mariscal, D., and Shahawy, M. (1993). "Investigation of S-2 Glass/Epoxy Strands in Concrete." *ACI SP*, 138(2), 15.

Shehata, E., Morphy, R., and Rizkalla, S. H. (2000). "Fibre reinforced polymer shear reinforcement for concrete members: behaviour and design guidelines." *Canadian Journal of Civil Engineering*, 27(5), 859–872.

Soudki, K. A. (1998). "FRP reinforcement for prestressed concrete structures." *Progress in Structural Engineering and Materials*, 1(2), 135–142.

Sovjak, R., Fornusek, J., Konvalinka, P., and Vitek, J. L. (2009). "Creep and Stress Relaxation of Concrete Slab with Pre-stressed GFRP." *Proc., Asia-Pacific Conference on FRP in Structures*, Seoul, Korea, 299–304.

Storm, T. K., Rizkalla, S. H., and Zia, P. Z. (2013). "Effects of production practices on camber of prestressed concrete bridge girders." *Pci Journal*, 58(4), 96–111.

Tottori, S., and Wakui, H. (1993). "Shear capacity of RC and PC beams using FRP reinforcement." *ACI SP*, 138(27), 615–631.

Wines, J. C., and Hoff, G. C. (1966). *Laboratory Investigation of Plastic-Glass Fiber Reinforcement for Reinforced and Prestressed Concrete*. Vicksburg, Missippippi.

# APPENDICES

# APPENDIX A: ACI 440.4R Design Calculations: Flexural Capacity

The geometric and material properties for the concrete, CFRP strands, and GFRP bars used in the FRP reinforced cored slabs are tabulated in Table A.1.

**Table A.1: Geometric and material properties for cored slabs**

| Property | Variable | Value | Units |
|---|---|---|---|
| **Concrete** | | | |
| Width of section | $b$ | 36 | in |
| Height of section | $h$ | 21 | in |
| Radius of cores | $r$ | 6 | in |
| Center of gravity of concrete | cgc | 10.5 | in |
| Area of concrete | $A_c$ | 530 | $in^2$ |
| Moment of inertia | $I_g$ | 25747 | $in^4$ |
| 28 day concrete strength | $f'_c$ | 9.5 | ksi |
| Modulus of elasticity of concrete | $E_c$ | 5556 | ksi |
| Equivalent rectangular stress ratio | $\beta_1$ | 0.65 | - |
| **CFCC** | | | |
| Depth to centroid of top steel | $d_T$ | 2.5 | in |
| Depth to centroid of first layer of bottom steel | $d_{B1}$ | 17 | in |
| Depth to centroid of second layer of bottom steel | $d_{B2}$ | 19 | in |
| Eccentricity of prestressing | $e$ | 6.03 | in |
| Center of gravity of steel strands | cgs | 16.53 | in |
| Distance from top prestressing to cgc | $y_T$ | 8 | in |
| Distance from first layer of bottom prestressing to cgc | $y_{B1}$ | 6.5 | in |
| Distance from second layer of bottom prestressing to cgc | $y_{B2}$ | 8.50 | in |
| Area of one 0.6" diameter strand | $A_{.6"\ strand}$ | 0.179 | $in^2$ |
| Area of top prestressing | $A_{psT}$ | 0.358 | $in^2$ |
| Area of first layer of bottom prestressing | $A_{psB1}$ | 0.358 | $in^2$ |
| Area of second layer of bottom prestressing | $A_{psB2}$ | 1.969 | $in^2$ |
| Area of total prestressing | $A_{psTOT}$ | 2.685 | $in^2$ |
| Modulus of elasticity of CFRP | $E_{CFRP}$ | 21900 | ksi |
| Guaranteed rupture stress | $f_{psMAX}$ | 339 | ksi |
| **GFRP** | | | |
| Area of GFRP bars | $A_{GFRP}$ | 0.62 | $in^2$ |
| Modulus of elasticity of GFRP | $E_{GFRP}$ | 6700 | ksi |

ACI 440.4R (2004) Table 3.3 limits the jacking stress of CFRP strands to $0.65f_{pu}$. Prestress losses of 25% are assumed:

$$f_{pe} = 0.75 \times 0.65 \times f_{pu} \tag{A.1}$$

$$f_{pe} = 0.75 \times 0.65 \times 339\, ksi = 165.3\, ksi$$

Calculate total prestressing force:

$$P_e = f_{pe} \times A_{psTOT} \tag{A.2}$$

$$P_e = 165.3\, ksi \times 2.685\, in^2 = 443.7\, k$$

Calculate strain in strands due to the axial prestressing effect:

$$\varepsilon_1 = \frac{f_{pe}}{E_{CFRP}} \tag{A.3}$$

$$\varepsilon_1 = \frac{165.3\, ksi}{21900\, ksi} = 7.55e-3$$

Calculate the decompression strain of all three layers of prestressing:

$$\varepsilon_2 = \frac{P_e}{E_c}\left(\frac{1}{A_c} + \frac{e \times y}{I_g}\right) \tag{A.4}$$

The $y_T$ value is negative because the top layer of prestressing is above the cgc. Therefore, the stresses induced by prestressing eccentricity are opposite in direction to the axial prestressing effect.

$$\varepsilon_{2T} = \frac{443.7\, k}{5556\, ksi}\left(\frac{1}{530\, in^2} + \frac{6.03\, in \times -8\, in}{25747\, in^4}\right) = 1.11e-6$$

$$\varepsilon_{2B1} = \frac{443.7\, k}{5556\, ksi}\left(\frac{1}{530\, in^2} + \frac{6.03\, in \times 6.5\, in}{25747\, in^4}\right) = 2.72e-4$$

$$\varepsilon_{2B2} = \frac{443.7\, k}{5556\, ksi}\left(\frac{1}{530\, in^2} + \frac{6.03\, in \times 8.5\, in}{25747\, in^4}\right) = 3.10e-4$$

The neutral axis depth is assumed to be $c$ = 4 in. Calculate the strain beyond decompression in all three layers of prestressing. Assume failure occurs from concrete crushing at a strain of $\varepsilon_{cu} = 3e-3$:

$$\varepsilon_{3T} = \varepsilon_{cu}\left(\frac{c - d_T}{c}\right) \tag{A.5}$$

$$\varepsilon_{3T} = 3e-3\left(\frac{4\ in - 2.5\ in}{4\ in}\right) = 1.13e-3$$

$$\varepsilon_{3B} = \varepsilon_{cu}\left(\frac{d_B - c}{c}\right) \tag{A.6}$$

$$\varepsilon_{3B1} = 3e-3\left(\frac{17\ in - 4\ in}{4\ in}\right) = 9.75e-3$$

$$\varepsilon_{3B2} = 3e-3\left(\frac{19\ in - 4\ in}{4\ in}\right) = 1.13e-2$$

Calculate the total strain at each level of prestressing. Because the concrete surrounding the top level of prestressing was in compression at release, and was in the compression zone throughout loading of the slab, $\varepsilon_{psT}$ is calculated as shown:

$$\varepsilon_{psT} = \varepsilon_1 - (-\varepsilon_{2T} + \varepsilon_{3T}) \tag{A.7}$$

$$\varepsilon_{psT} = (7.55e-3) + (1.11e-6) - (1.13e-3) = 6.42e-3$$

Bottom strands:

$$\varepsilon_{psB} = \varepsilon_1 + \varepsilon_{2B} + \varepsilon_{3B} \tag{A.8}$$

$$\varepsilon_{psB1} = (7.55e-3) + (2.72e-4) + (9.75e-3) = 1.76e-2$$

$$\varepsilon_{psB2} = (7.55e-3) + (3.10e-4) + (1.13e-2) = 1.91e-2$$

Find stress in prestressing strands:

$$f_{ps} = \varepsilon_{psT} \times E_{CFRP} \tag{A.9}$$

$$f_{psT} = 6.42e-3 \times 21900\ ksi = 140.7\ ksi$$

$$f_{psB1} = 1.76e-2 \times 21900\ ksi = 384.8\ ksi$$

This stress exceeds the design strength of the CFRP strand, $f_{psMAX}$, which is 339 ksi. Therefore, $c$ must be increased. To solve for $c_b$, the neutral axis depth at a balanced failure, first calculate the design strain of the CFRP strand:

$$\varepsilon_{ps\ MAX} = \frac{f_{psMAX}}{E_{CFRP}} \tag{A.10}$$

$$\varepsilon_{ps\ MAX} = \frac{339\ ksi}{21900\ ksi} = 1.55e-2$$

Next, calculate $\varepsilon_{3B2\ MAX}$, the strain beyond decompression in the bottom layer of prestressing strands corresponding to the design strength of the strands:

$$\varepsilon_{3B2\,MAX} = \varepsilon_{ps\,MAX} - \varepsilon_1 - \varepsilon_{2B} \tag{A.11}$$

$$\varepsilon_{3B2\,MAX} = (1.55e-2) - (7.55e-3) - (3.10e-4) = 7.62e-3$$

Use $\varepsilon_{3B2\,MAX}$ to calculate $c_b$:

$$c_b = d_{B2}\left(\frac{\varepsilon_{cu}}{\varepsilon_{cu} + \varepsilon_{3B2\,MAX}}\right) \tag{A.12}$$

$$c_b = 19\,in\left(\frac{3e-3}{(3e-3) + (7.62e-3)}\right) = 5.37\,in$$

Find the strains in the other prestressing strands using Equations (A.**5** (A.**6**, (**A**.**7**, and (A.**8**:

$$\varepsilon_{3T} = 3e-3\left(\frac{5.37\,in - 2.5\,in}{5.37\,in}\right) = 1.60e-3$$

$$\varepsilon_{3B1} = 3e-3\left(\frac{17\,in - 5.37\,in}{5.37\,in}\right) = 6.50e-3$$

$$\varepsilon_{psT} = (7.55e-3) + (1.11e-6) - (1.60e-3) = 5.95e-3$$

$$\varepsilon_{psB1} = (7.55e-3) + (2.72e-4) + (6.50e-3) = 1.43e-2$$

Find the corresponding stresses in the other prestressing strands using Equation (A.**9**:

$$f_{psT} = 5.95e-3 \times 21900\,ksi = 130.2\,ksi$$

$$f_{psB1} = 1.43e-2 \times 21900\,ksi = 313.7\,ksi$$

Calculate $T$, the resultant prestressing tensile force:

$$T = A_{psT} \times f_{psT} + A_{psB1} \times f_{psB1} + A_{psB2} \times f_{psB2} \tag{A.13}$$

$$T = 0.358\,in^2 \times 130.2\,ksi + 0.358\,in^2 \times 313.7\,ksi + 1.969\,in^2 \times 339.0\,ksi$$
$$= 826.4\,k$$

Calculate $C_c$, the resultant concrete compressive force:

$$C_c = 0.85 \times f'_c \times \beta_1 \times c \times b \tag{A.14}$$

$$C_c = 0.85 \times 9.5\,ksi \times 0.65 \times 5.37\,in \times 36\,in = 1014.0\,k$$

Because Cc > T, the section is controlled by the design strength of the bottom layer of strands, and the concrete does not reach $\varepsilon_{cMAX} = 3e-3$. Therefore, stress block factors are used to approximate the resultant force from the concrete in compression. These equations are used to find the maximum strain in the concrete corresponding to the strand design strength, $\varepsilon_{cMAX}$:

$$\beta_1 = \frac{4 \times \varepsilon'_c - \varepsilon_{cMAX}}{6 \times \varepsilon'_c - 2 \times \varepsilon_{cMAX}} \tag{A.15}$$

$$\alpha_1 = \frac{3 \times \varepsilon'_c \times \varepsilon_{cMAX} - \varepsilon_c^2}{3 \times \beta_1 \times \varepsilon'^2_c} \tag{A.16}$$

where $\varepsilon'_c$ is the maximum concrete strain:

$$\varepsilon'_c = \frac{1.7 \times f'_c}{E_c} \tag{A.17}$$

$$\varepsilon'_c = \frac{1.7 \times 9.5\ ksi}{5556\ ksi} = 2.91e - 3$$

Equation (A.**12** is adjusted to calculate $c$ given a constant $\varepsilon_{ps}$ ($\varepsilon_{3B2MAX}$) and a variable $\varepsilon_{cMAX}$:

$$c = d_{B2}\left(\frac{\varepsilon_{cMAX}}{\varepsilon_{cMAX} + \varepsilon_{3B2\ MAX}}\right) \tag{A.18}$$

The equation for the resultant force of the concrete compression zone for concrete that has not failed by crushing is:

$$C_c = \beta_1 \times \alpha_1 \times f'_c \times c \times b \tag{A.19}$$

To solve for $\varepsilon_{cMAX}$, Equation (A.**19** is set equal to the resultant force of the prestressing strands at the design strength of the bottom layer of CFRP calculated in Equation (A.**13**.

$$826.4\ k = \beta_1 \times \alpha_1 \times 9.5\ ksi \times c \times 36\ in \tag{A.20}$$

Equations (A.**15**, (A.**16**, and (A.**18** are substituted into Equation (A.**20**, so that the only variable is $\varepsilon_{cMAX}$. For simplicity, the values are solved in a spreadsheet by iterating $\varepsilon_{cMAX}$. The calculated value for $\varepsilon_{cMAX} = 2.21\text{e} - 3$. This new value of $\varepsilon_{cMAX}$ will change the value of $T$. Therefore, $c$ must be recalculated using Equation (A.**18**:

$$c = 19\ in\left(\frac{(2.21\text{e} - 3)}{(2.21\text{e} - 3) + (7.62e - 3)}\right) = 4.26\ in$$

This value of $c$ is used in Equations (A.**5** (A.**6**, (**A**.**7**, and (A.**8** to find the strain in the top two layers of CFRP strands:

$$\varepsilon_{3T} = 2.21\text{e} - 3\left(\frac{4.26\ in - 2.5\ in}{4.26\ in}\right) = 9.12e - 4$$

$$\varepsilon_{3B1} = 2.21\text{e} - 3\left(\frac{17\ in - 4.26\ in}{4.26\ in}\right) = 6.59e - 3$$

$$\varepsilon_{psT} = (7.55e - 3) + (1.11e - 6) - (9.12e - 4) = 6.64e - 3$$

$$\varepsilon_{psB1} = (7.55e - 3) + (2.72e - 4) + (6.59e - 3) = 1.44e - 2$$

Find the corresponding stresses in the other prestressing strands using Equation (A.**9**:

$$f_{psT} = 6.64e - 3 \times 21900\ ksi = 145.3\ ksi$$

$$f_{psB1} = 1.44e - 2 \times 21900\ ksi = 315.5\ ksi$$

These values are used to calculate *T* using Equation (A.**13**:

$$T = 0.358\ in^2 \times 145.3\ ksi + 0.358\ in^2 \times 315.5\ ksi + 1.969\ in^2 \times 339.0\ ksi$$
$$= 832.5\ k$$

This value is applied to Equation (A.**20**, and the process is repeated. The results are shown in Table A.2.

**Table A.2: Second iteration of calculated values**

| Variable | Value | Units |
|---|---|---|
| $\varepsilon_{cMAX}$ | 2.22E-03 | - |
| c | 4.28 | in |
| $\varepsilon_{3T}$ | 9.22E-04 | - |
| $\varepsilon_{3B1}$ | 6.59E-03 | - |
| $\varepsilon_{psT}$ | 6.63E-03 | - |
| $\varepsilon_{psB1}$ | 1.44E-02 | - |
| $f_{psT}$ | 145.1 | ksi |
| $f_{psB1}$ | 315.5 | ksi |
| T | 832.4 | k |

After the value of *T* converges, the nominal moment capacity is calculated by summing the moments about the bottom prestressing strand. Note that at equilibrium, $T = C_c$:

$$M_n = C_c\left(d_{B2} - \frac{\beta_1 c}{2}\right) - A_{psT}f_{psT}(d_{B2} - d_T) + A_{psB1}f_{psB1}(d_{B2} - d_{B1}) \qquad \text{(A.21)}$$

The tensile force from the top layer of CFRP has a deleterious effect on the moment capacity because it is in the compression zone.

$$M_n = \Big[832.4\ k\left(19\ in - \frac{0.72 \times 4.28\ in}{2}\right) - 0.358\ in^2 \times 145.1\ ksi(19\ in - 2.5\ in)$$
$$+ 0.358\ in^2 \times 315.5\ ksi(19\ in - 17\ in)\Big]\frac{1\ ft}{12\ in} = 1120\ k \cdot ft$$

According to ACI 440.4R Section 3.5 (2004), the strength reduction factor is 0.85 for FRP strand strains greater than 0.005. The design limit strain for the strands in this section is 0.0155, so Φ=0.85:

$$\Phi M_n = 0.85 \times 1120\ k - ft = 952.2\ k \cdot ft$$